

Heavy scalar top quark decays in the complex MSSM: A full one-loop analysisT. Fritzsche,^{1,*} S. Heinemeyer,^{2,‡} H. Rzehak,^{3,§,||} and C. Schappacher^{4,¶}¹*Max-Planck-Institut für Physik (Werner-Heisenberg-Institut), Föhringer Ring 6, D-80805 München, Germany*²*Instituto de Física de Cantabria (CSIC-UC), Santander, Spain*³*PH-TH, CERN, CH-1211 Genève 23, Switzerland*⁴*Institut für Theoretische Physik, Karlsruhe Institute of Technology, D-76128 Karlsruhe, Germany*

(Received 19 June 2012; published 21 August 2012)

We evaluate all two-body decay modes of the heavy scalar top quark in the minimal supersymmetric standard model with complex parameters (cMSSM) and no generation mixing. The evaluation is based on a full one-loop calculation of all decay channels, also including hard QED and QCD radiation. The renormalization of the complex parameters is described in detail. The dependence of the heavy scalar top quark decay on the relevant cMSSM parameters is analyzed numerically, including also the decay to Higgs bosons and another scalar quark or to a top quark and the lightest neutralino. We find sizable contributions to many partial decay widths and branching ratios. They are roughly of $\mathcal{O}(10\%)$ of the tree-level results, but can go up to 30% or higher. These contributions are important for the correct interpretation of scalar top quark decays at the LHC and, if kinematically allowed, at the ILC. The evaluation of the branching ratios of the heavy scalar top quark will be implemented into the Fortran code FEYNHIGGS.

DOI: [10.1103/PhysRevD.86.035014](https://doi.org/10.1103/PhysRevD.86.035014)

PACS numbers: 14.80.Ly, 12.15.Lk, 12.60.Jv

I. INTRODUCTION

One of the most important tasks at the LHC is to search for physics effects beyond the standard model (SM), where the minimal supersymmetric standard model (MSSM) [1] is one of the leading candidates. Supersymmetry (SUSY) predicts two scalar partners for all SM fermions as well as fermionic partners to all SM bosons. Another important task is investigating the mechanism of electroweak symmetry breaking. The most frequently investigated models are the Higgs mechanism within the SM and within the MSSM. Contrary to the case of the SM, in the MSSM two Higgs doublets are required. This results in five physical Higgs bosons instead of the single Higgs boson in the SM; three neutral Higgs bosons, h_n ($n = 1, 2, 3$), and two charged Higgs bosons, H^\pm .

If SUSY is realized in nature and the scalar quarks and/or the gluino are in the kinematic reach of the LHC, it is expected that these strongly interacting particles are copiously produced. This includes the production of scalar top quark pairs or the production of two gluinos with the subsequent (possible) decay to a scalar top quark and a top quark. An interesting production channel of Higgs bosons at the LHC is the decay of the heavy scalar top quark to the lighter scalar top (scalar bottom) quark and a

neutral (charged) Higgs boson, see, for instance, Refs. [2,3] and references therein. At the ILC (or any other future e^+e^- collider such as CLIC) a precision determination of the properties of the observed particles is expected [4,5]. (For combined LHC/ILC analyses and further prospects see Ref. [6].) Thus, if kinematically accessible, Higgs production via scalar top quark decays could offer important information about the stop and Higgs sector of the MSSM.

In order to yield a sufficient accuracy, one-loop corrections to the various scalar top quark decay modes have to be considered. We take into account all two-body decay modes of the heavy scalar top quark, \tilde{t}_2 , in the minimal supersymmetric standard model with complex parameters (cMSSM), but we neglect flavor violation effects and resulting decay channels that rather play a role for the decay of the light scalar top quark, \tilde{t}_1 , in special regions of the MSSM parameter space [7]. More specifically, we calculate the full one-loop corrections to the partial decay widths¹

$$\Gamma(\tilde{t}_2 \rightarrow \tilde{t}_1 h_n) \quad (n = 1, 2, 3), \quad (1)$$

$$\Gamma(\tilde{t}_2 \rightarrow \tilde{t}_1 Z), \quad (2)$$

$$\Gamma(\tilde{t}_2 \rightarrow t \tilde{\chi}_k^0) \quad (k = 1, 2, 3, 4), \quad (3)$$

$$\Gamma(\tilde{t}_2 \rightarrow t \tilde{g}), \quad (4)$$

$$\Gamma(\tilde{t}_2 \rightarrow \tilde{b}_i H^+) \quad (i = 1, 2), \quad (5)$$

*Thomas.Fritzsche@de.bosch.com

†Present address Robert Bosch GmbH, Corporate Sector Research and Advance Engineering, D-70839 Gerlingen-Schillerhöhe, Germany.

‡Sven.Heinemeyer@cern.ch

§heidi.rzehak@cern.ch

||On leave from Albert-Ludwigs-Universität Freiburg, Physikalisches Institut, D-79104 Freiburg, Germany.

¶cs@particle.uni-karlsruhe.de

¹It should be noted that the purely loop induced decay channels $\tilde{t}_2 \rightarrow \tilde{t}_1 \gamma/g$ have been neglected because they yield exactly zero, see Sec. III for further details.

$$\Gamma(\tilde{t}_2 \rightarrow \tilde{b}_i W^+) \quad (i = 1, 2), \quad (6)$$

$$\Gamma(\tilde{t}_2 \rightarrow b \tilde{\chi}_j^+) \quad (j = 1, 2), \quad (7)$$

where $\tilde{\chi}_k^0$ denotes the neutralinos, \tilde{g} the gluino, $\tilde{\chi}_j^\pm$ the charginos, t and b the top and bottom quark, and Z and W^\pm the SM gauge bosons. The total decay width is defined as the sum of the partial decay widths (1) to (7), where for a given parameter point several channels may be kinematically forbidden.

As explained above, we are especially interested in the branching ratios (BR) of the decays of the \tilde{t}_2 to a Higgs boson and another squark, Eqs. (1) and (5), as part of an evaluation of a Higgs production cross section. This can be an interesting production channel at the LHC (see, for instance, Ref. [8], where $pp \rightarrow \tilde{t}_1^\dagger \tilde{t}_1 h$ is analyzed, or Ref. [9], where searches for \mathcal{CP} -odd Higgs bosons in top squark decays are discussed). However, in order to reach a high accuracy, *all* two-body decay channels should be evaluated at one-loop. On the other hand, because we are interested in two-body modes (involving Higgs bosons), it is not necessary to investigate three- or four-body decay modes as these only play a significant role once the two-body decay modes are kinematically forbidden, and thus the relevant BR are zero.

We also concentrate on the decays of \tilde{t}_2 and do not investigate \tilde{t}_2^\dagger decays. In the presence of complex phases this would lead to somewhat different results. However, such an analysis of \mathcal{CP} -violating effects is beyond the scope of this paper.

Higher-order contributions to scalar fermion decays have been evaluated in various analyses over the last decade. However, they were in most cases restricted to one specific channel. In many cases only parts of a one-loop calculation has been performed, and no higher-order corrections in the cMSSM are available so far. More specifically, the available literature comprises the following. First, $\mathcal{O}(\alpha_s)$ corrections to partial decay widths of various squark decay channels in the MSSM with real parameters (rMSSM) were derived: to the decay of a squark to a quark and a chargino or neutralino in Ref. [10], to the decay of a squark to a quark and a gluino in Refs. [11,12], to the decay of a squark to a squark and a SM gauge boson in Ref. [13], and to the neutral Higgs boson radiation of a scalar top or bottom quark in Ref. [14]. (Those $\mathcal{O}(\alpha_s)$ corrections have been implemented into the code SDECAY [15].) A tree-level analysis on several \tilde{t} and \tilde{b} decay modes was presented in Ref. [16]. In a second step, Yukawa corrections to the partial decay widths of a scalar quark were evaluated in Refs. [17,18]. Finally, full one-loop contributions were derived, for the decay of a squark to a quark and a chargino or neutralino in Ref. [19], and for the decay of a scalar fermion to a scalar fermion and a gauge boson in Ref. [20]. One-loop corrections to scalar quark decays in the rMSSM, derived in a pure $\overline{\text{DR}}$ scheme (see below) have been made available in the program package SFOLD [21]. Also the

partial decay width of a \mathcal{CP} -even and a \mathcal{CP} -odd Higgs boson to scalar quarks at the one-loop level is available; see Refs. [22,23], respectively. A more recent evaluation can be found in Ref. [24]. Tree-level analyses for the decay of a \tilde{t} or a \tilde{b} in the cMSSM have been published in Refs. [25,26], and a one-loop calculation of a scalar top quark decaying to a bottom quark and a chargino in the cMSSM is presented in Ref. [27], where an LHC specific analysis can be found in Ref. [28]. Finally, results in an effective Lagrangian approach can be found in Ref. [29].

Several methods have been discussed in the literature to extract the complex parameters of the model from experimental measurements. Branching ratios at a linear collider were analyzed at the tree level in Ref. [26]. Triple products of decaying scalar top or bottom quarks have been examined in Ref. [30] (without specifying the production modes) and in Refs. [31–33] at the LHC. Rate asymmetries for decaying top squarks are analyzed in Ref. [27], again without specifying the production modes, and especially for the LHC in Ref. [28]. Depending on the realized cMSSM parameter space and on some further assumptions on the LHC performance, it seems to be possible to obtain limits on, e.g., the phases of M_1 , A_t , and A_b at the LHC. No corresponding analysis, to our knowledge, of the phase of M_3 has been performed so far.

In this paper we present for the first time a full one-loop calculation for all two-body decay channels of the heavier scalar top in the cMSSM (with no generation mixing), taking into account soft and hard QED and QCD radiation. In Sec. II we review the renormalization of all relevant sectors of the cMSSM. Details about the calculation can be found in Sec. III, and the numerical results for all decay channels are presented in Sec. IV. The conclusions can be found in Sec. V. The results will be implemented into the Fortran code FEYNHIGGS [34–37].

II. THE COMPLEX MSSM AND ITS RENORMALIZATION

All the channels (1)–(7) are calculated at the one-loop level, including hard QED and QCD radiation. This requires the simultaneous renormalization of several sectors of the cMSSM, including the colored sector with top and bottom quarks and their scalar partners as well as the gluon and the gluino, the Higgs and gauge boson sector with all the Higgs bosons as well as the Z and the W boson and the chargino/neutralino sector. In the following subsections we briefly review these sectors and their renormalization. To our knowledge, it is the first time that such a complete renormalization of the cMSSM has been performed.

A. The colored sector of the cMSSM

The colored sector of the cMSSM can be divided into a quark/squark part, a gluino part and a gluon part. The quark/squark part contains the soft SUSY-breaking mass parameters $M_{\tilde{q}_L}$, $M_{\tilde{q}_R}$, the trilinear couplings A_q , the quark

masses m_q as well as the quark and the squark fields² q and \tilde{q} , while the gluino part comprises the soft SUSY-breaking gaugino mass parameter M_3 and the gluino field \tilde{g} . From the gluon part, only the renormalization of the strong coupling constant α_s is needed for our calculation.

1. The top and bottom quark/squark sector

The part of the Fourier transformed Lagrangian that is bilinear in the quark and the squark fields with $q = \{t, b\}$ and $\tilde{q} = \{\tilde{t}, \tilde{b}\}$ can be written as

$$M_{\tilde{q}} = \begin{pmatrix} M_{\tilde{q}_L}^2 + m_q^2 + M_Z^2 c_{2\beta} (I_q^3 - Q_q s_w^2) & m_q X_q^* \\ m_q X_q & M_{\tilde{q}_R}^2 + m_q^2 + M_Z^2 c_{2\beta} Q_q s_w^2 \end{pmatrix} \quad (9)$$

with

$$X_q = A_q - \mu^* \kappa, \quad \kappa = \{\cot\beta, \tan\beta\} \quad \text{for } q = \{t, b\},$$

$$c_{2\beta} \equiv \cos 2\beta. \quad (10)$$

The soft SUSY-breaking mass parameter $M_{\tilde{q}_L}$ is equal for all members of an $SU(2)_L$ doublet, while the soft SUSY-breaking mass parameter $M_{\tilde{q}_R}$ can be different for scalar top and scalar bottom type quarks. Q_q and I_q^3 denote the charge and isospin of q . A_q is the trilinear soft-breaking parameter, μ the Higgs superfield mixing parameter, $\tan\beta \equiv v_2/v_1$ denotes the ratio of the two vacuum expectation values in the Higgs sector (see Sec. II B), M_Z and

$$m_{\tilde{q}_{1,2}}^2 = \frac{1}{2}(M_{\tilde{q}_L}^2 + M_{\tilde{q}_R}^2) + m_q^2 + \frac{1}{2}I_q^3 M_Z^2 c_{2\beta} \mp \frac{1}{2}\sqrt{[M_{\tilde{q}_L}^2 - M_{\tilde{q}_R}^2 + M_Z^2 c_{2\beta} (I_q^3 - 2Q_q s_w^2)]^2 + 4m_q^2 |X_q|^2}. \quad (12)$$

For the parameter and the field renormalization of the quark/squark sector we follow the procedure described in Ref. [38]. The quark mass and the squark mass matrix are replaced by the renormalized mass and mass matrix, respectively, and their counterterms,

$$m_q \rightarrow m_q + \delta m_q, \quad (13)$$

$$\mathbf{M}_{\tilde{q}} \rightarrow \mathbf{M}_{\tilde{q}} + \delta \mathbf{M}_{\tilde{q}}. \quad (14)$$

The mass matrix counterterm $\delta \mathbf{M}_{\tilde{q}}$ is obtained by applying the renormalization procedure—replacement of the parameters by the renormalized ones and the corresponding counterterms—for each parameter and expanding with respect to the introduced counterterms,

$$\delta \mathbf{M}_{\tilde{q}_{11}} = \delta M_{\tilde{q}_L}^2 + 2m_q \delta m_q - M_Z^2 c_{2\beta} Q_q \delta s_w^2 + (I_q^3 - Q_q s_w^2)(c_{2\beta} \delta M_Z^2 + M_Z^2 \delta c_{2\beta}), \quad (15)$$

²It should be noted that for the renormalization of the quark/squark sector we focus on the third generation—which is the relevant part for our calculation—but, in principle, it can be generalized to the other generations.

$$\mathcal{L}_{q/\tilde{q}}^{\text{bil.}} = (\tilde{q}_L^\dagger, \tilde{q}_R^\dagger)(p^2 \mathbb{1} - M_{\tilde{q}}) \begin{pmatrix} \tilde{q}_L \\ \tilde{q}_R \end{pmatrix} + \bar{q}(\not{p} - m_q)\omega_- q + \bar{q}(\not{p} - m_q)\omega_+ q, \quad (8)$$

where $\omega_\pm = \frac{1}{2}(\mathbb{1} \pm \gamma_5)$ are the right- and left-handed projectors, respectively. m_q with $q = \{t, b\}$ is the {top, bottom} quark mass and the stop and sbottom mass matrices, $M_{\tilde{t}}$ and $M_{\tilde{b}}$, are given by

M_W are the Z and W boson mass, respectively, and $c_w \equiv \cos\theta_w = M_W/M_Z$ with θ_w being the weak mixing angle, and $s_w = \sqrt{1 - c_w^2}$. The mass matrix can be diagonalized with the help of a unitary transformation $\mathbf{U}_{\tilde{q}}$,

$$\mathbf{D}_{\tilde{q}} = \mathbf{U}_{\tilde{q}} \mathbf{M}_{\tilde{q}} \mathbf{U}_{\tilde{q}}^\dagger = \begin{pmatrix} m_{\tilde{q}_1}^2 & 0 \\ 0 & m_{\tilde{q}_2}^2 \end{pmatrix}, \quad (11)$$

$$\mathbf{U}_{\tilde{q}} = \begin{pmatrix} U_{\tilde{q}_{11}} & U_{\tilde{q}_{12}} \\ U_{\tilde{q}_{21}} & U_{\tilde{q}_{22}} \end{pmatrix},$$

where the scalar quark masses, $m_{\tilde{q}_1}$, $m_{\tilde{q}_2}$, will always be mass ordered³ i.e. $m_{\tilde{q}_1} \leq m_{\tilde{q}_2}$, and are given by

$$\delta \mathbf{M}_{\tilde{q}_{12}} = (A_q^* - \mu \kappa) \delta m_q + m_q (\delta A_q^* - \mu \delta \kappa - \kappa \delta \mu), \quad (16)$$

$$\delta \mathbf{M}_{\tilde{q}_{21}} = \delta \mathbf{M}_{\tilde{q}_{12}}^*, \quad (17)$$

$$\delta \mathbf{M}_{\tilde{q}_{22}} = \delta M_{\tilde{q}_R}^2 + 2m_q \delta m_q + M_Z^2 c_{2\beta} Q_q \delta s_w^2 + Q_q s_w^2 (c_{2\beta} \delta M_Z^2 + M_Z^2 \delta c_{2\beta}) \quad (18)$$

with κ given in Eq. (10).

Instead of starting out with the squark mass matrix in Eq. (9) the mass matrix in terms of the squark masses as given in Eq. (11) can be used:

$$\mathbf{U}_{\tilde{q}} \mathbf{M}_{\tilde{q}} \mathbf{U}_{\tilde{q}}^\dagger \rightarrow \mathbf{U}_{\tilde{q}} \mathbf{M}_{\tilde{q}} \mathbf{U}_{\tilde{q}}^\dagger + \mathbf{U}_{\tilde{q}} \delta \mathbf{M}_{\tilde{q}} \mathbf{U}_{\tilde{q}}^\dagger = \begin{pmatrix} m_{\tilde{q}_1}^2 & Y_q \\ Y_q^* & m_{\tilde{q}_2}^2 \end{pmatrix} + \begin{pmatrix} \delta m_{\tilde{q}_1}^2 & \delta Y_q \\ \delta Y_q^* & \delta m_{\tilde{q}_2}^2 \end{pmatrix}, \quad (19)$$

³Because of the mass ordering, $\tilde{b}_2 \approx \tilde{b}_L$ is possible, which should be remembered when choosing a set of independent parameters—in our numerical examples, however, \tilde{b}_2 is rather b_R -like.

where $\delta m_{\tilde{q}_1}^2$ and $\delta m_{\tilde{q}_2}^2$ are the counterterms of the squark masses squared. In the mass matrix in Eq. (11) as well as in the first term of the right-hand side of Eq. (19) the squark mixing parameter Y_q vanishes as it should at tree level because the unitary matrix $U_{\tilde{q}}$ is chosen in that way to diagonalize the mass matrix $\mathbf{M}_{\tilde{q}}$. However, already at one-loop level, the squark mixing parameter Y_q receives a nonvanishing counterterm δY_q (which can be related to the counterterms of a mixing angle and a phase; see Ref. [39]). Using Eq. (19) one can express $\delta \mathbf{M}_{\tilde{q}}$ by the counterterms $\delta m_{\tilde{q}_1}^2$, $\delta m_{\tilde{q}_2}^2$, and δY_q . Especially for $\delta \mathbf{M}_{\tilde{q}_{11}}$ and $\delta \mathbf{M}_{\tilde{q}_{12}}$ this yields

$$\delta \mathbf{M}_{\tilde{q}_{11}} = |U_{\tilde{q}_{11}}^*|^2 \delta m_{\tilde{q}_1}^2 + |U_{\tilde{q}_{12}}|^2 \delta m_{\tilde{q}_2}^2 - U_{\tilde{q}_{22}} U_{\tilde{q}_{12}}^* \delta Y_q - U_{\tilde{q}_{12}} U_{\tilde{q}_{22}}^* \delta Y_q^*, \quad (20)$$

$$\delta \mathbf{M}_{\tilde{q}_{12}} = U_{\tilde{q}_{11}}^* U_{\tilde{q}_{12}} (\delta m_{\tilde{q}_1}^2 - \delta m_{\tilde{q}_2}^2) + U_{\tilde{q}_{11}}^* U_{\tilde{q}_{22}} \delta Y_q + U_{\tilde{q}_{12}} U_{\tilde{q}_{21}}^* \delta Y_q^*. \quad (21)$$

Equation (21) can be used together with Eq. (16) to express the counterterm for the trilinear top coupling δA_t and the counterterm for the bottom squark mixing parameter δY_b by the other counterterms [see Eqs. (51) and (52)].

For the field renormalization of the quark and the squark fields the following procedure is applied:

$$\omega_{-q} \rightarrow \left(1 + \frac{1}{2} \delta Z_q^L\right) \omega_{-q}, \quad (22)$$

$$\omega_{+q} \rightarrow \left(1 + \frac{1}{2} \delta Z_q^R\right) \omega_{+q}, \quad (23)$$

$$\tilde{q}_i \rightarrow \left[1 + \frac{1}{2} \delta \mathbf{Z}_{\tilde{q}}\right]_{ij} \tilde{q}_j. \quad (24)$$

$[\delta \mathbf{Z}_{\tilde{q}}]_{ij}$ with $i, j = 1, 2$ are the squark field renormalization constants and δZ_q^L and δZ_q^R the field renormalization constants for the left- and right-handed quark fields, respectively.

Following this renormalization procedure yields for the renormalized squark self-energies

$$\hat{\Sigma}_{\tilde{q}_{11}}(p^2) = \Sigma_{\tilde{q}_{11}}(p^2) + \frac{1}{2}(p^2 - m_{\tilde{q}_1}^2)[\delta \mathbf{Z}_{\tilde{q}} + \delta \mathbf{Z}_{\tilde{q}}^*]_{11} - \delta m_{\tilde{q}_1}^2, \quad (25)$$

$$\begin{aligned} \hat{\Sigma}_{\tilde{q}_{12}}(p^2) &= \Sigma_{\tilde{q}_{12}}(p^2) + \frac{1}{2}(p^2 - m_{\tilde{q}_1}^2)[\delta \mathbf{Z}_{\tilde{q}}]_{12} \\ &+ \frac{1}{2}(p^2 - m_{\tilde{q}_2}^2)[\delta \mathbf{Z}_{\tilde{q}}^*]_{21} - \delta Y_q, \end{aligned} \quad (26)$$

$$\begin{aligned} \hat{\Sigma}_{\tilde{q}_{21}}(p^2) &= \Sigma_{\tilde{q}_{21}}(p^2) + \frac{1}{2}(p^2 - m_{\tilde{q}_1}^2)[\delta \mathbf{Z}_{\tilde{q}}^*]_{12} \\ &+ \frac{1}{2}(p^2 - m_{\tilde{q}_2}^2)[\delta \mathbf{Z}_{\tilde{q}}]_{21} - \delta Y_q^*, \end{aligned} \quad (27)$$

$$\hat{\Sigma}_{\tilde{q}_{22}}(p^2) = \Sigma_{\tilde{q}_{22}}(p^2) + \frac{1}{2}(p^2 - m_{\tilde{q}_2}^2)[\delta \mathbf{Z}_{\tilde{q}} + \delta \mathbf{Z}_{\tilde{q}}^*]_{22} - \delta m_{\tilde{q}_2}^2. \quad (28)$$

The renormalized quark self-energy, $\hat{\Sigma}_q$, can be decomposed into left/right-handed and scalar left/right-handed parts, $\Sigma_q^{L/R}$ and $\Sigma_q^{SL/SR}$, respectively,

$$\begin{aligned} \hat{\Sigma}_q(p) &= \not{p} \omega_- \hat{\Sigma}_q^L(p^2) + \not{p} \omega_+ \hat{\Sigma}_q^R(p^2) + \omega_- \hat{\Sigma}_q^{SL}(p^2) \\ &+ \omega_+ \hat{\Sigma}_q^{SR}(p^2), \end{aligned} \quad (29)$$

where the components are given by

$$\hat{\Sigma}_q^{L/R}(p^2) = \Sigma_q^{L/R}(p^2) + \frac{1}{2}(\delta Z_q^{L/R} + \delta Z_q^{L/R*}), \quad (30)$$

$$\hat{\Sigma}_q^{SL}(p^2) = \Sigma_q^{SL}(p^2) - \frac{m_q}{2}(\delta Z_q^L + \delta Z_q^{R*}) - \delta m_q, \quad (31)$$

$$\hat{\Sigma}_q^{SR}(p^2) = \Sigma_q^{SR}(p^2) - \frac{m_q}{2}(\delta Z_q^R + \delta Z_q^{L*}) - \delta m_q. \quad (32)$$

It should be noted that $\widetilde{\text{Re}} \hat{\Sigma}_q^{SR}(p^2) = (\widetilde{\text{Re}} \hat{\Sigma}_q^{SL}(p^2))^*$ holds due to $\mathcal{CP}\mathcal{T}$ invariance.

We now review our choice of renormalization conditions where we follow the renormalization scheme of Ref. [38] with our favored “ $m_b, A_b, \overline{\text{DR}}$ ” scheme for the bottom quark/squark part. However, we expand this scheme to include also external bottom quarks (which was not investigated in Ref. [38]). In this case we deviate from the $m_b, A_b, \overline{\text{DR}}$ scheme and renormalize the bottom quark mass on-shell; see below. The problems found in Ref. [38] with this scheme do not arise in the processes with external bottom quarks considered in this paper as no external bottom squarks occur, and the trilinear coupling A_b is only needed at leading order in these processes.

The original parameters that we count as parameters of the top and bottom quark/squark sector are the soft SUSY-breaking mass parameters $M_{\tilde{q}_L}, M_{\tilde{t}_R}$, and $M_{\tilde{b}_R}$, the complex trilinear couplings $A_t \equiv |A_t| e^{i\varphi_{A_t}}$ and $A_b \equiv |A_b| e^{i\varphi_{A_b}}$, and the Yukawa couplings y_t and y_b that can be chosen to be real [the Cabibbo-Kobayashi-Maskawa (CKM) matrix is set to unity in our calculation and generation mixing effects are neglected]. Consequently, there are nine parameters to be defined in the top and bottom quark/squark sector. Instead of using the original parameters we choose the top squark masses $m_{\tilde{t}_1}, m_{\tilde{t}_2}$ and one bottom squark mass, $m_{\tilde{b}_2}$, as well as the quark masses m_t and m_b as independent input parameters.⁴ Also, in the scalar top quark sector a renormalization condition is chosen that fixes the counterterm δY_t instead of δA_t . For the parameters of the top quark/squark sector we impose on-shell (OS) conditions

⁴It should be noted that in the case $\tilde{b}_2 \approx \tilde{b}_L$, $m_{\tilde{b}_2}$ cannot be chosen as an independent parameter and the renormalization scheme has to be switched to one with $m_{\tilde{b}_1}$ as an input parameter.

while in the bottom quark/squark sector a mixed $\overline{\text{DR}}/\text{OS}$ scheme is employed:

(i–iii) The two top squark masses and the one bottom squark mass are determined via on-shell conditions,

$$\widetilde{\text{Re}}\hat{\Sigma}_{\tilde{t}_i}(m_{\tilde{t}_i}^2) = 0 \quad (i = 1, 2), \quad (33)$$

$$\widetilde{\text{Re}}\hat{\Sigma}_{\tilde{b}_{22}}(m_{\tilde{b}_2}^2) = 0, \quad (34)$$

yielding

$$\delta m_{\tilde{t}_i}^2 = \widetilde{\text{Re}}\hat{\Sigma}_{\tilde{t}_i}(m_{\tilde{t}_i}^2) \quad (i = 1, 2), \quad (35)$$

$$\delta m_{\tilde{b}_2}^2 = \widetilde{\text{Re}}\hat{\Sigma}_{\tilde{b}_{22}}(m_{\tilde{b}_2}^2). \quad (36)$$

$\widetilde{\text{Re}}$ denotes the real part with respect to contributions from the loop integrals, but leaves the complex couplings unaffected.⁵

(iv) The top quark mass is also defined on-shell,

$$\widetilde{\text{Re}}\hat{\Sigma}_t(p)t(p)|_{p^2=m_t^2} = 0, \quad (37)$$

yielding the one-loop counterterm δm_t ,

$$\delta m_t = \frac{1}{2}\widetilde{\text{Re}}\{m_t[\Sigma_t^L(m_t^2) + \Sigma_t^R(m_t^2)] + [\Sigma_t^{SL}(m_t^2) + \Sigma_t^{SR}(m_t^2)]\}, \quad (38)$$

referring to the Lorentz decomposition of the self-energy $\hat{\Sigma}_t(p)$; see Eq. (29).

(v) For the bottom quark mass we use two different definitions depending on whether in the considered decay channel a bottom quark appears as an external particle or not:

(a) In the case that no external bottom quarks are involved, the bottom quark mass is defined as $\overline{\text{DR}}$ mass with the corresponding counterterm,

$$\delta m_b^{\overline{\text{DR}}} = \frac{1}{2}\widetilde{\text{Re}}\{m_b[\Sigma_b^L(m_b^2) + \Sigma_b^R(m_b^2)]_{\text{div}} + [\Sigma_b^{SL}(m_b^2) + \Sigma_b^{SR}(m_b^2)]_{\text{div}}\}. \quad (39)$$

(b) If bottom quarks appear as external particles then we define the bottom quark mass on-shell,

$$\widetilde{\text{Re}}\hat{\Sigma}_b(p)b(p)|_{p^2=m_b^2} = 0, \quad (40)$$

to ensure the on-shell properties of the external particles that yield the following counterterm:

$$\delta m_b^{\text{OS}} = \frac{1}{2}\widetilde{\text{Re}}\{m_b[\Sigma_b^L(m_b^2) + \Sigma_b^R(m_b^2)] + [\Sigma_b^{SL}(m_b^2) + \Sigma_b^{SR}(m_b^2)]\}. \quad (41)$$

To have consistent input in all the decay channels we calculate the on-shell bottom quark mass m_b^{OS} starting from the $\overline{\text{DR}}$ mass,

$$m_b^{\text{OS}} = m_b^{\overline{\text{DR}}} + \delta m_b^{\overline{\text{DR}}} - \delta m_b^{\text{OS}}. \quad (42)$$

The value of $m_b^{\overline{\text{DR}}}$ is obtained as described in Eq. (65).

It should be noted that the problems found in Ref. [38] with an on-shell renormalization condition for m_b (leading, e.g., to unphysically large contributions to δA_b) do not occur as long as no external scalar bottom quarks appear at the same time and the parameter A_b is only needed at leading order. For example, the proposed scheme would presumably fail in the process $b\bar{b} \rightarrow \tilde{b}_i\tilde{b}_j^\dagger$, which, however, is beyond the scope of our paper.

(vi, vii) The complex counterterm of the nondiagonal entry of Eq. (19), which corresponds to two separate conditions, is fixed as [38–40]

$$\delta Y_t = \frac{1}{2}\widetilde{\text{Re}}\{\Sigma_{\tilde{t}_{12}}(m_{\tilde{t}_1}^2) + \Sigma_{\tilde{t}_{12}}(m_{\tilde{t}_2}^2)\}. \quad (43)$$

(viii, ix) In the scalar bottom quark sector the trilinear coupling is defined as a $\overline{\text{DR}}$ parameter with the counterterm,

$$\begin{aligned} \delta A_b = & \frac{1}{m_b} \left[U_{\tilde{b}_{11}} U_{\tilde{b}_{12}}^* (\widetilde{\text{Re}}\hat{\Sigma}_{\tilde{b}_{11}}(m_{\tilde{b}_1}^2)|_{\text{div}} - \widetilde{\text{Re}}\hat{\Sigma}_{\tilde{b}_{22}}(m_{\tilde{b}_2}^2)|_{\text{div}}) + \frac{1}{2} U_{\tilde{b}_{12}}^* U_{\tilde{b}_{21}} (\widetilde{\text{Re}}\hat{\Sigma}_{\tilde{b}_{12}}(m_{\tilde{b}_1}^2)|_{\text{div}} + \widetilde{\text{Re}}\hat{\Sigma}_{\tilde{b}_{12}}(m_{\tilde{b}_2}^2)|_{\text{div}}) \right. \\ & + \frac{1}{2} U_{\tilde{b}_{11}} U_{\tilde{b}_{22}}^* (\widetilde{\text{Re}}\hat{\Sigma}_{\tilde{b}_{12}}(m_{\tilde{b}_1}^2)|_{\text{div}} + \widetilde{\text{Re}}\hat{\Sigma}_{\tilde{b}_{12}}(m_{\tilde{b}_2}^2)|_{\text{div}})^* - \frac{1}{2} (A_b - \mu^* \tan\beta) \widetilde{\text{Re}}\{m_b[\Sigma_b^L(m_b^2) + \Sigma_b^R(m_b^2)]_{\text{div}} \\ & \left. + [\Sigma_b^{SL}(m_b^2) + \Sigma_b^{SR}(m_b^2)]_{\text{div}}\} \right] + \delta\mu^*|_{\text{div}} \tan\beta + \mu^* \delta \tan\beta, \end{aligned} \quad (44)$$

which also counts for two separate renormalization conditions as A_b is a complex parameter. The divergent parts of $\delta\mu$ and $\delta \tan\beta$ can be extracted from Eqs. (181) and (120c), respectively.

With these renormalization conditions all independent parameters in the top and bottom quark/squark sector are defined. The dependent parameters can be expressed in terms of those independent ones and the same applies for the corresponding

⁵It should be noted that we impose later an extra renormalization condition concerning the \tilde{b}_1 mass to solve infrared problems; see Eq. (46) below.

counterterms. With respect to this renormalization scheme the (one-loop corrected) on-shell \tilde{b}_1 mass, $m_{\tilde{b}_1}^{\text{OS}}$, differs from the mass parameter $m_{\tilde{b}_1}$. As an external particle \tilde{b}_1 should fulfill the on-shell properties, which in turn requires that it should have the mass

$$(m_{\tilde{b}_1}^{\text{OS}})^2 = (m_{\tilde{b}_1})^2 + (\delta m_{\tilde{b}_1}^{\text{dep}})^2 - \widetilde{\text{Re}}\Sigma_{\tilde{b}_1}(m_{\tilde{b}_1}^2), \quad (45)$$

where $\delta m_{\tilde{b}_1}^{\text{dep}}$ is the dependent mass counterterm⁶ that results from imposing only the renormalization conditions (i)–(ix). On the other hand, using $m_{\tilde{b}_1}$ for the internal \tilde{b}_1 squarks and $m_{\tilde{b}_1}^{\text{OS}}$ for the external \tilde{b}_1 squarks (which would formally be correct with respect to the considered loop order) leads to nonvanishing infrared (IR) singularities (for details see Ref. [38]).

To circumvent this problem we impose a further OS renormalization condition

$$\delta m_{\tilde{b}_1}^2 = \widetilde{\text{Re}}\Sigma_{\tilde{b}_1}(m_{\tilde{b}_1}^2). \quad (46)$$

As now all the squark masses within one generation are renormalized as on-shell, an explicit restoration of the $SU(2)$ relation is needed. This is performed in requiring that the left-handed (bare) soft SUSY-breaking mass parameter is the same in the bottom as in the top squark sector at the one-loop level,

$$M_{\tilde{q}_L}^2(\tilde{b}) + \delta M_{\tilde{q}_L}^2(\tilde{b}) = M_{\tilde{q}_L}^2(\tilde{t}) + \delta M_{\tilde{q}_L}^2(\tilde{t}). \quad (47)$$

More precisely, we define (see also Refs. [13,14,41])

$$M_{\tilde{q}_L}^2(\tilde{b}) = M_{\tilde{q}_L}^2(\tilde{t}) + \delta M_{\tilde{q}_L}^2(\tilde{t}) - \delta M_{\tilde{q}_L}^2(\tilde{b}) \quad (48)$$

with

$$\begin{aligned} \delta M_{\tilde{q}_L}^2(\tilde{q}) &= |U_{\tilde{q}_{11}}|^2 \delta m_{\tilde{q}_1}^2 + |U_{\tilde{q}_{12}}|^2 \delta m_{\tilde{q}_2}^2 - U_{\tilde{q}_{22}} U_{\tilde{q}_{12}}^* \delta Y_q \\ &\quad - U_{\tilde{q}_{12}} U_{\tilde{q}_{22}}^* \delta Y_q^* - 2m_q \delta m_q + M_Z^2 c_{2\beta} Q_q \delta s_W^2 \\ &\quad - (I_q^3 - Q_q s_W^2)(c_{2\beta} \delta M_Z^2 + M_Z^2 \delta c_{2\beta}), \end{aligned} \quad (49)$$

where $\delta M_{\tilde{q}_L}^2(\tilde{q})$ is derived with the help of Eqs. (15) and (20). Now $M_{\tilde{q}_L}^2(\tilde{b})$ is used in the scalar bottom mass matrix instead of the parameter $M_{\tilde{q}_L}^2$ in Eq. (9) when calculating the values of $m_{\tilde{b}_1}$ and $m_{\tilde{b}_2}$. However, with this procedure, also the mass of the \tilde{b}_2 squark is shifted, which contradicts our choice of independent parameters. To keep this choice, also the right-handed soft SUSY-breaking mass parameter $M_{\tilde{b}_R}$ receives a shift⁷:

$$\begin{aligned} M_{\tilde{b}_R}^2 &= \frac{m_{\tilde{b}}^2 |A_b^* - \mu \tan\beta|^2}{M_{\tilde{q}_L}^2(\tilde{b}) + m_{\tilde{b}}^2 + M_Z^2 c_{2\beta} (T_b^3 - Q_b s_W^2) - m_{\tilde{b}_2}^2} \\ &\quad - m_{\tilde{b}}^2 - M_Z^2 c_{2\beta} Q_b s_W^2 + m_{\tilde{b}_2}^2. \end{aligned} \quad (50)$$

⁶It can be found, up to $\mathcal{O}(\alpha_s)$ in Eq. (8.43) of [40].

⁷If the mass of the \tilde{b}_1 squark is chosen as independent mass as $\tilde{b}_2 \approx \tilde{b}_L$ then the shift of $M_{\tilde{b}_R}$ has to be performed with respect to $m_{\tilde{b}_1}$.

Taking into account this shift in $M_{\tilde{b}_R}$, up to one-loop order,⁸ the resulting mass parameter $m_{\tilde{b}_1}$ is the same as the on-shell mass Eq. (45).

In the top and bottom quark/squark sector the counterterm for the trilinear top coupling δA_t and the counterterm δY_b are given as a combination of the independent parameters that can be derived from the relation of Eqs. (16) and (21),

$$\begin{aligned} \delta A_t &= \frac{1}{m_t} [U_{\tilde{t}_{11}} U_{\tilde{t}_{12}}^* (\delta m_{\tilde{t}_1}^2 - \delta m_{\tilde{t}_2}^2) + U_{\tilde{t}_{11}} U_{\tilde{t}_{22}}^* \delta Y_t^* \\ &\quad + U_{\tilde{t}_{12}}^* U_{\tilde{t}_{21}} \delta Y_t - (A_t - \mu^* \cot\beta) \delta m_t] \\ &\quad + (\delta \mu^* \cot\beta - \mu^* \cot^2\beta \delta \tan\beta) \end{aligned} \quad (51)$$

and

$$\begin{aligned} \delta Y_b &= \frac{1}{|U_{\tilde{b}_{11}}|^2 - |U_{\tilde{b}_{12}}|^2} [U_{\tilde{b}_{11}} U_{\tilde{b}_{21}}^* (\delta m_{\tilde{b}_1}^2 - \delta m_{\tilde{b}_2}^2) \\ &\quad + m_b (U_{\tilde{b}_{11}} U_{\tilde{b}_{22}}^* (\delta A_b^* - \mu \delta \tan\beta - \tan\beta \delta \mu) \\ &\quad - U_{\tilde{b}_{12}} U_{\tilde{b}_{21}}^* (\delta A_b - \mu^* \delta \tan\beta - \tan\beta \delta \mu^*)) \\ &\quad + (U_{\tilde{b}_{11}} U_{\tilde{b}_{22}}^* (A_b^* - \mu \tan\beta) \\ &\quad - U_{\tilde{b}_{12}} U_{\tilde{b}_{21}}^* (A_b - \mu^* \tan\beta)) \delta m_b^{\overline{\text{DR}}}], \end{aligned} \quad (52)$$

where $\delta \tan\beta$ and $\delta \mu$ will be defined within the Higgs/gauge sector in Sec. II B, Eq. (120c) and the chargino/neutralino sector in II C, Eq. (181), respectively.

Now, the parameter renormalization for the top and bottom quark/squark sector is accomplished but the field renormalization still has to be done. We determine the Z factors of the quark and squark fields in the OS scheme. In the quark sector we have

$$\widetilde{\text{Re}}\hat{\Sigma}_q(p)q(p)|_{p^2=m_q^2} = 0, \quad (53)$$

$$\lim_{p^2 \rightarrow m_q^2} \frac{(\not{p} + m_q) \widetilde{\text{Re}}\hat{\Sigma}_q(p)}{p^2 - m_q^2} q(p) = 0, \quad (54)$$

where these two equations determine not only the quark mass counterterms [see Eqs. (37) and (40)] and the real part of the Z factors but also the difference of the imaginary parts of the quark Z factors, $\text{Im}\delta Z_q^L - \text{Im}\delta Z_q^R$ (analogously to the chargino/neutralino case in Sec. II C). This leaves us the freedom to impose additionally

$$\text{Im}\delta Z_q^L = -\text{Im}\delta Z_q^R. \quad (55)$$

With these equations we find

⁸In the case of a pure OS scheme (see e.g. [42,43] for the rMSSM) the shifts Eqs. (48) and (50) result in a mass parameter $m_{\tilde{b}_1}$, which is exactly the same as in Eq. (45). This constitutes an important consistency check of these two different methods.

$$\begin{aligned} \text{Re}\delta Z_q^{L/R} = & -\widetilde{\text{Re}}\{\Sigma_q^{L/R}(m_q^2) + m_q^2[\Sigma_q^{L'}(m_q^2) + \Sigma_q^{R'}(m_q^2)] \\ & + m_q[\Sigma_q^{SL'}(m_q^2) + \Sigma_q^{SR'}(m_q^2)]\}, \end{aligned} \quad (56)$$

$$\begin{aligned} \text{Im}\delta Z_q^{L/R} = & \pm \frac{i}{2m_q} \widetilde{\text{Re}}\{\Sigma_q^{SR}(m_q^2) - \Sigma_q^{SL}(m_q^2)\} \\ = & \pm \frac{1}{m_q} \text{Im}\{\widetilde{\text{Re}}\Sigma_q^{SL}(m_q^2)\}. \end{aligned} \quad (57)$$

For the scalar quarks we demand

$$\widetilde{\text{Re}}\hat{\Sigma}_{\tilde{q}ii}^{\prime}(p^2)|_{p^2=m_{\tilde{q}_i}^2} = 0 \quad (i = 1, 2), \quad (58)$$

$$\begin{aligned} \widetilde{\text{Re}}\hat{\Sigma}_{\tilde{q}_{12}}(m_{\tilde{q}_1}^2) = \widetilde{\text{Re}}\hat{\Sigma}_{\tilde{q}_{21}}(m_{\tilde{q}_1}^2) = 0, \\ \widetilde{\text{Re}}\hat{\Sigma}_{\tilde{q}_{12}}(m_{\tilde{q}_2}^2) = \widetilde{\text{Re}}\hat{\Sigma}_{\tilde{q}_{21}}(m_{\tilde{q}_2}^2) = 0, \end{aligned} \quad (59)$$

yielding

$$\text{Re}[\delta Z_{\tilde{q}}]_{ii} = -\widetilde{\text{Re}}\Sigma_{\tilde{q}ii}^{\prime}(p^2)|_{p^2=m_{\tilde{q}_i}^2} \quad (i = 1, 2), \quad (60)$$

$$\begin{aligned} [\delta Z_{\tilde{q}}]_{12} = & +2 \frac{\widetilde{\text{Re}}\hat{\Sigma}_{\tilde{q}_{12}}(m_{\tilde{q}_2}^2) - \delta Y_q}{(m_{\tilde{q}_1}^2 - m_{\tilde{q}_2}^2)}, \\ [\delta Z_{\tilde{q}}]_{21} = & -2 \frac{\widetilde{\text{Re}}\hat{\Sigma}_{\tilde{q}_{21}}(m_{\tilde{q}_1}^2) - \delta Y_q^*}{(m_{\tilde{q}_1}^2 - m_{\tilde{q}_2}^2)}, \end{aligned} \quad (61)$$

with $\Sigma^{\prime}(p^2) \equiv \frac{\partial \Sigma(p^2)}{\partial p^2}$, $q = \{t, b\}$, and $\tilde{q} = \{\tilde{t}, \tilde{b}\}$. It should be noted that the on-shell conditions leave the imaginary part of $[\delta Z_{\tilde{q}}]_{ii}$ undefined; it can be (implicitly) set to zero as it does not contain any divergences,

$$\text{Im}[\delta Z_{\tilde{q}}]_{ii} = 0 \quad (i = 1, 2). \quad (62)$$

The input parameters in the b/\tilde{b} sector have to correspond to the chosen renormalization. We start by defining the bottom mass, where the experimental input is the SM $\overline{\text{MS}}$ mass [44],

$$m_b^{\overline{\text{MS}}}(m_b) = 4.2 \text{ GeV}. \quad (63)$$

The value of $m_b^{\overline{\text{MS}}}(\mu_R)$ (at the renormalization scale $\mu_R = m_{\tilde{t}_2}$) is calculated from $m_b^{\overline{\text{MS}}}(m_b)$ at the three-loop level following the prescription given in Ref. [45].

The ‘‘on-shell’’ mass is connected to the $\overline{\text{MS}}$ mass via

$$m_b^{\text{os}} = m_b^{\overline{\text{MS}}}(\mu_R) \left[1 + \frac{\alpha_s^{\overline{\text{MS}}}(\mu_R)}{\pi} \left(\frac{4}{3} + 2 \ln \frac{\mu_R}{m_b^{\overline{\text{MS}}}(\mu_R)} \right) \right]. \quad (64)$$

The $\overline{\text{DR}}$ bottom quark mass at the scale μ_R is calculated iteratively from [40,43,46]

$$m_b^{\overline{\text{DR}}} = \frac{m_b^{\text{os}} |1 + \Delta_b| + \delta m_b^{\text{OS}} - \delta m_b^{\overline{\text{DR}}}}{|1 + \Delta_b|} \quad (65)$$

with an accuracy of $|1 - (m_b^{\overline{\text{DR}}})^n / (m_b^{\overline{\text{DR}}})^{(n-1)}| < 10^{-5}$ reached in the n th step of the iteration where $\delta m_b^{\overline{\text{DR}}}$ and δm_b^{OS} are given in Eqs. (39) and (41), respectively.

The quantity Δ_b [46–48] resums the $\mathcal{O}((\alpha_s \tan\beta)^n)$ and $\mathcal{O}((\alpha_t \tan\beta)^n)$ terms and is given by

$$\begin{aligned} \Delta_b = & \frac{2\alpha_s(m_t)}{3\pi} \tan\beta M_3^* \mu^* I(m_{b_1}^2, m_{b_2}^2, m_g^2) \\ & + \frac{\alpha_t(m_t)}{4\pi} \tan\beta A_t^* \mu^* I(m_{\tilde{t}_1}^2, m_{\tilde{t}_2}^2, |\mu|^2) \end{aligned} \quad (66)$$

with

$$I(a, b, c) = -\frac{ab \ln(b/a) + ac \ln(a/c) + bc \ln(c/b)}{(a-c)(c-b)(b-a)}. \quad (67)$$

Here α_t is defined in terms of the top Yukawa coupling $y_t(m_t) = \sqrt{2}m_t(m_t)/v$ as $\alpha_t(m_t) = y_t^2(m_t)/(4\pi)$ with $v = 1/\sqrt{2}G_F = 246.218 \text{ GeV}$ and $m_t(m_t) \approx m_t/(1 - \frac{1}{2\pi}\alpha_t(m_t) + \frac{4}{3\pi}\alpha_s(m_t))$. Setting in the evaluation of Δ_b the scale to m_t was shown to yield in general a more stable result [49] as long as two-loop corrections to Δ_b are not included.⁹ M_3 is the soft SUSY-breaking parameter for the gluinos; see below. We have neglected any CKM mixing of the quarks.

2. The gluino sector

The gluinos appear as external particles, for instance, in the decay $\tilde{t}_2 \rightarrow t\tilde{g}$. Therefore, a renormalization procedure for the gluino field and the corresponding parameters is necessary.

The Fourier transformed Lagrangian bilinear in the gluino fields is given by

$$\begin{aligned} \mathcal{L}_{\tilde{g}_{\text{org}}}^{\text{bil}} = & \tilde{g}_{\text{org}}^a \not{p} \omega - \tilde{g}_{\text{org}}^a + \tilde{g}_{\text{org}}^a \not{p} \omega + \tilde{g}_{\text{org}}^a - \tilde{g}_{\text{org}}^a M_3 \omega - \tilde{g}_{\text{org}}^a \\ & - \tilde{g}_{\text{org}}^a M_3^* \omega + \tilde{g}_{\text{org}}^a \end{aligned} \quad (68)$$

with M_3 being the soft-breaking gluino mass parameter, which is in general complex,

$$M_3 = |M_3| e^{i\varphi_{\tilde{g}}}. \quad (69)$$

The gluino field \tilde{g}_{org}^a can be redefined using a phase transformation

$$\omega_{\pm} \tilde{g}^a = e^{\mp i(\varphi_{\tilde{g}}/2)} \omega_{\pm} \tilde{g}_{\text{org}}^a \quad (70)$$

such that the gluino phase $\varphi_{\tilde{g}}$ appears only in the gluino couplings, but not in the mass term with the gluino mass $m_{\tilde{g}} = |M_3|$.

⁹It should be noted that in Ref. [49] a different scale has been advocated due to the emphasis on the two-loop contributions presented in this paper. The plots, however, show that m_t is a good scale choice if only one-loop corrections are included.

The renormalization is performed as follows [50]:

$$\begin{aligned} M_3 &\rightarrow M_3 + \delta M_3 = M_3 + \delta|M_3|e^{i\varphi_{\tilde{g}}} + iM_3\delta\varphi_{\tilde{g}}, \\ \omega_- \tilde{g}^a &\rightarrow \left(1 + \frac{1}{2}\delta Z_{\tilde{g}}\right)\omega_- \tilde{g}^a, \\ \omega_+ \tilde{g}^a &\rightarrow \left(1 + \frac{1}{2}\delta Z_{\tilde{g}}^*\right)\omega_+ \tilde{g}^a. \end{aligned} \quad (71)$$

Note that, analogous to the mixing matrix, only the gluino phase appearing in M_3 is renormalized but not the one appearing due to the redefinition of the gluino field.

The renormalized gluino self-energies read

$$\hat{\Sigma}_{\tilde{g}}^{L/R}(p^2) = \Sigma_{\tilde{g}}^{L/R}(p^2) + \frac{1}{2}(\delta Z_{\tilde{g}} + \delta Z_{\tilde{g}}^*), \quad (72)$$

$$\hat{\Sigma}_{\tilde{g}}^{SL}(p^2) = \Sigma_{\tilde{g}}^{SL}(p^2) - m_{\tilde{g}}\delta Z_{\tilde{g}} - \delta M_3 e^{-i\varphi_{\tilde{g}}}, \quad (73)$$

$$\hat{\Sigma}_{\tilde{g}}^{SR}(p^2) = \Sigma_{\tilde{g}}^{SR}(p^2) - m_{\tilde{g}}\delta Z_{\tilde{g}}^* - \delta M_3^* e^{i\varphi_{\tilde{g}}}. \quad (74)$$

We choose OS renormalization conditions for the gluino,

$$\widetilde{\text{Re}}\hat{\Sigma}_{\tilde{g}}(p)\tilde{g}^a(p)|_{p^2=m_{\tilde{g}}^2} = 0, \quad (75)$$

$$\lim_{p^2 \rightarrow m_{\tilde{g}}^2} \frac{(\not{p} + m_{\tilde{g}})\hat{\Sigma}_{\tilde{g}}(p)}{p^2 - m_{\tilde{g}}^2} \tilde{g}^a(p) = 0, \quad (76)$$

with $\hat{\Sigma}(p)$ defined according to Eq. (29). Because of the Majorana nature of the gluino this leads to three independent conditions, yielding—with $\Sigma'(m^2) \equiv \frac{\partial \Sigma(p^2)}{\partial p^2}|_{p^2=m^2}$ —

$$\begin{aligned} \delta|M_3| &= \frac{1}{2}\widetilde{\text{Re}}\{m_{\tilde{g}}[\Sigma_{\tilde{g}}^L(m_{\tilde{g}}^2) + \Sigma_{\tilde{g}}^R(m_{\tilde{g}}^2)] \\ &\quad + [\Sigma_{\tilde{g}}^{SL}(m_{\tilde{g}}^2) + \Sigma_{\tilde{g}}^{SR}(m_{\tilde{g}}^2)]\}, \end{aligned} \quad (77)$$

$$\begin{aligned} \text{Re}\delta Z_{\tilde{g}} &= -\widetilde{\text{Re}}\{[\Sigma_{\tilde{g}}^L(m_{\tilde{g}}^2) + m_{\tilde{g}}^2[\Sigma_{\tilde{g}}^{L'}(m_{\tilde{g}}^2) + \Sigma_{\tilde{g}}^{R'}(m_{\tilde{g}}^2)] \\ &\quad + m_{\tilde{g}}[\Sigma_{\tilde{g}}^{SL'}(m_{\tilde{g}}^2) + \Sigma_{\tilde{g}}^{SR'}(m_{\tilde{g}}^2)]\}, \end{aligned} \quad (78)$$

$$\text{Im}\delta Z_{\tilde{g}} = \frac{i}{2m_{\tilde{g}}}\widetilde{\text{Re}}\{\Sigma_{\tilde{g}}^{SR}(m_{\tilde{g}}^2) - \Sigma_{\tilde{g}}^{SL}(m_{\tilde{g}}^2)\} - \delta\varphi_{\tilde{g}}. \quad (79)$$

We have then chosen $\delta\varphi_{\tilde{g}} = 0$, which is similar to the quark case: There, we use a real Yukawa coupling due to the possibility of redefining the quark fields and have a complex Z factor at one-loop order that keeps the Yukawa coupling real also at one-loop order; in contrast the gluino phase still appears in the Lagrangian after the redefinition of the fields but this phase factor can be considered as a “transformation matrix” and does not obtain a counterterm. Note that in the chargino/neutralino sector we keep the diagonal Z factors real and have complex parameters.

3. The strong coupling constant

The strong coupling constant is renormalized as

$$\alpha_s \rightarrow Z_{\alpha_s} \alpha_s = (1 + \delta Z_{\alpha_s}) \alpha_s. \quad (80)$$

For Z_{α_s} we are using a $\overline{\text{DR}}$ renormalization condition yielding

$$\delta Z_{\alpha_s} = -\frac{1}{2}\Sigma_{GG}^{T'}(p^2)|_{p^2=0,\text{div}}, \quad (81)$$

where $\Sigma_{GG}^{T'}$ denotes the derivative of the transverse part of the gluon self-energy.

The decoupling of the heavy particles and the running is taken into account in the definition of α_s : starting point is [44]

$$\alpha_s^{\overline{\text{MS}},(5)}(M_Z) = 0.1176, \quad (82)$$

where the running of $\alpha_s^{\overline{\text{MS}},(n_f)}(\mu_R)$ can be found in Ref. [44]. From the $\overline{\text{MS}}$ value the $\overline{\text{DR}}$ value is obtained at the two-loop level via [51]

$$\begin{aligned} \alpha_s^{\overline{\text{DR}},(n_f)}(\mu_R) &= \alpha_s^{\overline{\text{MS}},(n_f)}(\mu_R) \left[1 + \frac{\alpha_s^{\overline{\text{MS}},(n_f)}(\mu_R)}{4\pi} \right. \\ &\quad \left. + \left(\frac{\alpha_s^{\overline{\text{MS}},(n_f)}(\mu_R)}{\pi} \right)^2 \left(\frac{11}{8} - \frac{n_f}{12} \right) \right]. \end{aligned} \quad (83)$$

For $\mu_R > m_t$ we have $n_f = 6$. Within the MSSM, at one-loop level, α_s reads

$$\begin{aligned} \alpha_s^{\text{MSSM}}(\mu_R) &= \alpha_s^{\overline{\text{DR}},(6)}(\mu_R) \left[1 + \frac{\alpha_s^{\overline{\text{DR}},(6)}(\mu_R)}{\pi} \left(\ln \frac{\mu_R}{m_{\tilde{g}}} + \ln \frac{\mu_R}{M_{\tilde{q}}} \right) \right], \end{aligned} \quad (84)$$

with $M_{\tilde{q}}$ being defined as the geometric average of all squark masses, $M_{\tilde{q}} = \Pi_{\tilde{q}}(m_{\tilde{q}_1} m_{\tilde{q}_2})^{(1/12)}$. The log terms originate from the decoupling of the SQCD particles from the running of α_s at lower scales $\mu_R \leq \mu_{\text{dec}} = m_{\tilde{t}_2}$. For simplification we have chosen $m_{\tilde{t}_2}$ (representing the energy scale of the considered decays and as a typical SUSY scale) also as a decoupling scale.

B. The Higgs and gauge boson sector of the cMSSM

The MSSM Higgs potential V_H ,

$$\begin{aligned} V_H &= m_1^2 H_{1i}^* H_{1i} + m_2^2 H_{2i}^* H_{2i} - \epsilon^{ij} (m_{12}^2 H_{1i} H_{2j} \\ &\quad + m_{12}^{*2} H_{1i}^* H_{2j}^*) + \frac{1}{8} (g_1^2 + g_2^2) (H_{1i}^* H_{1i} - H_{2i}^* H_{2i})^2 \\ &\quad + \frac{1}{2} g_2^2 |H_{1i}^* H_{2i}|^2 \end{aligned} \quad (85)$$

with $\{i, j\} = \{1, 2\}$ and $\epsilon^{12} = 1$, contains both the $U(1)$ and $SU(2)_L$ gauge coupling constants g_1 and g_2 , respectively, which are considered to be part of the gauge boson sector as well as the soft SUSY-breaking parameters m_{12} , \tilde{m}_1^2 , and \tilde{m}_2^2 (with $m_1^2 \equiv \tilde{m}_1^2 + |\mu|^2$, $m_2^2 \equiv \tilde{m}_2^2 + |\mu|^2$), which are part of the Higgs sector. For this reason we do not separate those two sectors but treat them within one section. The H_{ij} with $\{i, j\} = \{1, 2\}$ are the components of the two Higgs doublets that can be decomposed in the following way:

$$\begin{aligned}\mathcal{H}_1 &= \begin{pmatrix} H_{11} \\ H_{12} \end{pmatrix} = \begin{pmatrix} v_1 + \frac{1}{\sqrt{2}}(\phi_1 - i\chi_1) \\ -\phi_1^- \end{pmatrix}, \\ \mathcal{H}_2 &= \begin{pmatrix} H_{21} \\ H_{22} \end{pmatrix} = e^{i\xi} \begin{pmatrix} \phi_2^+ \\ v_2 + \frac{1}{\sqrt{2}}(\phi_2 + i\chi_2) \end{pmatrix}.\end{aligned}\quad (86)$$

Besides the vacuum expectation values v_1 and v_2 , in Eq. (86) a possible new phase ξ between the two Higgs doublets is introduced.

$$\begin{aligned}\mathcal{L}_{\text{Higgs}}^{\text{gauge}} &= T_{\phi_1}\phi_1 + T_{\phi_2}\phi_2 + T_{\chi_1}\chi_1 + T_{\chi_2}\chi_2 + \frac{1}{2}(\phi_1, \phi_2, \chi_1, \chi_2)(p^2\mathbb{1} - \mathbf{M}_{\phi\phi\chi\chi}) \begin{pmatrix} \phi_1 \\ \phi_2 \\ \chi_1 \\ \chi_2 \end{pmatrix} \\ &+ (\phi_1^+, \phi_2^+)(p^2\mathbb{1} - \mathbf{M}_{\phi^\pm\phi^\pm}^\top) \begin{pmatrix} \phi_1^- \\ \phi_2^- \end{pmatrix} - \frac{1}{2}Z_\mu[(p^2 - M_Z^2)g^{\mu\nu} - \left(1 - \frac{1}{\xi_Z}\right)p^\mu p^\nu]Z_\nu - \frac{g_2}{\sqrt{2}c_W}ip^\mu(v_1\chi_1 + v_2\chi_2)Z_\mu \\ &+ ip^\mu M_Z Z_\mu G - \frac{1}{2}\xi_Z M_Z^2 G^2 - W_\mu^+[(p^2 - M_W^2)g^{\mu\nu} - \left(1 - \frac{1}{\xi_W}\right)p^\mu p^\nu]W_\nu^- + \frac{g_2}{\sqrt{2}}p^\mu[W_\mu^+(v_1\phi_1^- + v_2\phi_2^-) \\ &+ (v_1\phi_1^+ + v_2\phi_2^+)W_\mu^-] - p^\mu M_W(W_\mu^+ G^- + G^+ W_\mu^-) - \xi_W M_W^2 G^+ G^-, \end{aligned}\quad (87)$$

where we have used the decomposition of Eq. (86). The coefficients of the linear terms are called tadpoles with T_{ϕ_i} , T_{χ_i} , $i = \{1, 2\}$ being the tadpole parameters. $\mathbf{M}_{\phi\phi\chi\chi}$ and $\mathbf{M}_{\phi^\pm\phi^\pm}$ are the Higgs mass matrices. The terms containing the neutral and the charged Goldstone boson fields, G and G^\pm , and the gauge parameters, ξ_Z and ξ_W , respectively, are coming from the gauge-fixing part of the Lagrangian. The interaction fields can be transformed into mass eigenstates (see Refs. [37,40,54] for details, especially on notation) with the help of the real and orthogonal transformation matrices $\mathbf{U}_{n(0)}$ and $\mathbf{U}_{c(0)}$,

$$\begin{aligned}\begin{pmatrix} h \\ H \\ A \\ G \end{pmatrix} &= \mathbf{U}_{n(0)} \begin{pmatrix} \phi_1 \\ \phi_2 \\ \chi_1 \\ \chi_2 \end{pmatrix} \quad \text{with} \\ \mathbf{M}_{hHAG}^{\text{diag}} &= \mathbf{U}_{n(0)} \mathbf{M}_{\phi\phi\chi\chi} \mathbf{U}_{n(0)}^\dagger,\end{aligned}\quad (88)$$

and

$$\begin{aligned}(T_h, T_H, T_A, T_G) &= (T_{\phi_1}, T_{\phi_2}, T_{\chi_1}, T_{\chi_2}) \mathbf{U}_{n(0)}^\dagger, \\ \begin{pmatrix} H^- \\ G^- \end{pmatrix} &= \mathbf{U}_{c(0)} \begin{pmatrix} \phi_1^- \\ \phi_2^- \end{pmatrix} \quad \text{with} \\ \mathbf{M}_{H^\pm G^\pm}^{\text{diag}} &= \mathbf{U}_{c(0)} \mathbf{M}_{\phi^\pm\phi^\pm}^\top \mathbf{U}_{c(0)}^\dagger,\end{aligned}\quad (89)$$

¹⁰Corresponding to the convention used in FEYNARTS/FORMCALC, we exchanged in the charged part the positive Higgs fields with the negative ones, which is in contrast to [37]. As we keep the definition of the matrix $\mathbf{M}_{\phi^\pm\phi^\pm}$ used in [37] the transposed matrix will appear in the expression for $\mathbf{M}_{H^\pm G^\pm}^{\text{diag}}$; see below.

In total, the Higgs and gauge boson sector contains 7 real parameters: $g_1, g_2, \tilde{m}_1^2, \tilde{m}_2^2, v_1, v_2$, and ξ and one complex one m_{12} . μ is defined within the chargino/neutralino sector; see Sec. II C. With the help of a Peccei-Quinn transformation [52] μ and m_{12}^2 can be redefined [53] such that the complex phase of m_{12}^2 vanishes.

The part of the Fourier transformed Lagrangian that is linear or bilinear in the massive gauge boson and Higgs boson fields is the following¹⁰:

where the diagonal elements of $\mathbf{M}_{hHAG}^{\text{diag}}$ and $\mathbf{M}_{H^\pm G^\pm}^{\text{diag}}$ are the tree-level masses denoted as m_h, m_H, m_A, m_G and M_{H^\pm}, m_{G^\pm} , respectively. It should be noted that the tadpole parameter T_G can be expressed by $\tan\beta$, the entries of $\mathbf{U}_{n(0)}$ and T_A .

Throughout our calculation we use the 't Hooft-Feynman gauge, $\xi_Z = \xi_W = 1$. Concerning the renormalization procedure, we follow the usual approach where the gauge-fixing terms do not receive a net contribution from the renormalization transformations. Accordingly, no counterterms as given below arise from the gauge-fixing terms.

We replace the 8 original parameters $v_1, v_2, g_1, g_2, m_{12}^2, \tilde{m}_1^2, \tilde{m}_2^2$, and ξ by the Z and W boson mass M_Z, M_W , the electric charge e , $\tan\beta$, the mass of the charged Higgs boson M_{H^\pm} , and the tadpole parameters T_h, T_H , and T_A (where we have chosen m_{12}^2 to be real, which is always possible with the help of a Peccei-Quinn transformation). Details about this replacement can be found in Ref. [37].

The minimization of the Higgs potential in lowest order leads to the requirement that the tadpole coefficients $T_{\{h,H,A\}}$ in Eq. (87) must vanish (the tadpole coefficient T_G vanishes automatically if $T_A = 0$ holds, as T_G can be written in terms of T_A). In particular, the condition $T_A = 0$ implies that the complex phase ξ has to vanish, see e.g. Ref. [37], so that the Higgs sector in lowest order is \mathcal{CP} conserving.

In order to derive the counterterms entering the one-loop corrections to the Higgs boson masses and effective couplings, we renormalize the parameters appearing in the linear and bilinear terms of the Higgs potential,¹¹

¹¹It should be noted that in Ref. [37] a slightly different renormalization prescription for $\tan\beta$ had been introduced, $\tan\beta \rightarrow \tan\beta(1 + \delta \tan\beta^{[37]})$, such that $\delta \tan\beta = \tan\beta \delta \tan\beta^{[37]}$.

$$\begin{aligned}
e &\rightarrow (1 + \delta Z_e)e, & M_{H^\pm}^2 &\rightarrow M_{H^\pm}^2 + \delta m_{H^\pm}^2 \\
M_Z^2 &\rightarrow M_Z^2 + \delta M_Z^2, & T_h &\rightarrow T_h + \delta T_h, \\
M_W^2 &\rightarrow M_W^2 + \delta M_W^2, & T_H &\rightarrow T_H + \delta T_H, \\
\tan\beta &\rightarrow \tan\beta + \delta \tan\beta & T_A &\rightarrow T_A + \delta T_A.
\end{aligned} \tag{91}$$

It is important that according to our renormalization procedure the renormalization prescription has to be applied *before* the transformation into the mass eigenstates, also for $\tan\beta$, i.e. a β appearing from the transformation to the fields A , G , H^\pm , and G^\pm does not obtain a counterterm. For the counterterms arising from the mass matrices we use the definitions [37]

$$\mathbf{M}_{\phi\phi\chi\chi} \rightarrow \mathbf{M}_{\phi\phi\chi\chi} + \delta\mathbf{M}_{\phi\phi\chi\chi}, \tag{92}$$

$$\mathbf{M}_{\phi^\pm\phi^\pm} \rightarrow \mathbf{M}_{\phi^\pm\phi^\pm} + \delta\mathbf{M}_{\phi^\pm\phi^\pm}, \tag{93}$$

with

$$\begin{aligned}
\delta\mathbf{M}_{hHAG} &= \mathbf{U}_{n(0)} \delta\mathbf{M}_{\phi\phi\chi\chi} \mathbf{U}_{n(0)}^\dagger \\
&= \begin{pmatrix} \delta m_h^2 & \delta m_{hH}^2 & \delta m_{hA}^2 & \delta m_{hG}^2 \\ \delta m_{hH}^2 & \delta m_H^2 & \delta m_{HA}^2 & \delta m_{HG}^2 \\ \delta m_{hA}^2 & \delta m_{HA}^2 & \delta m_A^2 & \delta m_{AG}^2 \\ \delta m_{hG}^2 & \delta m_{HG}^2 & \delta m_{AG}^2 & \delta m_G^2 \end{pmatrix}, \tag{94}
\end{aligned}$$

$$\begin{aligned}
\delta\mathbf{M}_{H^\pm G^\pm} &= \mathbf{U}_{c(0)} \delta\mathbf{M}_{\phi^\pm\phi^\pm}^\top \mathbf{U}_{c(0)}^\dagger \\
&= \begin{pmatrix} \delta m_{H^\pm}^2 & \delta m_{G^-H^+}^2 \\ \delta m_{H^-G^+}^2 & \delta m_{G^\pm}^2 \end{pmatrix}, \tag{95}
\end{aligned}$$

where $\delta\mathbf{M}_{\phi\phi\chi\chi}$ and $\delta\mathbf{M}_{\phi^\pm\phi^\pm}$ denote the counterterm mass matrices that are obtained when replacing the parameters in $\mathbf{M}_{\phi\phi\chi\chi}$ and $\mathbf{M}_{\phi^\pm\phi^\pm}$ by the renormalized ones and their counterterms using Eq. (91), expanding and taking the first-order expressions and applying the zeroth order relation $T_{\{h,H,A\}} = 0$; see Ref. [37].

As mentioned above, in contrast to what is often done in the MSSM with real parameters, we use M_{H^\pm} as an independent input parameter. The counterterm δm_A^2 in the formulas above is therefore a dependent quantity, which has to be expressed in terms of $\delta m_{H^\pm}^2$ using

$$\delta m_A^2 = \delta m_{H^\pm}^2 - \delta M_W^2. \tag{96}$$

For the field renormalization we choose to give each Higgs doublet one single renormalization constant,

$$\begin{aligned}
\mathcal{H}_1 &\rightarrow \left(1 + \frac{1}{2} \delta Z_{\mathcal{H}_1}\right) \mathcal{H}_1, \\
\mathcal{H}_2 &\rightarrow \left(1 + \frac{1}{2} \delta Z_{\mathcal{H}_2}\right) \mathcal{H}_2.
\end{aligned} \tag{97}$$

In the mass eigenstate basis, the field renormalization matrices read

$$\begin{aligned}
\begin{pmatrix} h \\ H \\ A \\ G \end{pmatrix} &\rightarrow \begin{pmatrix} h \\ H \\ A \\ G \end{pmatrix} \\
&+ \frac{1}{2} \begin{pmatrix} \delta Z_{hh} & \delta Z_{hH} & \delta Z_{hA} & \delta Z_{hG} \\ \delta Z_{hH} & \delta Z_{HH} & \delta Z_{HA} & \delta Z_{HG} \\ \delta Z_{hA} & \delta Z_{HA} & \delta Z_{AA} & \delta Z_{AG} \\ \delta Z_{hG} & \delta Z_{HG} & \delta Z_{AG} & \delta Z_{GG} \end{pmatrix} \cdot \begin{pmatrix} h \\ H \\ A \\ G \end{pmatrix}
\end{aligned} \tag{98a}$$

and

$$\begin{pmatrix} H^- \\ G^- \end{pmatrix} \rightarrow \begin{pmatrix} H^- \\ G^- \end{pmatrix} + \frac{1}{2} \begin{pmatrix} \delta Z_{H^-H^+} & \delta Z_{G^-H^+} \\ \delta Z_{H^-G^+} & \delta Z_{G^-G^+} \end{pmatrix} \cdot \begin{pmatrix} H^- \\ G^- \end{pmatrix}, \tag{98b}$$

where, according to (97), $\delta Z_{hh}, \dots, \delta Z_{G^-G^+}$ are not independent but can be derived via $\mathbf{U}_{n(0)} \mathbf{diag}(\delta Z_{\mathcal{H}_1}, \delta Z_{\mathcal{H}_2}, \delta Z_{\mathcal{H}_1}, \delta Z_{\mathcal{H}_2}) \mathbf{U}_{n(0)}^\dagger$ and $\mathbf{U}_{c(0)} \mathbf{diag}(\delta Z_{\mathcal{H}_1}, \delta Z_{\mathcal{H}_2}) \mathbf{U}_{c(0)}^\dagger$, yielding the following expressions for the field renormalization constants in Eq. (98)¹²:

$$\delta Z_{hh} = \sin^2\alpha \delta Z_{\mathcal{H}_1} + \cos^2\alpha \delta Z_{\mathcal{H}_2}, \tag{99a}$$

$$\delta Z_{AA} = \sin^2\beta \delta Z_{\mathcal{H}_1} + \cos^2\beta \delta Z_{\mathcal{H}_2}, \tag{99b}$$

$$\delta Z_{hH} = \sin\alpha \cos\alpha (\delta Z_{\mathcal{H}_2} - \delta Z_{\mathcal{H}_1}), \tag{99c}$$

$$\delta Z_{AG} = \sin\beta \cos\beta (\delta Z_{\mathcal{H}_2} - \delta Z_{\mathcal{H}_1}), \tag{99d}$$

$$\delta Z_{HH} = \cos^2\alpha \delta Z_{\mathcal{H}_1} + \sin^2\alpha \delta Z_{\mathcal{H}_2}, \tag{99e}$$

$$\delta Z_{GG} = \cos^2\beta \delta Z_{\mathcal{H}_1} + \sin^2\beta \delta Z_{\mathcal{H}_2}, \tag{99f}$$

$$\delta Z_{H^-H^+} = \delta Z_{AA}, \tag{99g}$$

$$\delta Z_{H^-G^+} = \delta Z_{G^-H^+} = \delta Z_{AG}, \tag{99h}$$

$$\delta Z_{G^-G^+} = \delta Z_{GG}. \tag{99i}$$

For the field renormalization constants of the \mathcal{CP} -violating self-energies it follows,

$$\delta Z_{hA} = \delta Z_{hG} = \delta Z_{HA} = \delta Z_{HG} = 0, \tag{100}$$

which is related to the fact that the Higgs potential is \mathcal{CP} conserving in lowest order.

In the case of a decay to a neutral or charged Higgs boson some self-energy transitions on the external Higgs leg have to be taken into account. In order to define the various counterterm contributions, we list here the respective renormalized self-energies [taking already Eq. (100) into account]. For a scalar-vector self-energy we use $\Sigma_{\text{SV}}^\mu(p^\mu) = p^\mu \Sigma_{\text{SV}}(p^2)$, where p^μ is the momentum of

¹²It should be noted that (99g) is sufficient to yield an UV-finite result for decays involving a charged Higgs boson. To obtain also an IR finite result and to ensure the on-shell properties of the outgoing charged Higgs boson, another Z factor has to be taken into account; see Eq. (134) below.

the incoming scalar or vector particle. Then we have the following renormalized self-energies:

$$\hat{\Sigma}_{hG}(p^2) = \Sigma_{hG}(p^2) - \delta m_{hG}^2, \quad (101)$$

$$\hat{\Sigma}_{HG}(p^2) = \Sigma_{HG}(p^2) - \delta m_{HG}^2, \quad (102)$$

$$\hat{\Sigma}_{AG}(p^2) = \Sigma_{AG}(p^2) + \delta Z_{AG} \left(p^2 - \frac{1}{2} m_A^2 \right) - \delta m_{AG}^2, \quad (103)$$

$$\hat{\Sigma}_{H^-G^+}(p^2) = \Sigma_{H^-G^+}(p^2) + \delta Z_{H^-G^+} \left(p^2 - \frac{1}{2} M_{H^\pm}^2 \right) - \delta m_{H^-G^+}^2, \quad (104)$$

$$\hat{\Sigma}_{hZ}(p^2) = \Sigma_{hZ}(p^2), \quad (105)$$

$$\hat{\Sigma}_{HZ}(p^2) = \Sigma_{HZ}(p^2), \quad (106)$$

$$\hat{\Sigma}_{AZ}(p^2) = \Sigma_{AZ}(p^2) - \delta m_{AZ}^2, \quad (107)$$

$$\hat{\Sigma}_{H^-W^+}(p^2) = \Sigma_{H^-W^+}(p^2) - \delta m_{H^-W^+}^2, \quad (108)$$

with the mass counterterms expressed as [37]

$$\delta m_{hG}^2 = \frac{e \cos(\beta - \alpha)}{2M_Z s_W c_W} \delta T_A, \quad (109)$$

$$\delta m_{HG}^2 = -\frac{e \sin(\beta - \alpha)}{2M_Z s_W c_W} \delta T_A, \quad (110)$$

$$\delta m_{AG}^2 = \frac{e(\sin(\beta - \alpha)\delta T_H - \cos(\beta - \alpha)\delta T_h)}{2M_Z s_W c_W} - \cos^2 \beta (M_{H^\pm}^2 - M_W^2) \delta \tan \beta, \quad (111)$$

$$\delta m_{H^-G^+}^2 = \frac{e(\sin(\beta - \alpha)\delta T_H - \cos(\beta - \alpha)\delta T_h + i\delta T_A)}{2M_Z s_W c_W} - \cos^2 \beta M_{H^\pm}^2 \delta \tan \beta, \quad (112)$$

$$\delta m_{AZ}^2 = +iM_Z \cos \beta [\cos \beta \delta \tan \beta + \frac{1}{2} \sin \beta (\delta Z_{\mathcal{H}_2} - \delta Z_{\mathcal{H}_1})], \quad (113)$$

$$\delta m_{H^-W^+}^2 = -M_W \cos \beta [\cos \beta \delta \tan \beta + \frac{1}{2} \sin \beta (\delta Z_{\mathcal{H}_2} - \delta Z_{\mathcal{H}_1})]. \quad (114)$$

α denotes the angle that diagonalizes the \mathcal{CP} -even Higgs boson mass matrix at the tree level. It should be noted that according to Eq. (87), no mixing of the \mathcal{CP} -even Higgs fields and the Z boson fields occurs at tree level.

Consequently, there are no counterterm contributions to this mixing at one-loop level; see Eqs. (105) and (106).¹³

In the following we list our renormalization conditions and the resulting counterterms:

(i–iii) We impose on-shell renormalization conditions for the masses of the SM gauge bosons and the charged Higgs boson,

$$\begin{aligned} \widetilde{\text{Re}} \hat{\Sigma}_{ZZ}^T(M_Z^2) &= 0, & \widetilde{\text{Re}} \hat{\Sigma}_{WW}^T(M_W^2) &= 0, \\ \widetilde{\text{Re}} \hat{\Sigma}_{H^+H^-}^T(M_{H^\pm}^2) &= 0. \end{aligned} \quad (115)$$

The gauge boson self-energies Σ^T are the transverse parts of the full self-energies. Equation (115) yields for the mass counterterms,

$$\begin{aligned} \delta M_Z^2 &= \widetilde{\text{Re}} \Sigma_{ZZ}^T(M_Z^2), & \delta M_W^2 &= \widetilde{\text{Re}} \Sigma_{WW}^T(M_W^2), \\ \delta m_{H^\pm}^2 &= \widetilde{\text{Re}} \Sigma_{H^+H^-}^T(M_{H^\pm}^2). \end{aligned} \quad (116)$$

(iv) The electric charge is defined via the standard on-shell conditions requiring that no corrections occur to the electron-positron-photon vertex with on-shell external particles at zero photon momentum. This yields δZ_e expressed through the photon and photon- Z self-energies,

$$\delta Z_e = \frac{1}{2} \Sigma'_{\gamma\gamma}(0) + \frac{s_W}{c_W} \frac{\Sigma_{\gamma Z}(0)}{M_Z^2}. \quad (117)$$

(v–vii) The tadpole parameters are renormalized such that the complete one-loop tadpole contributions vanish,

$$T_{\{h,H,A\}}^{(1)} + \delta T_{\{h,H,A\}} = 0, \quad (118)$$

where $T_{\{h,H,A\}}^{(1)}$ denote the contributions coming from the genuine one-loop tadpole graphs. These conditions lead to

$$\delta T_h = -T_h^{(1)}, \quad \delta T_H = -T_H^{(1)}, \quad \delta T_A = -T_A^{(1)}. \quad (119)$$

(viii) The last parameter that has to be defined is $\tan \beta$. We do that together with the Higgs boson field renormalization constants $\delta Z_{\mathcal{H}_1}$ and $\delta Z_{\mathcal{H}_2}$.

A convenient choice that avoids large (and unphysically) higher-order corrections in the (c)MSSM Higgs sector is a $\overline{\text{DR}}$ renormalization of $\delta Z_{\mathcal{H}_1}$, $\delta Z_{\mathcal{H}_2}$, and $\delta \tan \beta$ [55],

$$\delta Z_{\mathcal{H}_1} \equiv \delta Z_{\mathcal{H}_1}^{\overline{\text{DR}}} = -\text{Re} \Sigma'_{HH}(0)|_{\alpha=0, \text{div}}, \quad (120a)$$

$$\delta Z_{\mathcal{H}_2} \equiv \delta Z_{\mathcal{H}_2}^{\overline{\text{DR}}} = -\text{Re} \Sigma'_{hh}(0)|_{\alpha=0, \text{div}}, \quad (120b)$$

$$\delta \tan \beta \equiv \delta \tan \beta^{\overline{\text{DR}}} = \frac{1}{2} \tan \beta (\delta Z_{\mathcal{H}_2} - \delta Z_{\mathcal{H}_1}), \quad (120c)$$

¹³The other renormalized Higgs boson self-energies, $\hat{\Sigma}_{hh}$, $\hat{\Sigma}_{hH}$, $\hat{\Sigma}_{HH}$, $\hat{\Sigma}_{AA}$, $\hat{\Sigma}_{GG}$, $\hat{\Sigma}_{hA}$, $\hat{\Sigma}_{HA}$, and $\hat{\Sigma}_{H^-H^+}$ and the corresponding mass matrix counterterm contributions, δm_h^2 , δm_H^2 , δm_{hH}^2 , δm_G^2 , δm_{hA}^2 , δm_{HA}^2 , are not explicitly needed in our calculation (employing FEYNHIGGS, these self-energy contributions are automatically taken care of). They are given by Eqs. (64) and (53) of Ref. [37], respectively, considering $\delta \tan \beta^{[37]} = \delta \tan \beta / \tan \beta$.

i.e. the counterterms in Eq. (120) contribute only via divergent parts,¹⁴ and the finite result depends on the renormalization scale μ_R . For the setting of μ_R see Sec. IV A.

The $\overline{\text{DR}}$ renormalization of the parameter $\tan\beta$, which is manifestly process independent, is convenient since there is no obvious relation of this parameter to a specific physical observable that would favor a particular on-shell definition. Furthermore, the $\overline{\text{DR}}$ renormalization of $\tan\beta$ has been shown to yield stable numerical results [55–57]. This scheme is also gauge independent at the one-loop level within the class of R_ξ gauges [56].

Finally, the field renormalization constants of the gauge bosons have to be determined. Applying an on-shell condition for the gauge boson fields, the field renormalization constants can be derived as

$$\delta Z_{ZZ} = -\widetilde{\text{Re}}\Sigma_{ZZ}^{T'}(M_Z^2), \quad \delta Z_{WW} = -\widetilde{\text{Re}}\Sigma_{WW}^{T'}(M_W^2). \quad (121)$$

In other sectors, one may need the following counterterms expressed by independent ones:

$$\delta s_W = \frac{1}{2} \frac{c_W^2}{s_W} \left(\frac{\delta M_Z^2}{M_Z^2} - \frac{\delta M_W^2}{M_W^2} \right), \quad (122)$$

$$\delta c_W = -\frac{c_W}{2} \left(\frac{\delta M_Z^2}{M_Z^2} - \frac{\delta M_W^2}{M_W^2} \right),$$

$$\delta \sin\beta = \cos^3\beta \delta \tan\beta, \quad (123)$$

$$\delta \cos\beta = -\sin\beta \cos^2\beta \delta \tan\beta.$$

We have checked (at the one-loop level) that the following Slavnov-Taylor identities [58–60] hold:

$$\hat{\Sigma}_{hG}(p^2) - \frac{ip^2}{M_Z} \hat{\Sigma}_{hZ}(p^2) = 0, \quad (124)$$

$$\hat{\Sigma}_{HG}(p^2) - \frac{ip^2}{M_Z} \hat{\Sigma}_{HZ}(p^2) = 0, \quad (125)$$

$$\hat{\Sigma}_{AG}(p^2) - \frac{ip^2}{M_Z} \hat{\Sigma}_{AZ}(p^2) + (p^2 - m_A^2) f_0(p^2) = 0, \quad (126)$$

$$\hat{\Sigma}_{GG}(p^2) - \frac{2ip^2}{M_Z} \hat{\Sigma}_{GZ}(p^2) - \frac{p^2}{M_Z^2} \hat{\Sigma}_{ZZ}^L(p^2) = 0, \quad (127)$$

$$\hat{\Sigma}_{H^-G^+}(p^2) - \frac{p^2}{M_W} \hat{\Sigma}_{H^-W^+}(p^2) + (p^2 - M_{H^\pm}^2) f_\pm(p^2) = 0, \quad (128)$$

$$\hat{\Sigma}_{G^-G^+}(p^2) - \frac{2p^2}{M_W} \hat{\Sigma}_{G^-W^+}(p^2) - \frac{p^2}{M_W^2} \hat{\Sigma}_{WW}^L(p^2) = 0, \quad (129)$$

¹⁴The divergences in Eqs. (120a) and (120b), are momentum independent.

where Σ^L denotes the longitudinal part of the self-energy and

$$f_0(p^2) = -\frac{\alpha}{16\pi s_W^2 c_W^2} \sin(\beta - \alpha) \cos(\beta - \alpha) \times [B_0(p^2, m_h^2, M_Z^2) - B_0(p^2, m_H^2, M_Z^2)], \quad (130)$$

$$f_\pm(p^2) = -\frac{\alpha}{16\pi s_W^2} \sin(\beta - \alpha) \cos(\beta - \alpha) \times [B_0(p^2, m_h^2, M_W^2) - B_0(p^2, m_H^2, M_W^2)]. \quad (131)$$

The definition for the B_0 function can be found in Ref. [61]. The Slavnov-Taylor identities also hold for the unrenormalized self-energies (where the tadpole contributions must not be neglected).

The Higgs boson field renormalization constants are necessary to render the one-loop calculations of partial decay widths with external Higgs bosons UV finite. The $\overline{\text{DR}}$ scheme for the field renormalization constants is used in the calculation of the Higgs masses within FEYNHIGGS in order to avoid the possible occurrence of unphysical threshold effects. As the results of FEYNHIGGS are used within the numerical evaluation in Sec. IV, it is appropriate and consistent to follow the same renormalization procedure. As always, Higgs bosons appearing as external particles in a physical process have to obey proper on-shell conditions. A vertex with an external on-shell Higgs boson h_n ($n = 1, 2, 3$), Γ_{h_n} , is obtained from the tree-level vertices Γ_h, Γ_H , and Γ_A via the complex matrix \mathbf{Z} [37],

$$\Gamma_{h_n} = [\mathbf{Z}]_{n1} \Gamma_h + [\mathbf{Z}]_{n2} \Gamma_H + [\mathbf{Z}]_{n3} \Gamma_A + \dots, \quad (132)$$

where the ellipsis represents contributions from the mixing with the Goldstone boson and the Z boson; see Sec. III. It should be noted that the transformation with \mathbf{Z} is not a unitary transformation; see Ref. [37] for details.

Also the charged Higgs boson appearing as an external particle in a \tilde{t} decay has to obey the proper on-shell conditions. The corrections to the charged Higgs boson propagator lead to an extra Z factor,

$$\hat{Z}_{H^-H^+} = [1 + \text{Re}\hat{\Sigma}'_{H^-H^+}(p^2)|_{p^2=M_{H^\pm}^2}]^{-1}. \quad (133)$$

Expanding both sides of Eq. (133) up to one-loop order and using $\hat{Z}_{H^-H^+} = 1 + \delta\hat{Z}_{H^-H^+}$ leads to

$$\delta\hat{Z}_{H^-H^+} = -\text{Re}\hat{\Sigma}'_{H^-H^+}(p^2)|_{p^2=M_{H^\pm}^2} = -\text{Re}\Sigma'_{H^-H^+}(M_{H^\pm}^2) - \delta Z_{H^-H^+}. \quad (134)$$

Analogous to the procedure for the neutral Higgs bosons, see Ref. [37],

$$\sqrt{\hat{Z}_{H^-H^+}} = 1 + \frac{1}{2} \delta\hat{Z}_{H^-H^+} \quad (135)$$

has to be applied to a process with an external charged Higgs boson. Within the presented calculations, for the charged Higgs bosons, we include contributions from $\sqrt{\hat{Z}_{H^-H^+}}$ strictly at the one-loop level i.e. the correction coming from $\frac{1}{2} \delta\hat{Z}_{H^-H^+}$ of Eq. (134) multiplied by the

corresponding tree-level vertex contribution.¹⁵ As for the neutral Higgs bosons, there are contributions from the mixing with the Goldstone boson and the W boson, which we deal with separately calculating the mixing explicitly and strictly at one-loop order. The Z factor $\hat{Z}_{H^-H^+}$ is UV finite by definition. However, it contains IR divergences that cancel with (IR divergent) soft photon contributions from the one-loop diagrams; see Sec. III.

C. The chargino/neutralino sector of the cMSSM

The chargino/neutralino sector contains two soft SUSY-breaking gaugino mass parameters M_1 and M_2 corresponding to the bino and the wino fields, respectively, as well as the Higgs superfield mixing parameter μ , which, in general, can be complex.¹⁶ The gauge boson masses and $\tan\beta$ that also appear in this sector have already been defined within the context of the Higgs and gauge boson sector; see Sec. II B. For our calculation we also need to renormalize the chargino and neutralino fields.

The starting point for the renormalization procedure of the chargino/neutralino sector is the part of the Fourier transformed MSSM Lagrangian that is bilinear in the chargino and neutralino fields,

$$\begin{aligned} \mathcal{L}_{\tilde{\chi}^{\pm}, \tilde{\chi}^0}^{\text{bil.}} = & \overline{\tilde{\chi}_i^-} \not{p} \omega_- \tilde{\chi}_i^- + \overline{\tilde{\chi}_i^+} \not{p} \omega_+ \tilde{\chi}_i^+ \\ & - \overline{\tilde{\chi}_i^-} [\mathbf{V}^* \mathbf{X}^\top \mathbf{U}^\dagger]_{ij} \omega_- \tilde{\chi}_j^- - \overline{\tilde{\chi}_i^+} [\mathbf{U} \mathbf{X}^* \mathbf{V}^\top]_{ij} \omega_+ \tilde{\chi}_j^+ \\ & + \frac{1}{2} (\overline{\tilde{\chi}_k^0} \not{p} \omega_- \tilde{\chi}_k^0 + \overline{\tilde{\chi}_k^0} \not{p} \omega_+ \tilde{\chi}_k^0 \\ & - \overline{\tilde{\chi}_k^0} [\mathbf{N}^* \mathbf{Y} \mathbf{N}^\dagger]_{kl} \omega_- \tilde{\chi}_l^0 - \overline{\tilde{\chi}_k^0} [\mathbf{N} \mathbf{Y}^* \mathbf{N}^\top]_{kl} \omega_+ \tilde{\chi}_l^0), \end{aligned} \quad (136)$$

already expressed in terms of the chargino and neutralino mass eigenstates $\tilde{\chi}_i^-$ and $\tilde{\chi}_k^0$, respectively, and $i, j = 1, 2$ and $k, l = 1, 2, 3, 4$. The mass eigenstates can be determined

$$\mathbf{Y} = \begin{pmatrix} M_1 & 0 & -M_Z s_w \cos\beta & M_Z s_w \sin\beta \\ 0 & M_2 & M_Z c_w \cos\beta & -M_Z c_w \sin\beta \\ -M_Z s_w \cos\beta & M_Z c_w \cos\beta & 0 & -\mu \\ M_Z s_w \sin\beta & -M_Z c_w \sin\beta & -\mu & 0 \end{pmatrix}. \quad (140)$$

The unitary 4×4 matrix \mathbf{N} and the physical neutralino masses $m_{\tilde{\chi}_k^0}$ ($k = 1, 2, 3, 4$) result from a numerical Takagi factorization [62] of \mathbf{Y} . Starting from the original bino/wino/Higgsino basis, the mass eigenstates can be determined with the help of the transformation matrix \mathbf{N} ,

$$\tilde{\chi}_k^0 = \begin{pmatrix} \psi_k^0 \\ \psi_k^0 \end{pmatrix} \quad \text{with} \quad \psi_k^0 = N_{kl} \begin{pmatrix} \tilde{B}^0 \\ \tilde{W}^0 \\ \tilde{H}_1^0 \\ \tilde{H}_2^0 \end{pmatrix}_l, \quad (141)$$

¹⁵In our calculational setup we add Eq. (134) to (99g).

¹⁶Often, M_2 is chosen to be real, which is possible without loss of generality as not all the possible phases of the MSSM Lagrangian are physical and there is a certain freedom of choice; see the discussion in Sec. IV C.

¹⁷Corresponding to the convention used in FEYNARTS/FORMCALC, we express the chargino part in terms of negative chargino fields, which is in contrast to [50]. As we keep the commonly used definition of the matrix \mathbf{X} the transposed matrix appears in the expression for $\mathbf{M}_{\tilde{\chi}^-}$.

via unitary transformations where the corresponding matrices diagonalize the chargino and neutralino mass matrix, \mathbf{X} and \mathbf{Y} , respectively.

In the chargino case, two 2×2 matrices \mathbf{U} and \mathbf{V} are necessary for the diagonalization of the chargino mass matrix¹⁷ \mathbf{X} ,

$$\mathbf{M}_{\tilde{\chi}^-} = \mathbf{V}^* \mathbf{X}^\top \mathbf{U}^\dagger = \begin{pmatrix} m_{\tilde{\chi}_1^\pm} & 0 \\ 0 & m_{\tilde{\chi}_2^\pm} \end{pmatrix} \quad \text{with} \quad \mathbf{X} = \begin{pmatrix} M_2 & \sqrt{2} \sin\beta M_W \\ \sqrt{2} \cos\beta M_W & \mu \end{pmatrix}, \quad (137)$$

where $\mathbf{M}_{\tilde{\chi}^-}$ is the diagonal mass matrix with the chargino masses $m_{\tilde{\chi}_1^\pm}$, $m_{\tilde{\chi}_2^\pm}$ as entries, which are determined as the (real and positive) singular values of \mathbf{X} . The singular value decomposition of \mathbf{X} also yields results for \mathbf{U} and \mathbf{V} . Using the transformation matrices \mathbf{U} and \mathbf{V} , the interaction Higgsino and Wino spinors \tilde{H}_1^- , \tilde{H}_2^+ , and \tilde{W}^\pm , which are two component Weyl spinors, can be transformed into the mass eigenstates

$$\tilde{\chi}_i^- = \begin{pmatrix} \psi_i^L \\ \psi_i^R \end{pmatrix} \quad \text{with} \quad \psi_i^L = U_{ij} \begin{pmatrix} \tilde{W}^- \\ \tilde{H}_1^- \end{pmatrix}_j \quad \text{and} \quad \psi_i^R = V_{ij} \begin{pmatrix} \tilde{W}^+ \\ \tilde{H}_2^+ \end{pmatrix}_j, \quad (138)$$

where the i th mass eigenstate can be expressed in terms of either the Weyl spinors ψ_i^L and ψ_i^R or the Dirac spinor $\tilde{\chi}_i^-$.

In the neutralino case, as the neutralino mass matrix \mathbf{Y} is symmetric, one 4×4 matrix is sufficient for the diagonalization

$$\mathbf{M}_{\tilde{\chi}^0} = \mathbf{N}^* \mathbf{Y} \mathbf{N}^\dagger = \text{diag}(m_{\tilde{\chi}_1^0}, m_{\tilde{\chi}_2^0}, m_{\tilde{\chi}_3^0}, m_{\tilde{\chi}_4^0}) \quad (139)$$

with

where ψ_k^0 denotes the two-component Weyl spinor and $\tilde{\chi}_k^0$ the four-component Majorana spinor of the k th neutralino field.

Concerning the renormalization we follow the prescription of Ref. [50]. The following replacements of the parameters and the fields are performed according to the multiplicative renormalization procedure:

$$M_1 \rightarrow M_1 + \delta M_1, \quad (142)$$

$$M_2 \rightarrow M_2 + \delta M_2, \quad (143)$$

$$\mu \rightarrow \mu + \delta \mu, \quad (144)$$

$$\omega_- \tilde{\chi}_i^- \rightarrow \left[\mathbb{1} + \frac{1}{2} \delta \mathbf{Z}_{\tilde{\chi}^-}^L \right]_{ij} \omega_- \tilde{\chi}_j^- \quad (i, j = 1, 2), \quad (145)$$

$$\omega_+ \tilde{\chi}_i^- \rightarrow \left[\mathbb{1} + \frac{1}{2} \delta \mathbf{Z}_{\tilde{\chi}^-}^R \right]_{ij} \omega_+ \tilde{\chi}_j^- \quad (i, j = 1, 2), \quad (146)$$

$$\delta \mathbf{Y} = \begin{pmatrix} \delta M_1 & 0 & -\delta(M_Z s_w \cos \beta) & \delta(M_Z s_w \sin \beta) \\ 0 & \delta M_2 & \delta(M_Z c_w \cos \beta) & -\delta(M_Z c_w \sin \beta) \\ -\delta(M_Z s_w \cos \beta) & \delta(M_Z c_w \cos \beta) & 0 & -\delta \mu \\ \delta(M_Z s_w \sin \beta) & -\delta(M_Z c_w \sin \beta) & -\delta \mu & 0 \end{pmatrix}, \quad (152)$$

the replacements of the matrices $\mathbf{M}_{\tilde{\chi}^-}$ and $\mathbf{M}_{\tilde{\chi}^0}$ can be expressed as

$$\mathbf{M}_{\tilde{\chi}^-} \rightarrow \mathbf{M}_{\tilde{\chi}^-} + \delta \mathbf{M}_{\tilde{\chi}^-} = \mathbf{M}_{\tilde{\chi}^-} + \mathbf{V}^* \delta \mathbf{X}^\top \mathbf{U}^\dagger, \quad (153)$$

$$\mathbf{M}_{\tilde{\chi}^0} \rightarrow \mathbf{M}_{\tilde{\chi}^0} + \delta \mathbf{M}_{\tilde{\chi}^0} = \mathbf{M}_{\tilde{\chi}^0} + \mathbf{N}^* \delta \mathbf{Y} \mathbf{N}^\dagger. \quad (154)$$

Now the renormalized self-energies are given by

$$[\hat{\Sigma}_{\tilde{\chi}^-}^L(p^2)]_{ij} = [\Sigma_{\tilde{\chi}^-}^L(p^2)]_{ij} + \frac{1}{2} [\delta \mathbf{Z}_{\tilde{\chi}^-}^L + \delta \mathbf{Z}_{\tilde{\chi}^-}^{L\dagger}]_{ij}, \quad (155)$$

$$[\hat{\Sigma}_{\tilde{\chi}^-}^R(p^2)]_{ij} = [\Sigma_{\tilde{\chi}^-}^R(p^2)]_{ij} + \frac{1}{2} [\delta \mathbf{Z}_{\tilde{\chi}^-}^R + \delta \mathbf{Z}_{\tilde{\chi}^-}^{R\dagger}]_{ij}, \quad (156)$$

$$\begin{aligned} [\hat{\Sigma}_{\tilde{\chi}^-}^{SL}(p^2)]_{ij} &= [\Sigma_{\tilde{\chi}^-}^{SL}(p^2)]_{ij} \\ &\quad - \left[\frac{1}{2} \delta \mathbf{Z}_{\tilde{\chi}^-}^{R\dagger} \mathbf{M}_{\tilde{\chi}^-} + \frac{1}{2} \mathbf{M}_{\tilde{\chi}^-} \delta \mathbf{Z}_{\tilde{\chi}^-}^L + \delta \mathbf{M}_{\tilde{\chi}^-} \right]_{ij}, \end{aligned} \quad (157)$$

$$\begin{aligned} [\hat{\Sigma}_{\tilde{\chi}^-}^{SR}(p^2)]_{ij} &= [\Sigma_{\tilde{\chi}^-}^{SR}(p^2)]_{ij} \\ &\quad - \left[\frac{1}{2} \delta \mathbf{Z}_{\tilde{\chi}^-}^{L\dagger} \mathbf{M}_{\tilde{\chi}^-}^\dagger + \frac{1}{2} \mathbf{M}_{\tilde{\chi}^-}^\dagger \delta \mathbf{Z}_{\tilde{\chi}^-}^R + \delta \mathbf{M}_{\tilde{\chi}^-}^\dagger \right]_{ij}, \end{aligned} \quad (158)$$

$$\omega_- \tilde{\chi}_k^0 \rightarrow \left[\mathbb{1} + \frac{1}{2} \delta \mathbf{Z}_{\tilde{\chi}^0} \right]_{kl} \omega_- \tilde{\chi}_l^0 \quad (k, l = 1, 2, 3, 4), \quad (147)$$

$$\omega_+ \tilde{\chi}_k^0 \rightarrow \left[\mathbb{1} + \frac{1}{2} \delta \mathbf{Z}_{\tilde{\chi}^0}^* \right]_{kl} \omega_+ \tilde{\chi}_l^0 \quad (k, l = 1, 2, 3, 4). \quad (148)$$

It should be noted that the parameter counterterms are complex counterterms that each need two renormalization conditions to be fixed. The transformation matrices are not renormalized, so that, using the notation of replacing a matrix by its renormalized matrix and a counterterm matrix

$$\mathbf{X} \rightarrow \mathbf{X} + \delta \mathbf{X}, \quad (149)$$

$$\mathbf{Y} \rightarrow \mathbf{Y} + \delta \mathbf{Y} \quad (150)$$

with

$$\delta \mathbf{X} = \begin{pmatrix} \delta M_2 & \sqrt{2} \delta(M_W \sin \beta) \\ \sqrt{2} \delta(M_W \cos \beta) & \delta \mu \end{pmatrix}, \quad (151)$$

$$[\hat{\Sigma}_{\tilde{\chi}^0}^L(p^2)]_{kl} = [\Sigma_{\tilde{\chi}^0}^L(p^2)]_{kl} + \frac{1}{2} [\delta \mathbf{Z}_{\tilde{\chi}^0} + \delta \mathbf{Z}_{\tilde{\chi}^0}^\dagger]_{kl}, \quad (159)$$

$$[\hat{\Sigma}_{\tilde{\chi}^0}^R(p^2)]_{kl} = [\Sigma_{\tilde{\chi}^0}^R(p^2)]_{kl} + \frac{1}{2} [\delta \mathbf{Z}_{\tilde{\chi}^0}^* + \delta \mathbf{Z}_{\tilde{\chi}^0}^\top]_{kl}, \quad (160)$$

$$\begin{aligned} [\hat{\Sigma}_{\tilde{\chi}^0}^{SL}(p^2)]_{kl} &= [\Sigma_{\tilde{\chi}^0}^{SL}(p^2)]_{kl} \\ &\quad - \left[\frac{1}{2} \delta \mathbf{Z}_{\tilde{\chi}^0}^\top \mathbf{M}_{\tilde{\chi}^0} + \frac{1}{2} \mathbf{M}_{\tilde{\chi}^0} \delta \mathbf{Z}_{\tilde{\chi}^0} + \delta \mathbf{M}_{\tilde{\chi}^0} \right]_{kl}, \end{aligned} \quad (161)$$

$$\begin{aligned} [\hat{\Sigma}_{\tilde{\chi}^0}^{SR}(p^2)]_{kl} &= [\Sigma_{\tilde{\chi}^0}^{SR}(p^2)]_{kl} \\ &\quad - \left[\frac{1}{2} \delta \mathbf{Z}_{\tilde{\chi}^0}^\dagger \mathbf{M}_{\tilde{\chi}^0}^\dagger + \frac{1}{2} \mathbf{M}_{\tilde{\chi}^0}^\dagger \delta \mathbf{Z}_{\tilde{\chi}^0}^* + \delta \mathbf{M}_{\tilde{\chi}^0}^\dagger \right]_{kl}. \end{aligned} \quad (162)$$

Instead of choosing the three complex parameters M_1 , M_2 , and μ as independent parameters, we impose on-shell conditions for the two chargino masses and the mass of the lightest neutralino and extract the expressions for the counterterms of M_1 , M_2 , and μ , accordingly. In a recent analysis [63] it was emphasized that in the case of the renormalization of two chargino and one neutralino mass, always the most binolike neutralino has to be renormalized

in order to find a numerically stable result. Also, in Ref. [64] the problem of large unphysical contributions due to a non-binolike lightest neutralino is discussed. In our numerical setup, see Sec. IV, the lightest neutralino is always rather binolike. On the other hand, it would be trivial to change our prescription from the lightest neutralino to any other neutralino. In Ref. [63] it was also suggested that the numerically most stable result is obtained via the renormalization of one chargino and two neutralinos. However, in our approach, this choice leads to IR divergences, since the chargino mass changes (from the tree-level mass to the one-loop pole mass) by a finite shift due to the renormalization procedure. Using the shifted mass for the external particle but the tree-level mass for internal particles results in IR divergences. On the other hand, in general, inserting the shifted chargino mass everywhere yields UV divergences. Consequently, we stick to our choice of imposing on-shell conditions for the two charginos and one neutralino. The conditions read

$$([\widetilde{\text{Re}}\hat{\Sigma}_{\tilde{\chi}^-}(p)]_{ii}\tilde{\chi}_i^-(p))|_{p^2=m_{\tilde{\chi}_i^\pm}^2} = 0 \quad (i = 1, 2), \quad (163)$$

$$([\widetilde{\text{Re}}\hat{\Sigma}_{\tilde{\chi}^0}(p)]_{11}\tilde{\chi}_1^0(p))|_{p^2=m_{\tilde{\chi}_1^0}^2} = 0. \quad (164)$$

These conditions can be rewritten in terms of six equations defining six real parameters and field renormalization constants or three complex ones,

$$\begin{aligned} \widetilde{\text{Re}}[m_{\tilde{\chi}_i^\pm}(\hat{\Sigma}_{\tilde{\chi}^-}^L(m_{\tilde{\chi}_i^\pm}^2) + \hat{\Sigma}_{\tilde{\chi}^-}^R(m_{\tilde{\chi}_i^\pm}^2)) + \hat{\Sigma}_{\tilde{\chi}^-}^{SL}(m_{\tilde{\chi}_i^\pm}^2) \\ + \hat{\Sigma}_{\tilde{\chi}^-}^{SR}(m_{\tilde{\chi}_i^\pm}^2)]_{ii} = 0, \end{aligned} \quad (165)$$

$$\begin{aligned} \widetilde{\text{Re}}[m_{\tilde{\chi}_i^\pm}(\hat{\Sigma}_{\tilde{\chi}^-}^L(m_{\tilde{\chi}_i^\pm}^2) - \hat{\Sigma}_{\tilde{\chi}^-}^R(m_{\tilde{\chi}_i^\pm}^2)) - \hat{\Sigma}_{\tilde{\chi}^-}^{SL}(m_{\tilde{\chi}_i^\pm}^2) \\ + \hat{\Sigma}_{\tilde{\chi}^-}^{SR}(m_{\tilde{\chi}_i^\pm}^2)]_{ii} = 0, \end{aligned} \quad (166)$$

$$\begin{aligned} \widetilde{\text{Re}}[m_{\tilde{\chi}_1^0}(\hat{\Sigma}_{\tilde{\chi}^0}^L(m_{\tilde{\chi}_1^0}^2) + \hat{\Sigma}_{\tilde{\chi}^0}^R(m_{\tilde{\chi}_1^0}^2)) + \hat{\Sigma}_{\tilde{\chi}^0}^{SL}(m_{\tilde{\chi}_1^0}^2) \\ + \hat{\Sigma}_{\tilde{\chi}^0}^{SR}(m_{\tilde{\chi}_1^0}^2)]_{11} = 0, \end{aligned} \quad (167)$$

$$\begin{aligned} \widetilde{\text{Re}}[m_{\tilde{\chi}_1^0}(\hat{\Sigma}_{\tilde{\chi}^0}^L(m_{\tilde{\chi}_1^0}^2) - \hat{\Sigma}_{\tilde{\chi}^0}^R(m_{\tilde{\chi}_1^0}^2)) - \hat{\Sigma}_{\tilde{\chi}^0}^{SL}(m_{\tilde{\chi}_1^0}^2) \\ + \hat{\Sigma}_{\tilde{\chi}^0}^{SR}(m_{\tilde{\chi}_1^0}^2)]_{11} = 0. \end{aligned} \quad (168)$$

For the further determination of the field renormalization constants we also impose

$$\begin{aligned} \lim_{p^2 \rightarrow m_{\tilde{\chi}_i^\pm}^2} \left(\frac{(\not{p} + m_{\tilde{\chi}_i^\pm})[\widetilde{\text{Re}}\hat{\Sigma}_{\tilde{\chi}^-}(p)]_{ii}}{p^2 - m_{\tilde{\chi}_i^\pm}^2} \tilde{\chi}_i^-(p) \right) = 0 \\ (i = 1, 2), \end{aligned} \quad (169)$$

$$\lim_{p^2 \rightarrow m_{\tilde{\chi}_1^0}^2} \left(\frac{(\not{p} + m_{\tilde{\chi}_1^0})[\widetilde{\text{Re}}\hat{\Sigma}_{\tilde{\chi}^0}(p)]_{11}}{p^2 - m_{\tilde{\chi}_1^0}^2} \tilde{\chi}_1^0(p) \right) = 0. \quad (170)$$

This leads to the following set of equations:

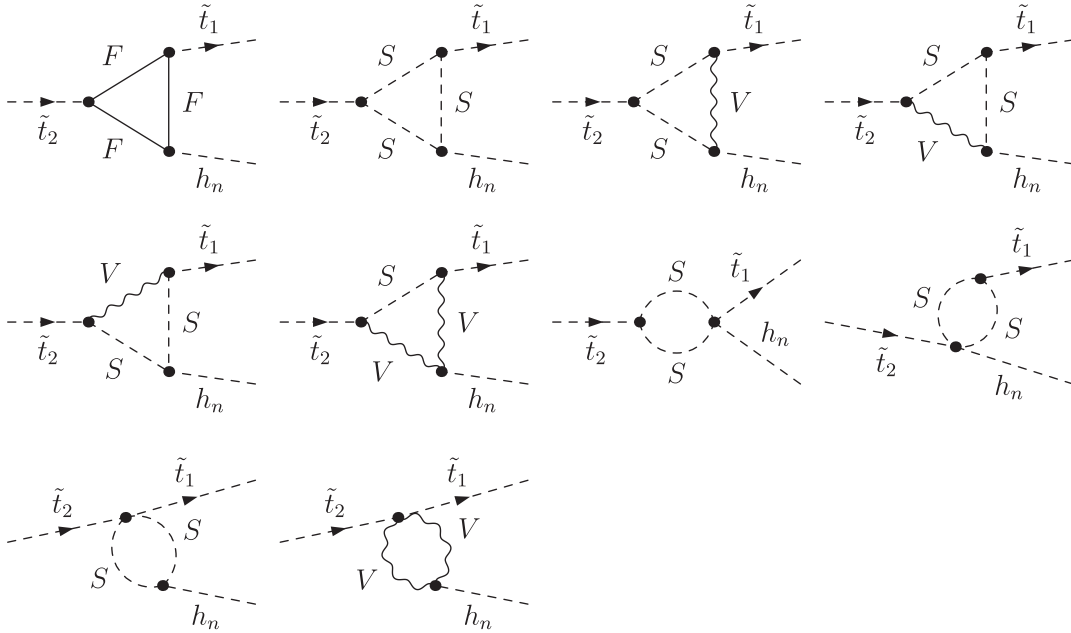


FIG. 1. Generic Feynman diagrams for the decay $\tilde{t}_2 \rightarrow \tilde{t}_1 h_n$ ($n = 1, 2, 3$). F can be a SM fermion, chargino, neutralino, or gluino; S can be a sfermion or a Higgs boson; V can be a γ , Z , W^\pm , or g . Not shown are the diagrams with a $Z - h_n$ or $G - h_n$ transition contribution on the external Higgs boson leg.

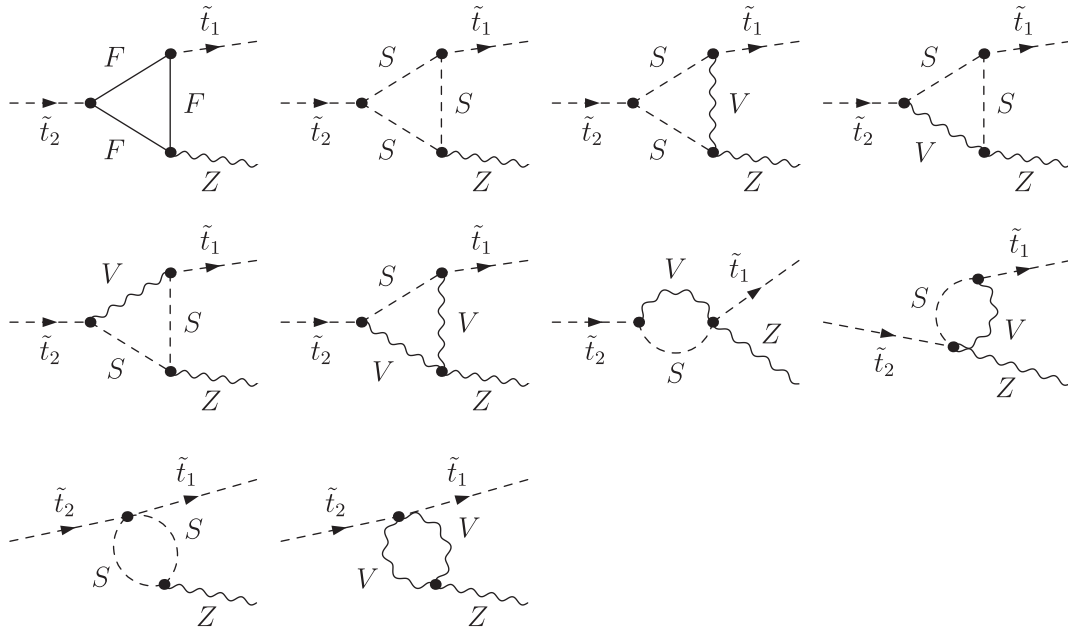


FIG. 2. Generic Feynman diagrams for the decay $\tilde{t}_2 \rightarrow \tilde{t}_1 Z$. F can be a SM fermion, chargino, neutralino, or gluino; S can be a sfermion or a Higgs boson; V can be a γ , Z , W^\pm , or g .

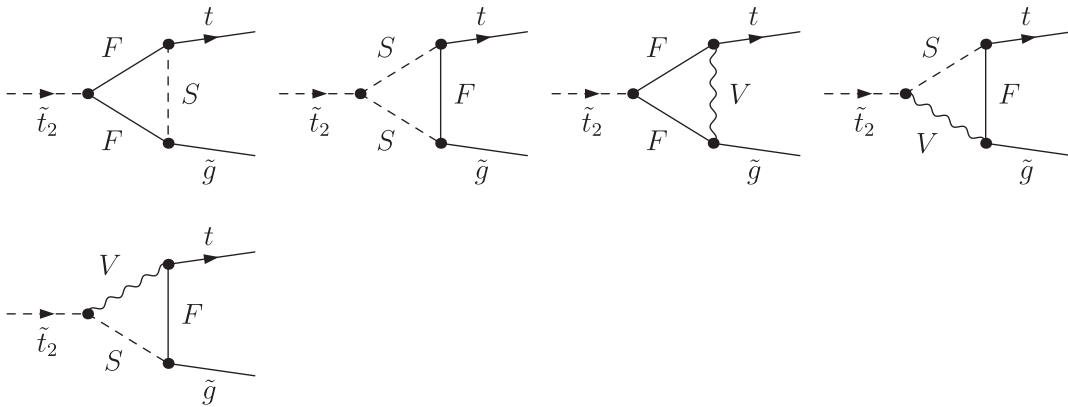


FIG. 3. Generic Feynman diagrams for the decay $\tilde{t}_2 \rightarrow t \tilde{g}$. F can be a SM fermion, chargino, neutralino, or gluino; S can be a sfermion or a Higgs boson; V can be a γ , Z , W^\pm , or g .

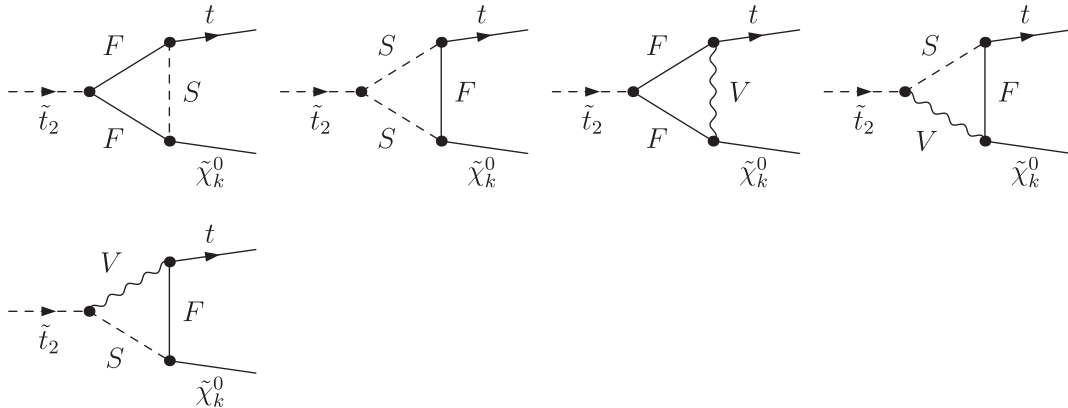


FIG. 4. Generic Feynman diagrams for the decay $\tilde{t}_2 \rightarrow t \tilde{\chi}_k^0$ ($k = 1, 2, 3, 4$). F can be a SM fermion, chargino, neutralino, or gluino; S can be a sfermion or a Higgs boson; V can be a γ , Z , W^\pm , or g .

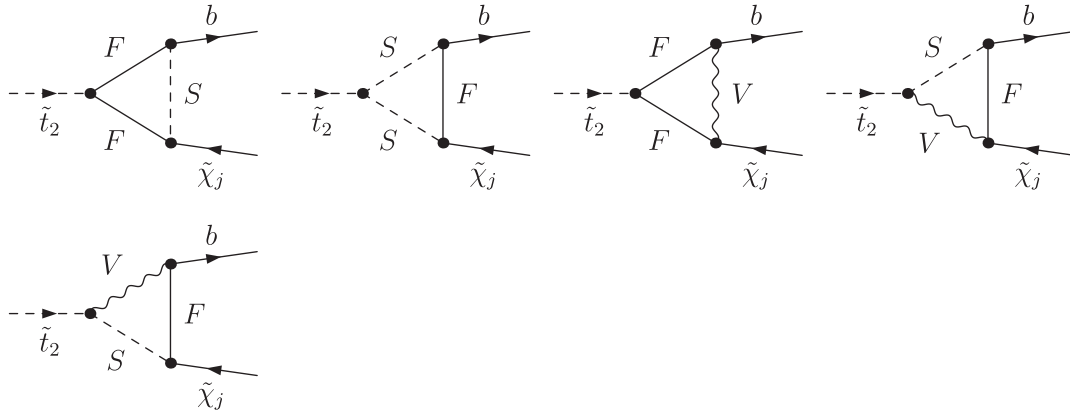


FIG. 5. Generic Feynman diagrams for the decay $\tilde{t}_2 \rightarrow b \tilde{\chi}_j^+$ ($j = 1, 2$). F can be a SM fermion, chargino, neutralino, or gluino; S can be a sfermion or a Higgs boson; V can be a γ, Z, W^\pm , or g .

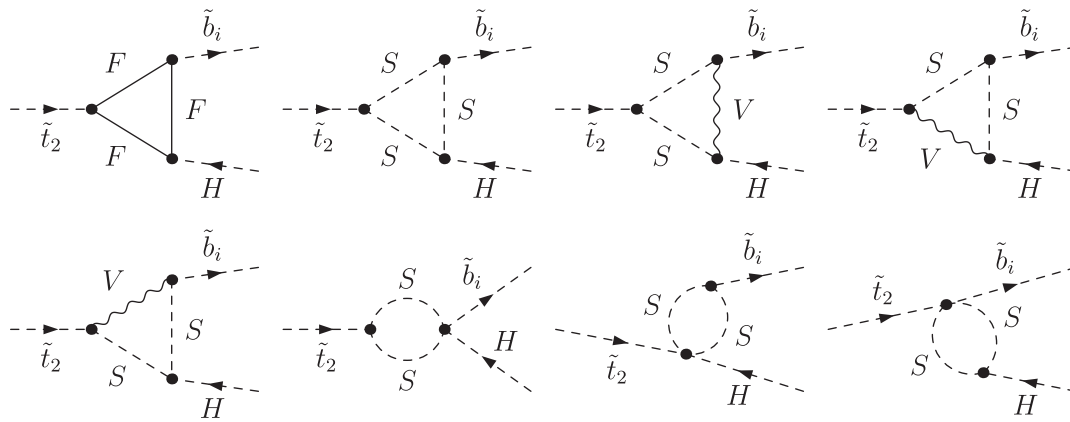


FIG. 6. Generic Feynman diagrams for the decay $\tilde{t}_2 \rightarrow \tilde{b}_i H^+$ ($i = 1, 2$). F can be a SM fermion, chargino, neutralino, or gluino; S can be a sfermion or a Higgs boson; V can be a γ, Z, W^\pm , or g . Not shown are the diagrams with a $W^+ - H^+$ or $G^+ - H^+$ transition contribution on the external Higgs boson leg.

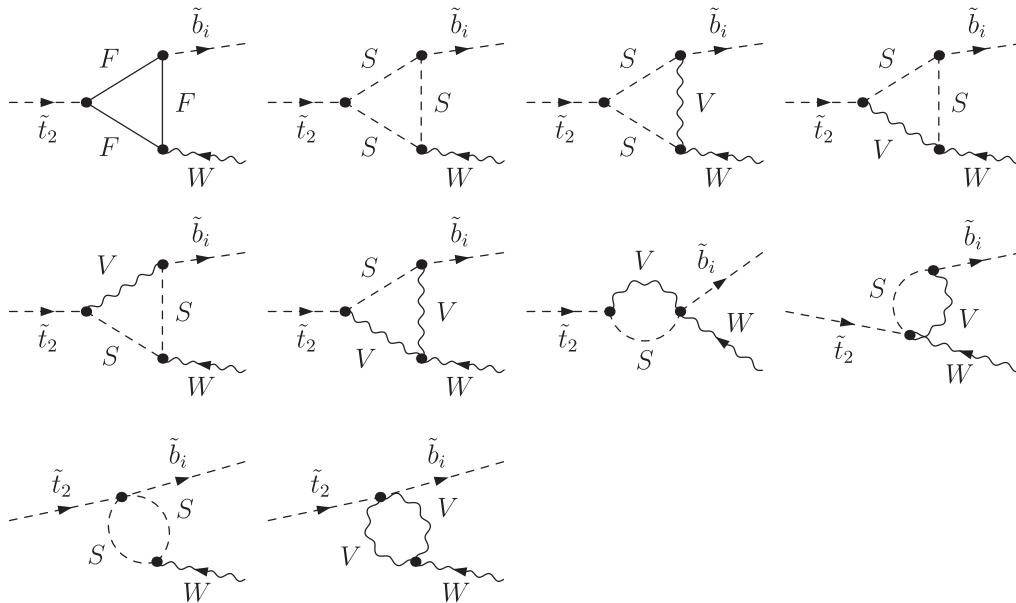


FIG. 7. Generic Feynman diagrams for the decay $\tilde{t}_2 \rightarrow \tilde{b}_i W^+$ ($i = 1, 2$). F can be a SM fermion, chargino, neutralino, or gluino; S can be a sfermion or a Higgs boson; V can be a γ, Z, W^\pm , or g .

TABLE I. MSSM parameters for the initial numerical investigation; all parameters (except $\tan\beta$) are in GeV. We always set $m_b^{\overline{\text{MS}}}(m_b) = 4.2$ GeV. In our analysis $M_{\tilde{q}_L} (= M_{\tilde{l}_L})$, $M_{\tilde{t}_R} (= M_{\tilde{u}_R} = M_{\tilde{c}_R})$, and $M_{\tilde{b}_R} (= M_{\tilde{d}_R} = M_{\tilde{s}_R} = M_{\tilde{t}_R})$ are chosen such that the values of $m_{\tilde{t}_1}$, $m_{\tilde{t}_2}$, and $m_{\tilde{b}_2}$ are realized. For the \tilde{b} sector the shifts in $M_{\tilde{q}_{L,R}}(\tilde{b})$ as defined in Eqs. (48) and (50) are taken into account. The values for A_t and $A_b (= A_\tau)$ are chosen such that charge- or color-breaking minima are avoided [77].

| Scen. | $\tan\beta$ | M_{H^\pm} | $m_{\tilde{t}_2}$ | $m_{\tilde{t}_1}$ | $m_{\tilde{b}_2}$ | μ | A_t | A_b | M_1 | M_2 | M_3 |
|-------|-------------|-------------|-------------------|----------------------|----------------------|-------|-------|-------|-------|-------|-------|
| S1 | 20 | 150 | 650 | $0.4m_{\tilde{t}_2}$ | $0.7m_{\tilde{t}_2}$ | 200 | 800 | 400 | 200 | 300 | 350 |
| S2 | 20 | 180 | 1200 | $0.6m_{\tilde{t}_2}$ | $0.8m_{\tilde{t}_2}$ | 300 | 1800 | 1600 | 150 | 200 | 400 |

TABLE II. The stop and sbottom masses in S1 and S2 and at different $\tan\beta$ for the numerical investigation; all masses are in GeV and rounded to 1 MeV.

| Scen. | $\tan\beta$ | $m_{\tilde{t}_1}$ | $m_{\tilde{t}_2}$ | $m_{\tilde{b}_1}$ | $m_{\tilde{b}_2}$ |
|-------|-------------|-------------------|-------------------|-------------------|-------------------|
| S1 | 2 | 260.000 | 650.000 | 305.436 | 455.000 |
| | 20 | 260.000 | 650.000 | 333.572 | 455.000 |
| | 50 | 260.000 | 650.000 | 329.755 | 455.000 |
| S2 | 2 | 720.000 | 1200.000 | 769.801 | 960.000 |
| | 20 | 720.000 | 1200.000 | 783.300 | 960.000 |
| | 50 | 720.000 | 1200.000 | 783.094 | 960.000 |

$$\begin{aligned} \widetilde{\text{Re}}\left[\frac{1}{2}(\hat{\Sigma}_{\tilde{\chi}^-}^L(m_{\tilde{\chi}_i^\pm}^2) + \hat{\Sigma}_{\tilde{\chi}^-}^R(m_{\tilde{\chi}_i^\pm}^2)) + m_{\tilde{\chi}_i^\pm}^2(\hat{\Sigma}_{\tilde{\chi}^-}^{L'}(m_{\tilde{\chi}_i^\pm}^2) \right. \\ \left. + \hat{\Sigma}_{\tilde{\chi}^-}^{R'}(m_{\tilde{\chi}_i^\pm}^2)) + m_{\tilde{\chi}_i^\pm}(\hat{\Sigma}_{\tilde{\chi}^-}^{SL'}(m_{\tilde{\chi}_i^\pm}^2) + \hat{\Sigma}_{\tilde{\chi}^-}^{SR'}(m_{\tilde{\chi}_i^\pm}^2))\right]_{ii} = 0, \end{aligned} \quad (171)$$

$$\widetilde{\text{Re}}[\hat{\Sigma}_{\tilde{\chi}^-}^L(m_{\tilde{\chi}_i^\pm}^2) - \hat{\Sigma}_{\tilde{\chi}^-}^R(m_{\tilde{\chi}_i^\pm}^2)]_{ii} = 0, \quad (172)$$

$$\begin{aligned} \widetilde{\text{Re}}\left[\frac{1}{2}(\hat{\Sigma}_{\tilde{\chi}^0}^L(m_{\tilde{\chi}_1^0}^2) + \hat{\Sigma}_{\tilde{\chi}^0}^R(m_{\tilde{\chi}_1^0}^2)) + m_{\tilde{\chi}_1^0}^2(\hat{\Sigma}_{\tilde{\chi}^0}^{L'}(m_{\tilde{\chi}_1^0}^2) \right. \\ \left. + \hat{\Sigma}_{\tilde{\chi}^0}^{R'}(m_{\tilde{\chi}_1^0}^2)) + m_{\tilde{\chi}_1^0}(\hat{\Sigma}_{\tilde{\chi}^0}^{SL'}(m_{\tilde{\chi}_1^0}^2) + \hat{\Sigma}_{\tilde{\chi}^0}^{SR'}(m_{\tilde{\chi}_1^0}^2))\right]_{11} = 0, \end{aligned} \quad (173)$$

$$\widetilde{\text{Re}}[\hat{\Sigma}_{\tilde{\chi}^0}^L(m_{\tilde{\chi}_1^0}^2) - \hat{\Sigma}_{\tilde{\chi}^0}^R(m_{\tilde{\chi}_1^0}^2)]_{11} = 0, \quad (174)$$

where we have used again the shorthand $\Sigma'(m^2) \equiv \frac{\partial \Sigma}{\partial p^2}|_{p^2=m^2}$. It should be noted that Eq. (174) is already fulfilled due to the Majorana nature of the neutralinos. Inserting Eqs. (155)–(162) for the renormalized self-energies in Eqs. (165)–(168) and solving for $[\delta\mathbf{M}_{\tilde{\chi}^-}]_{ii}$ and $[\delta\mathbf{M}_{\tilde{\chi}^0}]_{11}$ results in

$$\begin{aligned} \text{Re}[\delta\mathbf{M}_{\tilde{\chi}^-}]_{ii} = \frac{1}{2} \widetilde{\text{Re}}[m_{\tilde{\chi}_i^\pm}(\Sigma_{\tilde{\chi}^-}^L(m_{\tilde{\chi}_i^\pm}^2) + \Sigma_{\tilde{\chi}^-}^R(m_{\tilde{\chi}_i^\pm}^2)) \\ + \Sigma_{\tilde{\chi}^-}^{SL}(m_{\tilde{\chi}_i^\pm}^2) + \Sigma_{\tilde{\chi}^-}^{SR}(m_{\tilde{\chi}_i^\pm}^2)]_{ii}, \end{aligned} \quad (175)$$

$$\begin{aligned} \text{Im}[\delta\mathbf{M}_{\tilde{\chi}^-}]_{ii} = \frac{i}{2} \widetilde{\text{Re}}[\Sigma_{\tilde{\chi}^-}^{SR}(m_{\tilde{\chi}_i^\pm}^2) - \Sigma_{\tilde{\chi}^-}^{SL}(m_{\tilde{\chi}_i^\pm}^2)]_{ii} \\ - \frac{1}{2} m_{\tilde{\chi}_i^\pm} \text{Im}[\delta\mathbf{Z}_{\tilde{\chi}^-}^L - \delta\mathbf{Z}_{\tilde{\chi}^-}^R]_{ii}, \end{aligned} \quad (176)$$

$$\begin{aligned} \text{Re}[\delta\mathbf{M}_{\tilde{\chi}^0}]_{11} = \frac{1}{2} \widetilde{\text{Re}}[m_{\tilde{\chi}_1^0}(\Sigma_{\tilde{\chi}^0}^L(m_{\tilde{\chi}_1^0}^2) + \Sigma_{\tilde{\chi}^0}^R(m_{\tilde{\chi}_1^0}^2)) \\ + \Sigma_{\tilde{\chi}^0}^{SL}(m_{\tilde{\chi}_1^0}^2) + \Sigma_{\tilde{\chi}^0}^{SR}(m_{\tilde{\chi}_1^0}^2)]_{11}, \end{aligned} \quad (177)$$

$$\begin{aligned} \text{Im}[\delta\mathbf{M}_{\tilde{\chi}^0}]_{11} = \frac{i}{2} \widetilde{\text{Re}}[\Sigma_{\tilde{\chi}^0}^{SR}(m_{\tilde{\chi}_1^0}^2) - \Sigma_{\tilde{\chi}^0}^{SL}(m_{\tilde{\chi}_1^0}^2)]_{11} \\ - m_{\tilde{\chi}_1^0} \text{Im}[\delta\mathbf{Z}_{\tilde{\chi}^0}]_{11}, \end{aligned} \quad (178)$$

where we have used already Eqs. (172) and (174). Using Eqs. (151)–(154), these conditions lead to [50,65]

$$\begin{aligned} \delta M_1 = \frac{1}{(N_{11}^*)^2} (2N_{11}^* [N_{13}^* \delta(M_{Zs_w} \cos\beta) - N_{14}^* \delta(M_{Zs_w} \sin\beta)] - N_{12}^* [2N_{13}^* \delta(M_{Zc_w} \cos\beta) - 2N_{14}^* \delta(M_{Zc_w} \sin\beta) \\ + N_{12}^* \delta M_2] + 2N_{13}^* N_{14}^* \delta\mu + [m_{\tilde{\chi}_1^0} (\widetilde{\text{Re}}\Sigma_{\tilde{\chi}^0}^L(m_{\tilde{\chi}_1^0}^2) - i \text{Im}\delta\mathbf{Z}_{\tilde{\chi}^0}) + \widetilde{\text{Re}}\Sigma_{\tilde{\chi}^0}^{SL}(m_{\tilde{\chi}_1^0}^2)]_{11}), \end{aligned} \quad (179)$$

$$\begin{aligned} \delta M_2 = \frac{1}{2(U_{11}^* U_{22}^* V_{11}^* V_{22}^* - U_{12}^* U_{21}^* V_{12}^* V_{21}^*)} (U_{22}^* V_{22}^* [m_{\tilde{\chi}_1^\pm} (\widetilde{\text{Re}}\Sigma_{\tilde{\chi}^-}^L(m_{\tilde{\chi}_1^\pm}^2) + \widetilde{\text{Re}}\Sigma_{\tilde{\chi}^-}^R(m_{\tilde{\chi}_1^\pm}^2) - i \text{Im}\{\delta\mathbf{Z}_{\tilde{\chi}^-}^L - \delta\mathbf{Z}_{\tilde{\chi}^-}^R\}) \\ + 2 \widetilde{\text{Re}}\Sigma_{\tilde{\chi}^-}^{SL}(m_{\tilde{\chi}_1^\pm}^2)]_{11} - U_{12}^* V_{12}^* [m_{\tilde{\chi}_2^\pm} (\widetilde{\text{Re}}\Sigma_{\tilde{\chi}^-}^L(m_{\tilde{\chi}_2^\pm}^2) + \widetilde{\text{Re}}\Sigma_{\tilde{\chi}^-}^R(m_{\tilde{\chi}_2^\pm}^2) - i \text{Im}\{\delta\mathbf{Z}_{\tilde{\chi}^-}^L - \delta\mathbf{Z}_{\tilde{\chi}^-}^R\}) + 2 \widetilde{\text{Re}}\Sigma_{\tilde{\chi}^-}^{SL}(m_{\tilde{\chi}_2^\pm}^2)]_{22} \\ + 2(U_{12}^* U_{21}^* - U_{11}^* U_{22}^*) V_{12}^* V_{22}^* \delta(\sqrt{2}M_W \sin\beta) + 2U_{12}^* U_{22}^* (V_{12}^* V_{21}^* - V_{11}^* V_{22}^*) \delta(\sqrt{2}M_W \cos\beta)), \end{aligned} \quad (180)$$

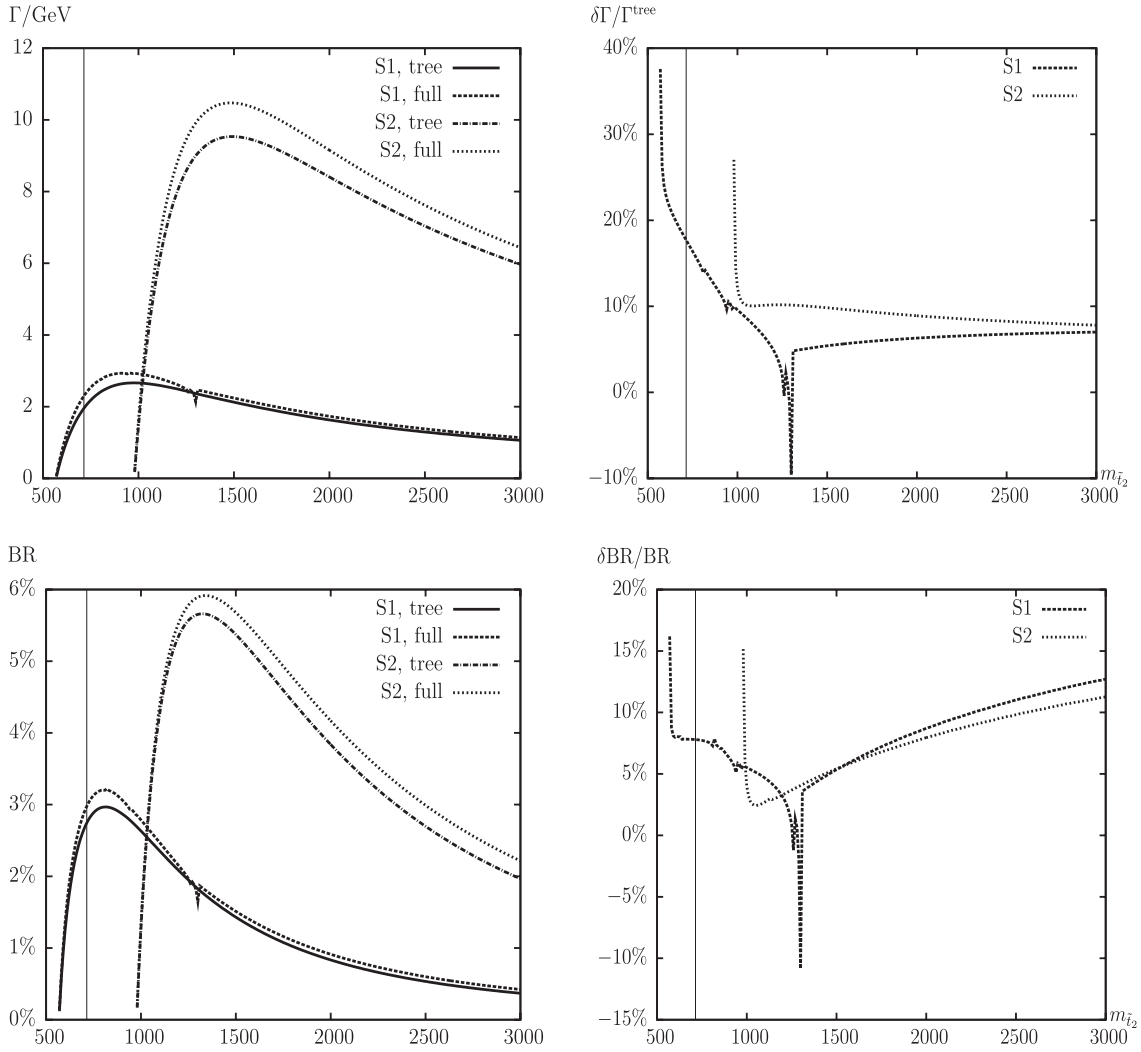


FIG. 8. $\Gamma(\tilde{t}_2 \rightarrow \tilde{t}_1 h_1)$. Tree-level and full one-loop corrected partial decay widths are shown with the parameters chosen according to S1 and S2 (see Table I), with $m_{\tilde{t}_2}$ varied. The upper left plot shows the partial decay width; the upper right plot shows the corresponding relative size of the corrections. The lower left plot shows the BR; the lower right plot shows the relative correction of the BR. The vertical lines indicate where $m_{\tilde{t}_2} + m_{\tilde{t}_1} = 1000$ GeV, i.e. the maximum reach of the ILC(1000).

$$\begin{aligned}
\delta\mu = & \frac{1}{2(U_{11}^* U_{22}^* V_{11}^* V_{22}^* - U_{12}^* U_{21}^* V_{12}^* V_{21}^*)} (U_{11}^* V_{11}^* [m_{\tilde{\chi}_2^\pm} (\tilde{\text{Re}}\Sigma_{\tilde{\chi}^-}^L(m_{\tilde{\chi}_2^\pm}^2) + \tilde{\text{Re}}\Sigma_{\tilde{\chi}^-}^R(m_{\tilde{\chi}_2^\pm}^2) - i \text{Im}\{\delta\mathbf{Z}_{\tilde{\chi}^-}^L - \delta\mathbf{Z}_{\tilde{\chi}^-}^R\}) \\
& + 2 \tilde{\text{Re}}\Sigma_{\tilde{\chi}^-}^{SL}(m_{\tilde{\chi}_2^\pm}^2)]_{22} - U_{21}^* V_{21}^* [m_{\tilde{\chi}_1^\pm} (\tilde{\text{Re}}\Sigma_{\tilde{\chi}^-}^L(m_{\tilde{\chi}_1^\pm}^2) + \tilde{\text{Re}}\Sigma_{\tilde{\chi}^-}^R(m_{\tilde{\chi}_1^\pm}^2) - i \text{Im}\{\delta\mathbf{Z}_{\tilde{\chi}^-}^L - \delta\mathbf{Z}_{\tilde{\chi}^-}^R\}) + 2 \tilde{\text{Re}}\Sigma_{\tilde{\chi}^-}^{SL}(m_{\tilde{\chi}_1^\pm}^2)]_{11} \\
& + 2(U_{12}^* U_{21}^* - U_{11}^* U_{22}^*) V_{11}^* V_{21}^* \delta(\sqrt{2}M_W \cos\beta) + 2U_{11}^* U_{21}^* (V_{12}^* V_{21}^* - V_{11}^* V_{22}^*) \delta(\sqrt{2}M_W \sin\beta)). \quad (181)
\end{aligned}$$

Equations (171)–(173) define the real part of the diagonal field renormalization constants of the chargino fields and of the lightest neutralino field. We generalize the latter result for the diagonal field renormalization constants of the other neutralino fields imposing Eq. (173) also for the components $k = 2, 3, 4$ —though we do not define them fully on-shell; see below. The imaginary parts of the diagonal field renormalization constants are still undefined. For the definition of the imaginary parts, we use Eqs. (176) and (178), where the latter one is generalized for the components $k = 2, 3, 4$ and

is imposed to hold also for those neutralinos. Now, for the charginos and the lightest neutralino Eqs. (176) and (178) already define the imaginary parts of $[\delta\mathbf{M}_{\tilde{\chi}^\pm}]_{ii}$ ($i = 1, 2$), and $[\delta\mathbf{M}_{\tilde{\chi}^0}]_{11}$, which means that a further condition for the imaginary part of the field renormalization constants of the charginos and the lightest neutralino is required, and we just set them to zero [see below Eqs. (185) and (188)] which is possible as all divergences are absorbed by other counter-terms. The off-diagonal field renormalization constants are fixed by the condition that

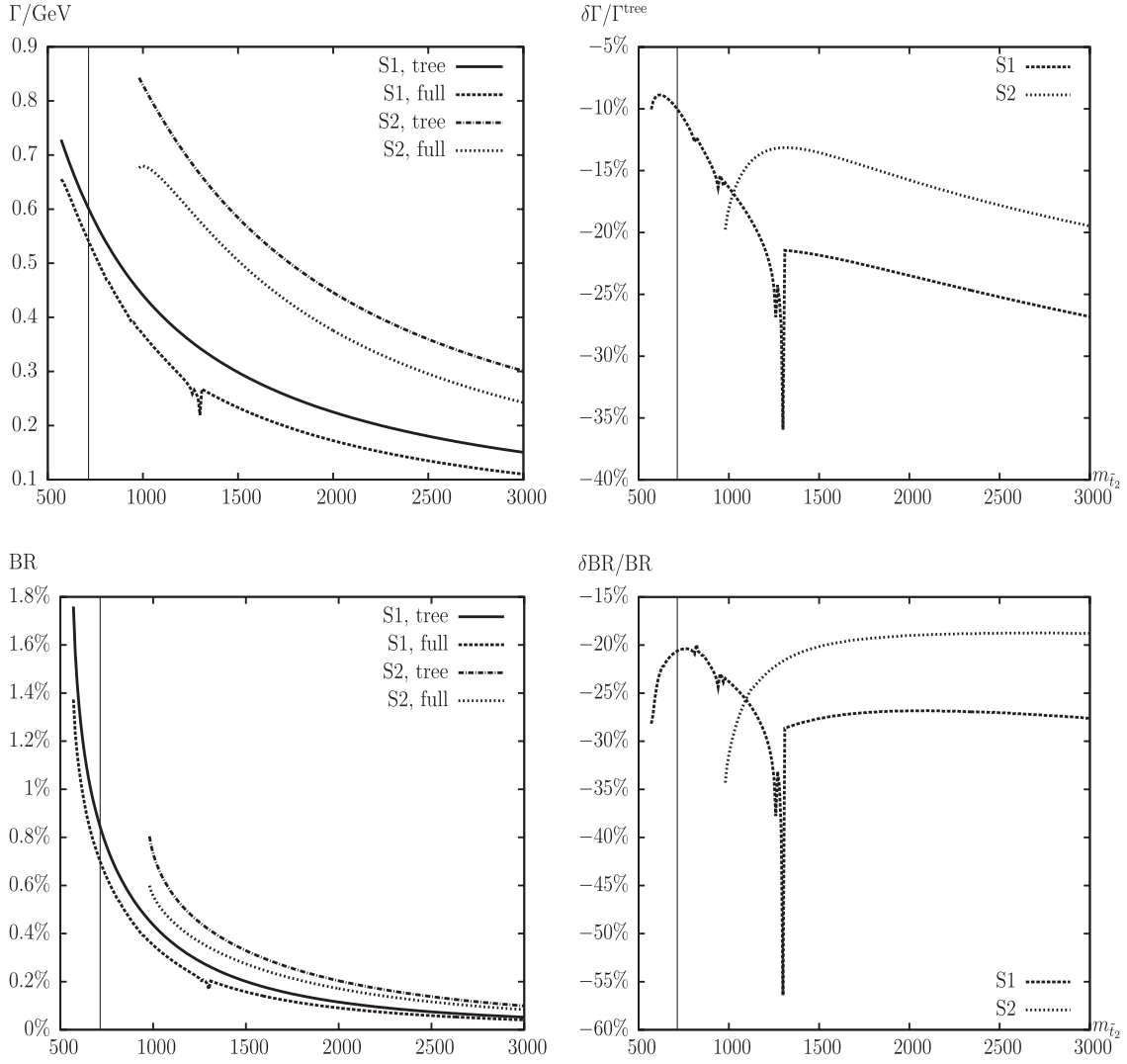


FIG. 9. $\Gamma(\tilde{t}_2 \rightarrow \tilde{t}_1 h_2)$. Tree-level and full one-loop corrected partial decay widths are shown with the parameters chosen according to S1 and S2 (see Table I), with $m_{\tilde{t}_2}$ varied. The upper left plot shows the partial decay width; the upper right plot shows the corresponding relative size of the corrections. The lower left plot shows the BR; the lower right plot shows the relative correction of the BR. The vertical lines indicate where $m_{\tilde{t}_2} + m_{\tilde{t}_1} = 1000$ GeV, i.e. the maximum reach of the ILC(1000).

$$([\widetilde{\text{Re}}\hat{\Sigma}_{\tilde{\chi}^-}(p)]_{ij}\tilde{\chi}_j^-(p))|_{p^2=m_{\tilde{\chi}_j^\pm}^2} = 0 \quad (i, j = 1, 2), \quad (182)$$

$$([\widetilde{\text{Re}}\hat{\Sigma}_{\tilde{\chi}^0}(p)]_{kl}\tilde{\chi}_l^0(p))|_{p^2=m_{\tilde{\chi}_l^0}^2} = 0 \quad (k, l = 1, 2, 3, 4). \quad (183)$$

Finally, this yields for the field renormalization constants [50],

$$\begin{aligned} \text{Re}[\delta\mathbf{Z}_{\tilde{\chi}^-}^{L/R}]_{ii} = & -\widetilde{\text{Re}}[\Sigma_{\tilde{\chi}^-}^{L/R}(m_{\tilde{\chi}_i^\pm}^2) + m_{\tilde{\chi}_i^\pm}^2(\Sigma_{\tilde{\chi}^-}^{L'}(m_{\tilde{\chi}_i^\pm}^2) \\ & + \Sigma_{\tilde{\chi}^-}^{R'}(m_{\tilde{\chi}_i^\pm}^2)) + m_{\tilde{\chi}_i^\pm}^2(\Sigma_{\tilde{\chi}^-}^{SL'}(m_{\tilde{\chi}_i^\pm}^2) \\ & + \Sigma_{\tilde{\chi}^-}^{SR'}(m_{\tilde{\chi}_i^\pm}^2))]_{ii}, \end{aligned} \quad (184)$$

$$\begin{aligned} \text{Im}[\delta\mathbf{Z}_{\tilde{\chi}^-}^{L/R}]_{ii} \\ = & \pm \frac{1}{m_{\tilde{\chi}_i^\pm}^2} \left[\frac{i}{2} \widetilde{\text{Re}} \left\{ \Sigma_{\tilde{\chi}^-}^{SR}(m_{\tilde{\chi}_i^\pm}^2) - \Sigma_{\tilde{\chi}^-}^{SL}(m_{\tilde{\chi}_i^\pm}^2) \right\} - \text{Im}\delta\mathbf{M}_{\tilde{\chi}^-} \right]_{ii} \\ := & 0, \end{aligned} \quad (185)$$

$$\begin{aligned} [\delta\mathbf{Z}_{\tilde{\chi}^-}^{L/R}]_{ij} = & \frac{2}{m_{\tilde{\chi}_i^\pm}^2 - m_{\tilde{\chi}_j^\pm}^2} \widetilde{\text{Re}}[m_{\tilde{\chi}_j^\pm}^2 \Sigma_{\tilde{\chi}^-}^{L/R}(m_{\tilde{\chi}_j^\pm}^2) \\ & + m_{\tilde{\chi}_i^\pm} m_{\tilde{\chi}_j^\pm} \Sigma_{\tilde{\chi}^-}^{R/L}(m_{\tilde{\chi}_j^\pm}^2) + m_{\tilde{\chi}_i^\pm}^2 \Sigma_{\tilde{\chi}^-}^{SL/SR}(m_{\tilde{\chi}_j^\pm}^2) \\ & + m_{\tilde{\chi}_j^\pm}^2 \Sigma_{\tilde{\chi}^-}^{SR/SL}(m_{\tilde{\chi}_j^\pm}^2) - m_{\tilde{\chi}_{ij}} \delta\mathbf{M}_{\tilde{\chi}^-} \\ & - m_{\tilde{\chi}_{ji}} \delta\mathbf{M}_{\tilde{\chi}^-}^\dagger]_{ij}, \end{aligned} \quad (186)$$

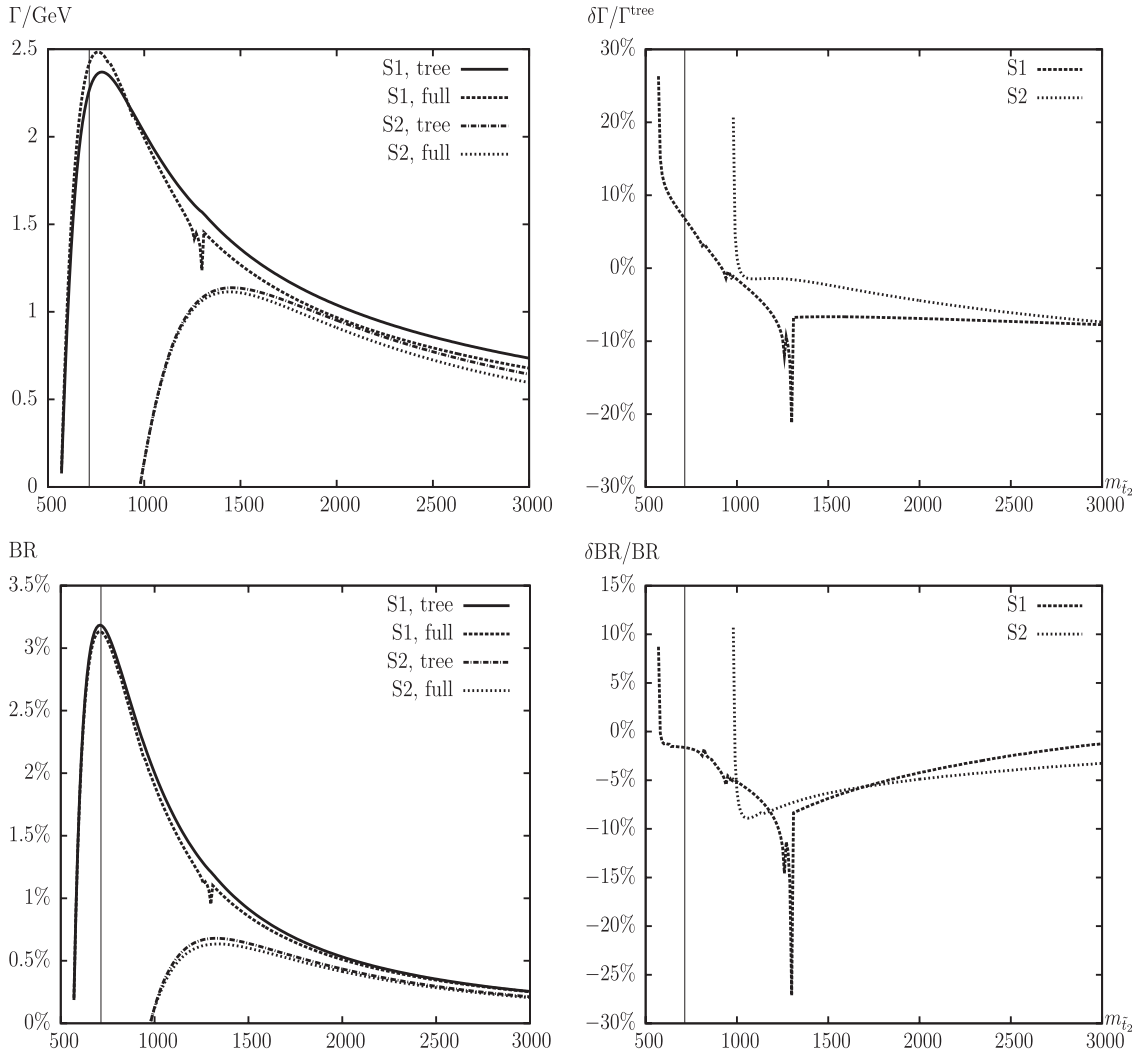


FIG. 10. $\Gamma(\tilde{t}_2 \rightarrow \tilde{t}_1 h_3)$. Tree-level and full one-loop corrected partial decay widths are shown with the parameters chosen according to S1 and S2 (see Table I), with $m_{\tilde{t}_2}$ varied. The upper left plot shows the partial decay width; the upper right plot shows the corresponding relative size of the corrections. The lower left plot shows the BR; the lower right plot shows the relative correction of the BR. The vertical lines indicate where $m_{\tilde{t}_2} + m_{\tilde{t}_1} = 1000$ GeV, i.e. the maximum reach of the ILC(1000).

$$\begin{aligned} \text{Re}[\delta\mathbf{Z}_{\tilde{\chi}^0}]_{kk} &= -\widetilde{\text{Re}}[\Sigma_{\tilde{\chi}^0}^L(m_{\tilde{\chi}_k^0}^2) + m_{\tilde{\chi}_k^0}^2(\Sigma_{\tilde{\chi}^0}^{L'}(m_{\tilde{\chi}_k^0}^2) \\ &\quad + \Sigma_{\tilde{\chi}^0}^{R'}(m_{\tilde{\chi}_k^0}^2)) + m_{\tilde{\chi}_k^0}(\Sigma_{\tilde{\chi}^0}^{SL'}(m_{\tilde{\chi}_k^0}^2) \\ &\quad + \Sigma_{\tilde{\chi}^0}^{SR'}(m_{\tilde{\chi}_k^0}^2))]_{kk}, \end{aligned} \quad (187)$$

$$\begin{aligned} \text{Im}[\delta\mathbf{Z}_{\tilde{\chi}^0}]_{kk} &= \frac{1}{m_{\tilde{\chi}_k^0}} \left[\frac{i}{2} \widetilde{\text{Re}}\{\Sigma_{\tilde{\chi}^0}^{SR}(m_{\tilde{\chi}_k^0}^2) - \Sigma_{\tilde{\chi}^0}^{SL}(m_{\tilde{\chi}_k^0}^2)\} \right. \\ &\quad \left. - \text{Im}\delta\mathbf{M}_{\tilde{\chi}^0} \right]_{kk}^{k=1}, \end{aligned} \quad (188)$$

$$\begin{aligned} [\delta\mathbf{Z}_{\tilde{\chi}^0}]_{kl} &= \frac{2}{m_{\tilde{\chi}_k^0}^2 - m_{\tilde{\chi}_l^0}^2} \widetilde{\text{Re}}[m_{\tilde{\chi}_l^0}^2 \Sigma_{\tilde{\chi}^0}^L(m_{\tilde{\chi}_l^0}^2) + m_{\tilde{\chi}_k^0} m_{\tilde{\chi}_l^0} \Sigma_{\tilde{\chi}^0}^R(m_{\tilde{\chi}_l^0}^2) \\ &\quad + m_{\tilde{\chi}_k^0} \Sigma_{\tilde{\chi}^0}^{SL}(m_{\tilde{\chi}_l^0}^2) + m_{\tilde{\chi}_l^0} \Sigma_{\tilde{\chi}^0}^{SR}(m_{\tilde{\chi}_k^0}^2) \\ &\quad - m_{\tilde{\chi}_k^0} \delta\mathbf{M}_{\tilde{\chi}^0} - m_{\tilde{\chi}_l^0} \delta\mathbf{M}_{\tilde{\chi}^0}^\dagger]_{kl}. \end{aligned} \quad (189)$$

The Eqs. (163) and (164) result in three on-shell masses in the neutralino/chargino sector. Therefore the three neutralino masses $m_{\tilde{\chi}_{2,3,4}^0}$, on the other hand, require a finite shift for their on-shell value. We have checked that this shift (for the scenarios under investigation in Sec. IV) is numerically small and does not change our results. Consequently, these shifts, though formally necessary, are not further taken into account to simplify the numerical evaluation.

The field renormalization constants for squark, quark, gluino, gauge boson as well as chargino and neutralino fields that have been derived in Secs. II A, II B, and II C are constructed via the multiplicative renormalization procedure in a symmetry conserving way, absorb the divergences accordingly, and are defined via on-shell renormalization conditions. In the presence of complex phases and nonvanishing absorptive parts of the self-energy type corrections, further wave function corrections

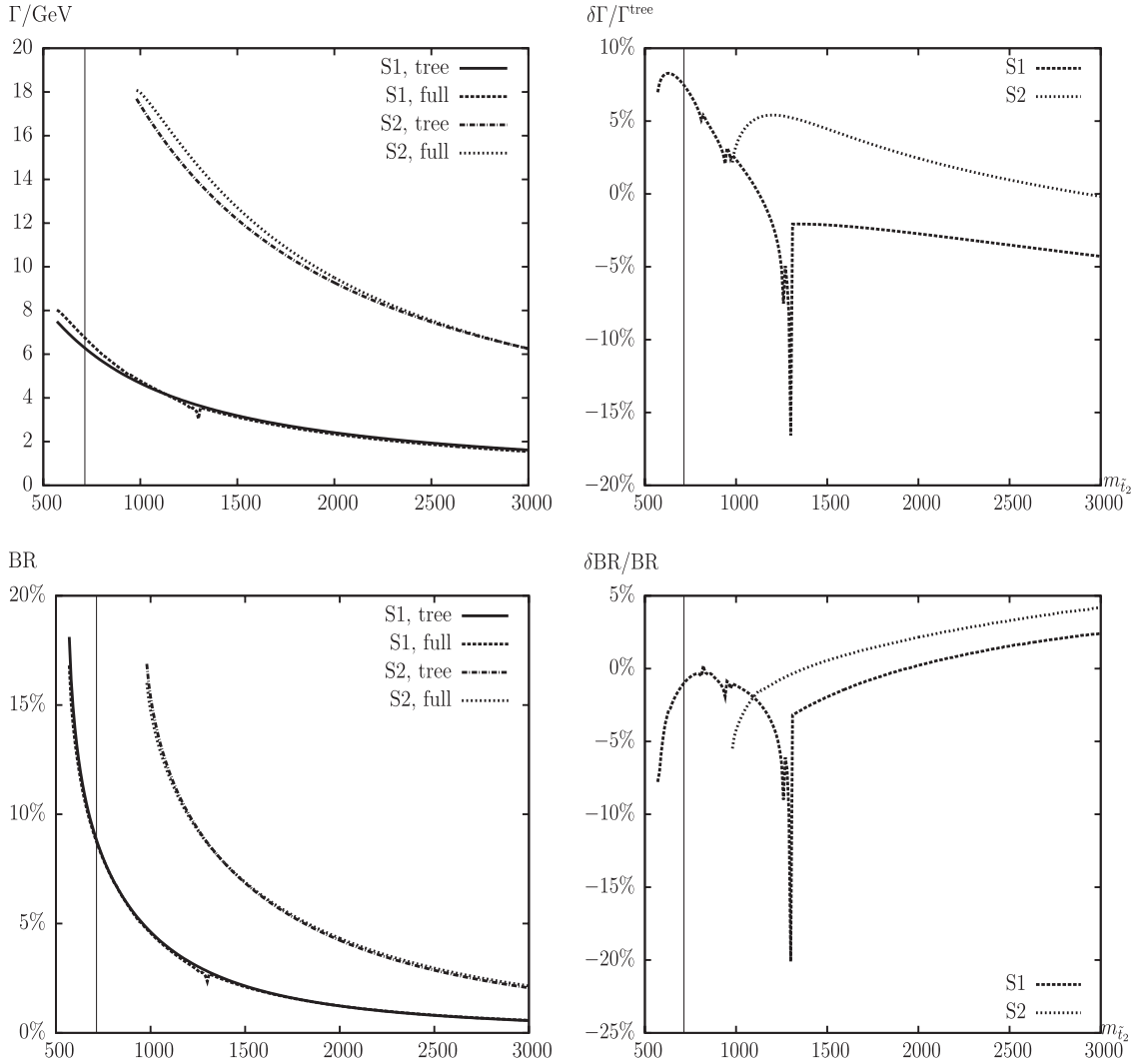


FIG. 11. $\Gamma(\tilde{t}_2 \rightarrow \tilde{t}_1 Z)$. Tree-level and full one-loop corrected partial decay widths are shown with the parameters chosen according to S1 and S2 (see Table I), with $m_{\tilde{t}_2}$ varied. The upper left plot shows the partial decay width; the upper right plot shows the corresponding relative size of the corrections. The lower left plot shows the BR; the lower right plot shows the relative correction of the BR. The vertical lines indicate where $m_{\tilde{t}_2} + m_{\tilde{t}_1} = 1000$ GeV, i.e. the maximum reach of the ILC(1000).

may arise that are not part of the field renormalization constant but can be taken into account by additional Z factors; see the Appendix.

III. CALCULATION OF LOOP DIAGRAMS

In this section we give some details about the calculation of the higher-order corrections to the partial decay widths of scalar quarks. Sample diagrams are shown in Figs. 1–7. Not shown are the diagrams for real (hard or soft) photon and gluon radiation. They are obtained from the corresponding tree-level diagrams by attaching a photon (gluon) to the electrically (color) charged particles. The internal generically depicted particles in Figs. 1–7 are labeled as follows: F can be a SM fermion f , chargino $\tilde{\chi}_j^\pm$ or neutralino $\tilde{\chi}_k^0$, or gluino \tilde{g} ; S can be a sfermion \tilde{f}_i or a

Higgs boson h_n ; V can be a photon γ , gluon g , or a massive SM gauge boson, Z or W^\pm . For internally appearing Higgs bosons no higher-order corrections to their masses or couplings are taken into account; these corrections would correspond to effects beyond one-loop order.¹⁸ For external Higgs bosons, as described in Sec. II B, the appropriate Z factors are applied and on-shell masses (including higher-order corrections) are used.

Also not shown are the diagrams with a gauge boson (Goldstone-)Higgs boson self-energy contribution on the external Higgs boson leg. They appear in the decay $\tilde{t}_2 \rightarrow \tilde{t}_1 h_n$, Fig. 1, with a $Z/G - h_n$ transition and in the

¹⁸We found that using loop corrected Higgs boson masses in the loops leads to a UV divergent result.

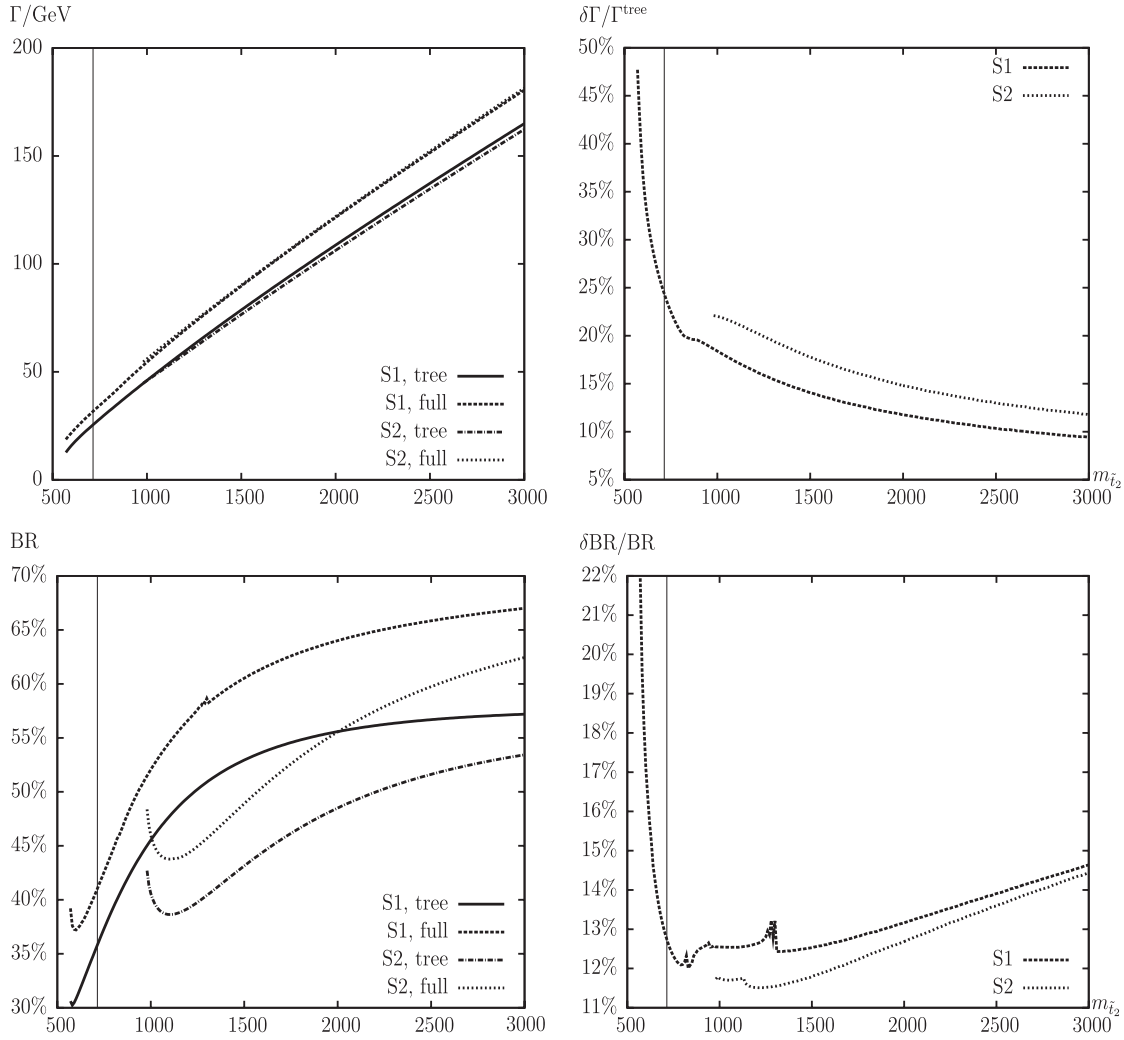


FIG. 12. $\Gamma(\tilde{t}_2 \rightarrow t\tilde{g})$. Tree-level and full one-loop corrected partial decay widths are shown with the parameters chosen according to S1 and S2 (see Table I), with $m_{\tilde{t}_2}$ varied. The upper left plot shows the partial decay width; the upper right plot shows the corresponding relative size of the corrections. The lower left plot shows the BR; the lower right plot shows the relative correction of the BR. The vertical lines indicate where $m_{\tilde{t}_2} + m_{\tilde{t}_1} = 1000$ GeV, i.e. the maximum reach of the ILC(1000).

decay $\tilde{t}_2 \rightarrow \tilde{b}_i H^+$, Fig. 6, with a $W^+/G^+ - H^+$ transition.¹⁹ The corresponding self-energy diagram belonging to the process $\tilde{t}_2 \rightarrow \tilde{t}_1 Z$ or $\tilde{t}_2 \rightarrow \tilde{b}_i W^+$, respectively, yields a vanishing contribution for external on-shell gauge bosons due to $\varepsilon \cdot p = 0$ for $p^2 = M_Z^2$ ($p^2 = M_W^2$), where p denotes the external momentum and ε the polarization vector of the gauge boson.

Furthermore, in general, in Figs. 1–7 we have omitted diagrams with self-energy type corrections of external (on-shell) particles. While the contributions from the real parts of the loop functions are taken into account via the renormalization constants defined by on-shell renormalization

¹⁹From a technical point of view, the $W^+/G^+ - H^+$ transitions have been absorbed into the respective counterterms, while the $Z/G - h_n$ transitions have been calculated explicitly.

conditions, the contributions coming from the imaginary part of the loop functions can result in an additional (real) correction if multiplied by complex parameters (such as A_i). In the analytical and numerical evaluation, these diagrams have been taken into account via the prescription described in the Appendix. The impact of these contributions will be discussed in Sec. IV.

Within our one-loop calculation we neglect finite width effects that can help to cure threshold singularities. Consequently, in the close vicinity of those thresholds our calculation does not give a reasonable result. Switching to a complex mass scheme [66] would be another possibility to cure this problem, but its application is beyond the scope of our paper.

Finally it should be noted that the purely loop induced decay channels $\tilde{t}_2 \rightarrow \tilde{t}_1 \gamma/g$ yield exactly zero due to the

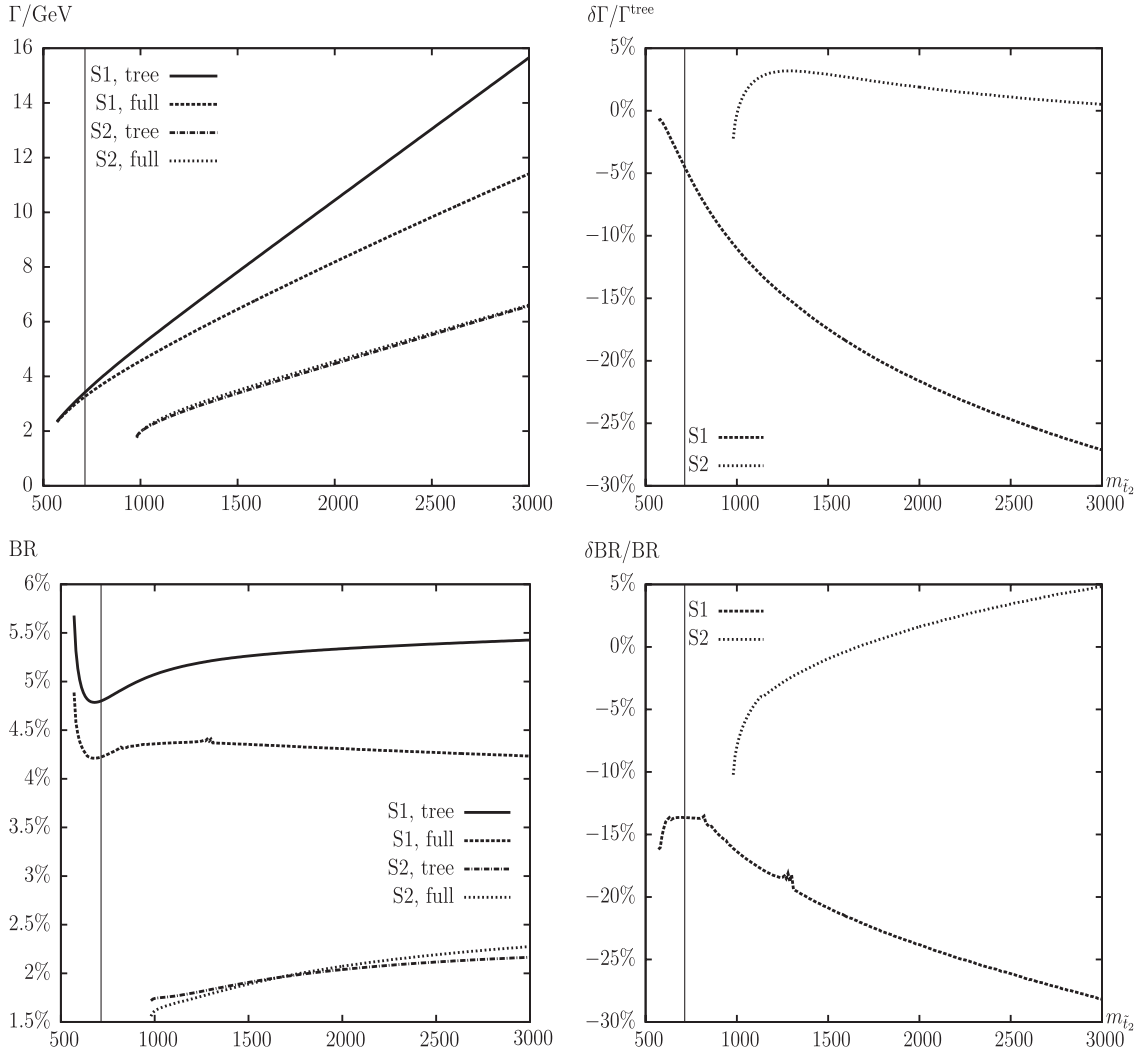


FIG. 13. $\Gamma(\tilde{t}_2 \rightarrow t\tilde{\chi}_1^0)$. Tree-level and full one-loop corrected partial decay widths are shown with the parameters chosen according to S1 and S2 (see Table I), with $m_{\tilde{t}_2}$ varied. The upper left plot shows the partial decay width; the upper right plot shows the corresponding relative size of the corrections. The lower left plot shows the BR; the lower right plot shows the relative correction of the BR. The vertical lines indicate where $m_{\tilde{t}_2} + m_{\tilde{t}_1} = 1000$ GeV, i.e. the maximum reach of the ILC(1000).

fact that the decay width is proportional to $\varepsilon \cdot p$ and the photon/gluon is on-shell, i.e. $\varepsilon \cdot p = 0$.

The diagrams and corresponding amplitudes have been obtained with FEYNARTS [67]. The model file, including the MSSM counterterms, is largely based on Ref. [50], however, adjusted to match exactly the renormalization prescription described in Sec. II. The further evaluation has been performed with FORMCALC [68].

A. Ultraviolet divergences

As regularization scheme for the UV divergences we have used constrained differential renormalization [69], which has been shown to be equivalent to dimensional reduction [70] at the one-loop level [68]. Thus the employed regularization scheme preserves SUSY [71,72] and guarantees that the SUSY relations are kept intact, e.g.

that the gauge couplings of the SM vertices and the Yukawa couplings of the corresponding SUSY vertices also coincide to one-loop order in the SUSY limit. Therefore no additional shifts, which might occur when using a different regularization scheme, arise. All UV divergences cancel in the final result.

B. Infrared divergences

The IR divergences from diagrams with an internal photon or gluon have to cancel with the ones from the corresponding real soft radiation. In the case of QED we have included the soft photon contribution following the description given in Ref. [61]. In the case of QCD we have modified this prescription by replacing the product of electric charges by the appropriate combination of color charges (linear combination of C_A and C_F times α_s). The

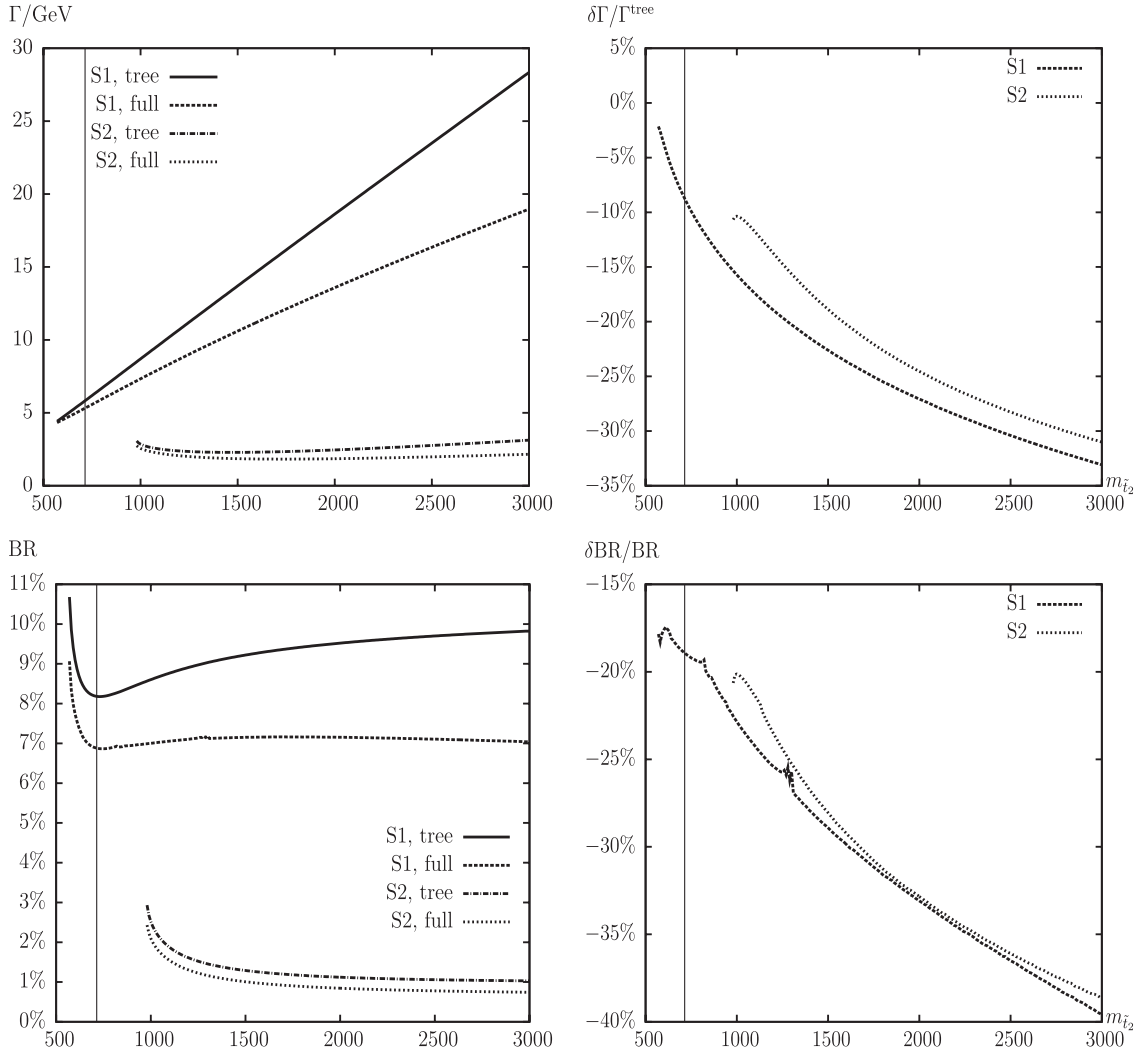


FIG. 14. $\Gamma(\tilde{t}_2 \rightarrow t\tilde{\chi}_2^0)$. Tree-level and full one-loop corrected partial decay widths are shown with the parameters chosen according to S1 and S2 (see Table I), with $m_{\tilde{t}_2}$ varied. The upper left plot shows the partial decay width; the upper right plot shows the corresponding relative size of the corrections. The lower left plot shows the BR; the lower right plot shows the relative correction of the BR. The vertical lines indicate where $m_{\tilde{t}_2} + m_{\tilde{t}_1} = 1000$ GeV, i.e. the maximum reach of the ILC(1000).

IR divergences arising from the diagrams involving a γ (or a g) are regularized by introducing a photon (or gluon) mass parameter, λ . While for the QED part this procedure always works, in the QCD part due to its non-Abelian character this method can fail. However, since no triple or quartic gluon vertices appear, λ can indeed be used as a regulator (the appearance of the non-Abelian gluino-gluino-gluon vertex does not pose a problem here [12]). All IR divergences, i.e. all divergences in the limit $\lambda \rightarrow 0$, cancel once virtual and real diagrams for one decay channel are added.

Special care has to be taken in the decay modes involving scalar bottom quarks. Using tree-level sbottom masses yields a cancellation of IR divergences to all orders for all \tilde{t}_2 decay modes. However, inserting the one-loop corrected sbottom masses (see Sec. II A 1), as required for

consistency, we found cancellation to all orders of the related IR divergences, except for the decay modes $\tilde{t}_2 \rightarrow \tilde{b}_i W^+$. Within these decays the tree-level relation required by the $SU(2)$ symmetry $M_{\tilde{q}_L}(\tilde{t}) = M_{\tilde{q}_L}(\tilde{b})$, corresponding to

$$\begin{aligned} & |U_{\tilde{b}_{11}}|^2 m_{\tilde{b}_1}^2 + |U_{\tilde{b}_{12}}|^2 m_{\tilde{b}_2}^2 \\ &= |U_{\tilde{t}_{11}}|^2 m_{\tilde{t}_1}^2 + |U_{\tilde{t}_{12}}|^2 m_{\tilde{t}_2}^2 - m_t^2 + m_b^2 - M_W^2 \cos 2\beta, \end{aligned} \quad (190)$$

has to be fulfilled to yield a cancellation of all IR divergences.²⁰ On the other hand, the requirement of on-shell sbottom

²⁰Equation (190) has been deduced via $M_{\tilde{q}_L}^2 = |U_{\tilde{q}_{11}}|^2 m_{\tilde{q}_1}^2 + |U_{\tilde{q}_{12}}|^2 m_{\tilde{q}_2}^2 - M_Z^2 c_{2\beta}(J_q^3 - Q_q s_W^2) - m_q^2$.

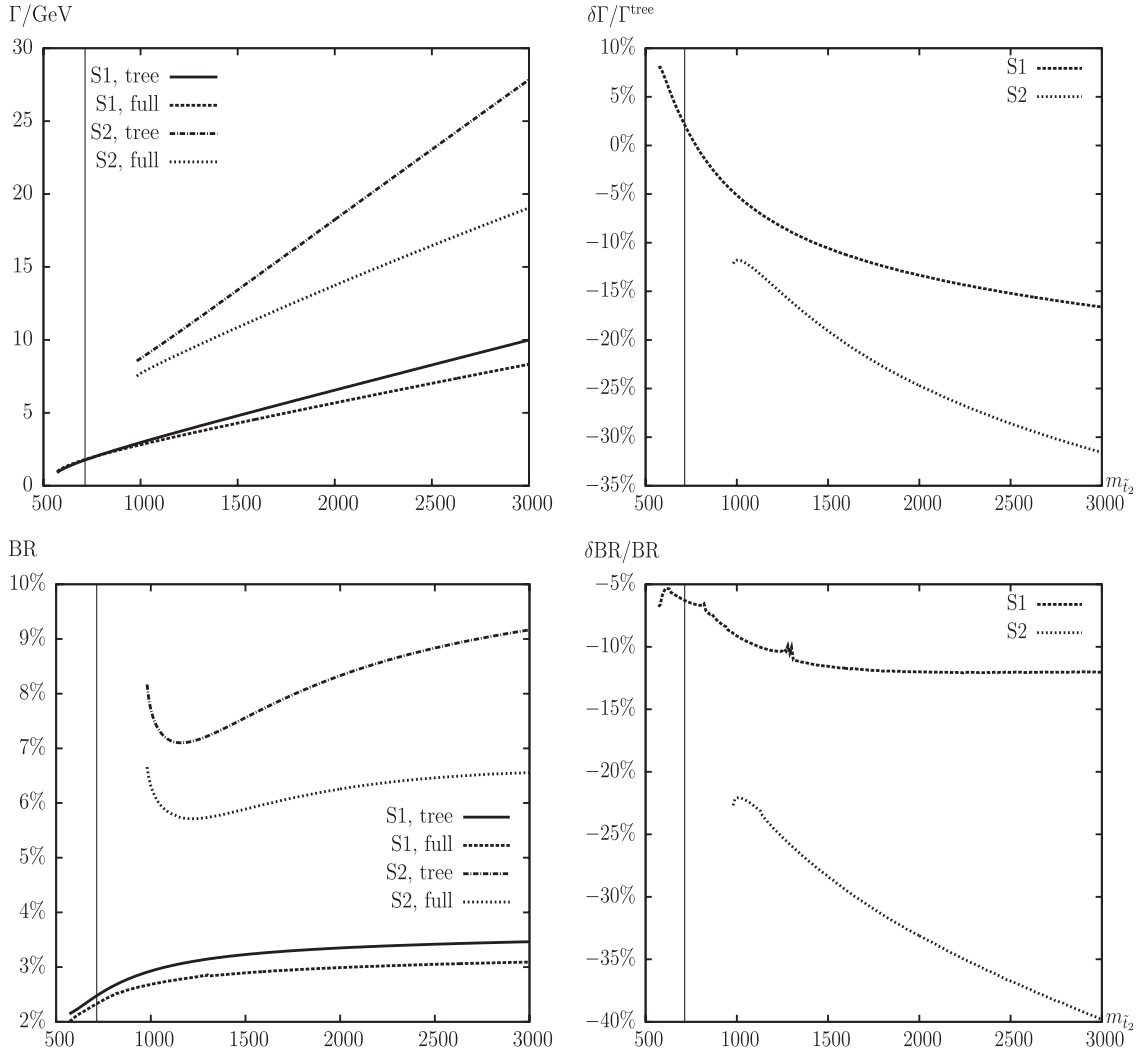


FIG. 15. $\Gamma(\tilde{\tau}_2 \rightarrow \tilde{\tau}_3^0)$. Tree-level and full one-loop corrected partial decay widths are shown with the parameters chosen according to S1 and S2 (see Table I), with $m_{\tilde{\tau}_2}$ varied. The upper left plot shows the partial decay width; the upper right plot shows the corresponding relative size of the corrections. The lower left plot shows the BR; the lower right plot shows the relative correction of the BR. The vertical lines indicate where $m_{\tilde{\tau}_2} + m_{\tilde{\tau}_1} = 1000$ GeV, i.e. the maximum reach of the ILC(1000).

masses as well as an intact $SU(2)$ relation at the one-loop level leads to the necessity of a shift in the scalar bottom masses; see Eq. (48). Therefore Eq. (190) is “violated” at the one-loop level, introducing a two-loop IR divergence in $\Gamma(\tilde{\tau}_2 \rightarrow \tilde{b}_i W^+)$. In order to eliminate this two-loop IR divergence we introduced a counterterm in the $\tilde{\tau}_2 \tilde{b}_i W$ vertex,

$$\delta Z_{\text{ir}} = (|U_{\tilde{b}_{11}}|^2 m_{\tilde{b}_1}^2 + |U_{\tilde{b}_{12}}|^2 m_{\tilde{b}_2}^2) - [|U_{\tilde{b}_{11}}|^2 m_{\tilde{b}_1}^2 + |U_{\tilde{b}_{12}}|^2 m_{\tilde{b}_2}^2]_{\text{shift}} \times \text{IRdiv}, \quad (191)$$

to restore the tree-level $SU(2)$ relation. The left term in Eq. (191) contains only “tree-level” values, while the index “shift” refers to inserting the one-loop masses and mixing matrices. The IR divergence has been taken from Eq. (B.5)

of Ref. [73] (it can also be found in Ref. [74]), and reads (in our case)

$$\text{IRdiv} = \frac{\alpha}{6\pi M_W} \left[\frac{2x_t \ln(x_t)}{m_{\tilde{\tau}_2}(1-x_t^2)} \ln\left(\frac{m_{\tilde{\tau}_2} M_W}{\lambda^2}\right) - \frac{x_b \ln(x_b)}{m_{\tilde{b}_i}(1-x_b^2)} \ln\left(\frac{m_{\tilde{b}_i} M_W}{\lambda^2}\right) \right] \quad (192)$$

with

$$x_t = \frac{\sqrt{1 - 4m_{\tilde{\tau}_2} M_W / (m_{\tilde{b}_i}^2 + i0 - (M_W - m_{\tilde{\tau}_2})^2)} - 1}{\sqrt{1 - 4m_{\tilde{\tau}_2} M_W / (m_{\tilde{b}_i}^2 + i0 - (M_W - m_{\tilde{\tau}_2})^2)} + 1}, \quad (193)$$

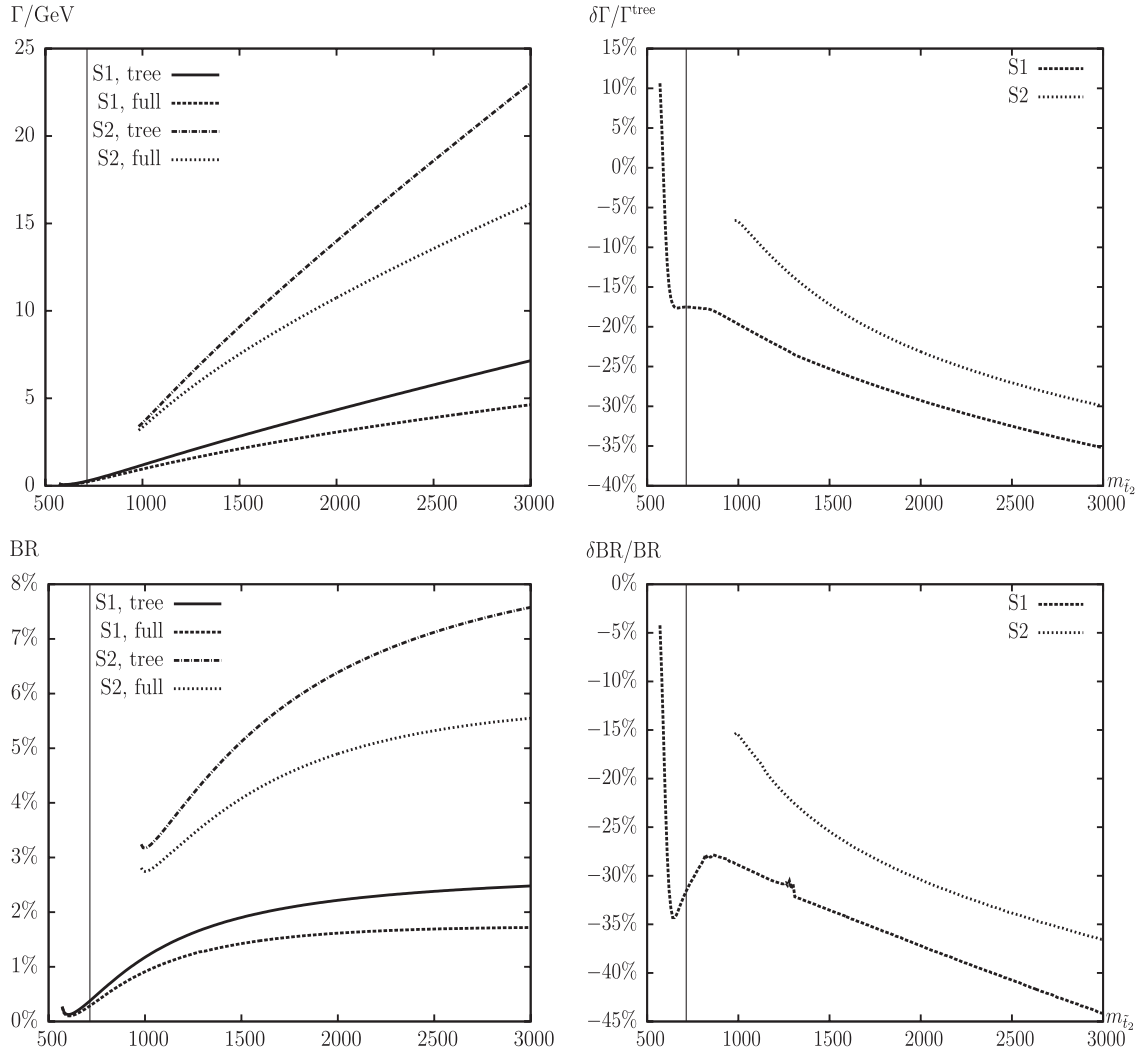


FIG. 16. $\Gamma(\tilde{t}_2 \rightarrow t \tilde{\chi}_4^0)$. Tree-level and full one-loop corrected partial decay widths are shown with the parameters chosen according to S1 and S2 (see Table I), with $m_{\tilde{t}_2}$ varied. The upper left plot shows the partial decay width; the upper right plot shows the corresponding relative size of the corrections. The lower left plot shows the BR; the lower right plot shows the relative correction of the BR. The vertical lines indicate where $m_{\tilde{t}_2} + m_{\tilde{t}_1} = 1000$ GeV, i.e. the maximum reach of the ILC(1000).

$$x_b = \frac{\sqrt{1 - 4m_{\tilde{b}_i}M_W/(m_{\tilde{t}_2}^2 + i0 - (M_W - m_{\tilde{b}_i})^2)} - 1}{\sqrt{1 - 4m_{\tilde{b}_i}M_W/(m_{\tilde{t}_2}^2 + i0 - (M_W - m_{\tilde{b}_i})^2)} + 1}, \quad (194)$$

where $i0$ denotes an infinitesimally small imaginary part. After including this tree-level relation restoring counterterm we find an IR finite result to all orders as required.

We have furthermore checked that our result does not depend on ΔE defining the energy cut that separates the soft from the hard radiation. Our numerical results have been obtained for $\Delta E = 10^{-5} \times m_{\tilde{t}_2}$.

C. Tree-level formulas

For completeness we show here also the formulas that have been used to calculate the tree-level decay widths:

$$\Gamma^{\text{tree}}(\tilde{t}_2 \rightarrow \tilde{t}_1 h_n) = \frac{|C(\tilde{t}_2, \tilde{t}_1, h_n)|^2 \lambda^{1/2}(m_{\tilde{t}_2}^2, m_{\tilde{t}_1}^2, m_{h_n}^2)}{16\pi m_{\tilde{t}_2}^3} \quad (n = 1, 2, 3), \quad (195)$$

$$\Gamma^{\text{tree}}(\tilde{t}_2 \rightarrow \tilde{t}_1 Z) = \frac{|C(\tilde{t}_2, \tilde{t}_1, Z)|^2 \lambda^{3/2}(m_{\tilde{t}_2}^2, m_{\tilde{t}_1}^2, M_Z^2)}{16\pi M_Z^2 m_{\tilde{t}_2}^3}, \quad (196)$$

$$\begin{aligned} \Gamma^{\text{tree}}(\tilde{t}_2 \rightarrow t \tilde{g}) &= [(|C(\tilde{t}_2, t, \tilde{g})_L|^2 + |C(\tilde{t}_2, t, \tilde{g})_R|^2) \\ &\quad \times (m_{\tilde{t}_2}^2 - m_t^2 - m_{\tilde{g}}^2) \\ &\quad - 4 \text{Re}\{C(\tilde{t}_2, t, \tilde{g})_L^* C(\tilde{t}_2, t, \tilde{g})_R\} m_t m_{\tilde{g}}] \\ &\quad \times \frac{4}{3} \frac{\lambda^{1/2}(m_{\tilde{t}_2}^2, m_t^2, m_{\tilde{g}}^2)}{16\pi m_{\tilde{t}_2}^3}, \quad (197) \end{aligned}$$

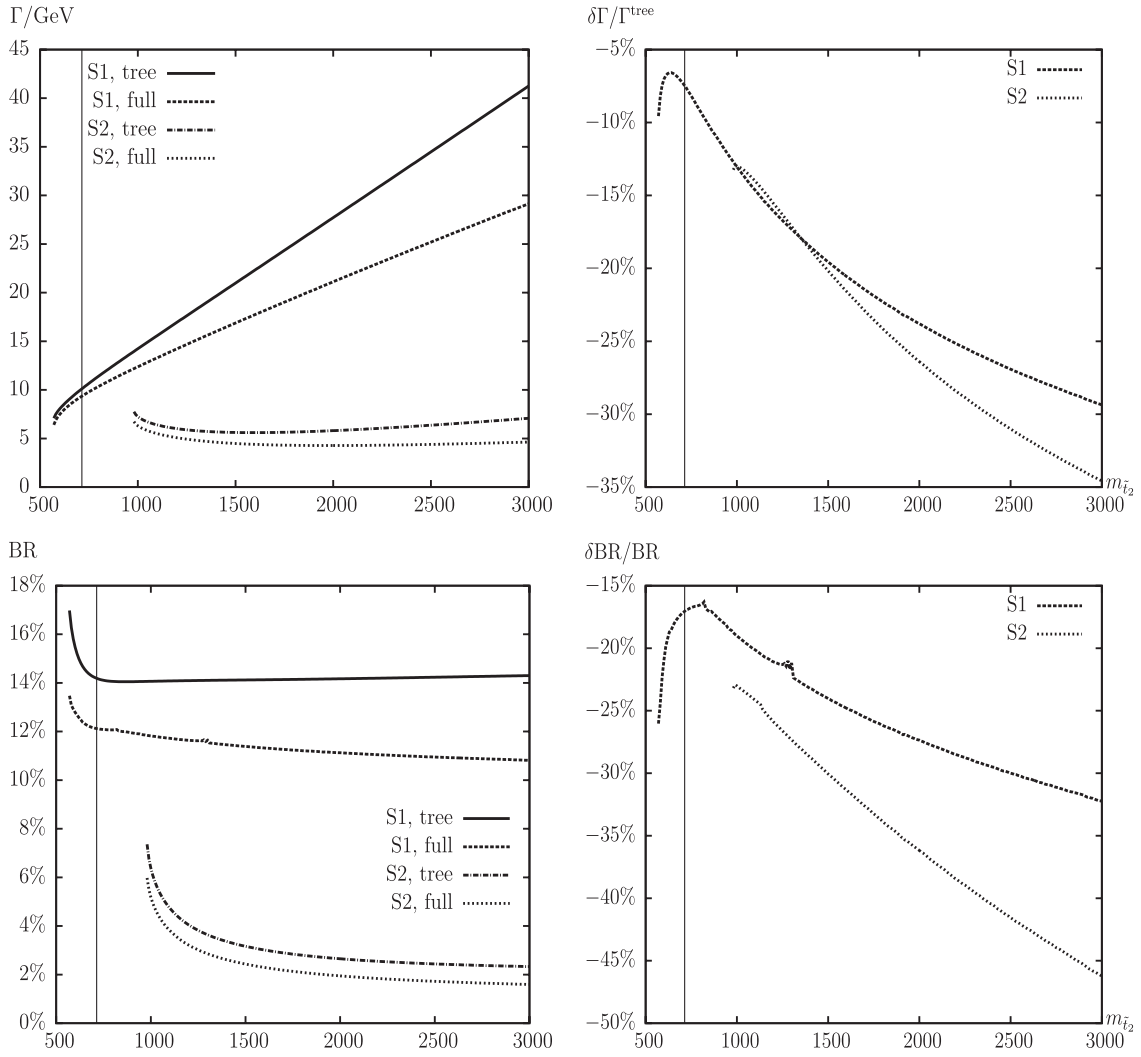


FIG. 17. $\Gamma(\tilde{\tau}_2 \rightarrow b\tilde{\chi}_1^+)$. Tree-level and full one-loop corrected partial decay widths are shown with the parameters chosen according to S1 and S2 (see Table I), with $m_{\tilde{\tau}_2}$ varied. The upper left plot shows the partial decay width; the upper right plot shows the corresponding relative size of the corrections. The lower left plot shows the BR; the lower right plot shows the relative correction of the BR. The vertical lines indicate where $m_{\tilde{\tau}_2} + m_{\tilde{\tau}_1} = 1000$ GeV, i.e. the maximum reach of the ILC(1000).

$$\Gamma^{\text{tree}}(\tilde{\tau}_2 \rightarrow t\tilde{\chi}_k^0) = [(|C(\tilde{\tau}_2, t, \tilde{\chi}_k^0)_L|^2 + |C(\tilde{\tau}_2, t, \tilde{\chi}_k^0)_R|^2)(m_{\tilde{\tau}_2}^2 - m_t^2 - m_{\tilde{\chi}_k^0}^2) - 4 \text{Re}\{C(\tilde{\tau}_2, t, \tilde{\chi}_k^0)_L^* C(\tilde{\tau}_2, t, \tilde{\chi}_k^0)_R\}m_t m_{\tilde{\chi}_k^0}] \times \frac{\lambda^{1/2}(m_{\tilde{\tau}_2}^2, m_t^2, m_{\tilde{\chi}_k^0}^2)}{16\pi m_{\tilde{\tau}_2}^3} \quad (k = 1, 2, 3, 4), \quad (198)$$

$$\Gamma^{\text{tree}}(\tilde{\tau}_2 \rightarrow b\tilde{\chi}_j^+) = [(|C(\tilde{\tau}_2, b, \tilde{\chi}_j^+)_L|^2 + |C(\tilde{\tau}_2, b, \tilde{\chi}_j^+)_R|^2)(m_{\tilde{\tau}_2}^2 - m_b^2 - m_{\tilde{\chi}_j^+}^2) - 4 \text{Re}\{C(\tilde{\tau}_2, b, \tilde{\chi}_j^+)_L^* C(\tilde{\tau}_2, b, \tilde{\chi}_j^+)_R\}m_b m_{\tilde{\chi}_j^+}] \times \frac{\lambda^{1/2}(m_{\tilde{\tau}_2}^2, m_b^2, m_{\tilde{\chi}_j^+}^2)}{16\pi m_{\tilde{\tau}_2}^3} \quad (j = 1, 2), \quad (199)$$

$$\Gamma^{\text{tree}}(\tilde{\tau}_2 \rightarrow \tilde{b}_i H^+) = \frac{|C(\tilde{\tau}_2, \tilde{b}_i, H^+)|^2 \lambda^{1/2}(m_{\tilde{\tau}_2}^2, m_{\tilde{b}_i}^2, M_{H^\pm}^2)}{16\pi m_{\tilde{\tau}_2}^3} \quad (i = 1, 2), \quad (200)$$

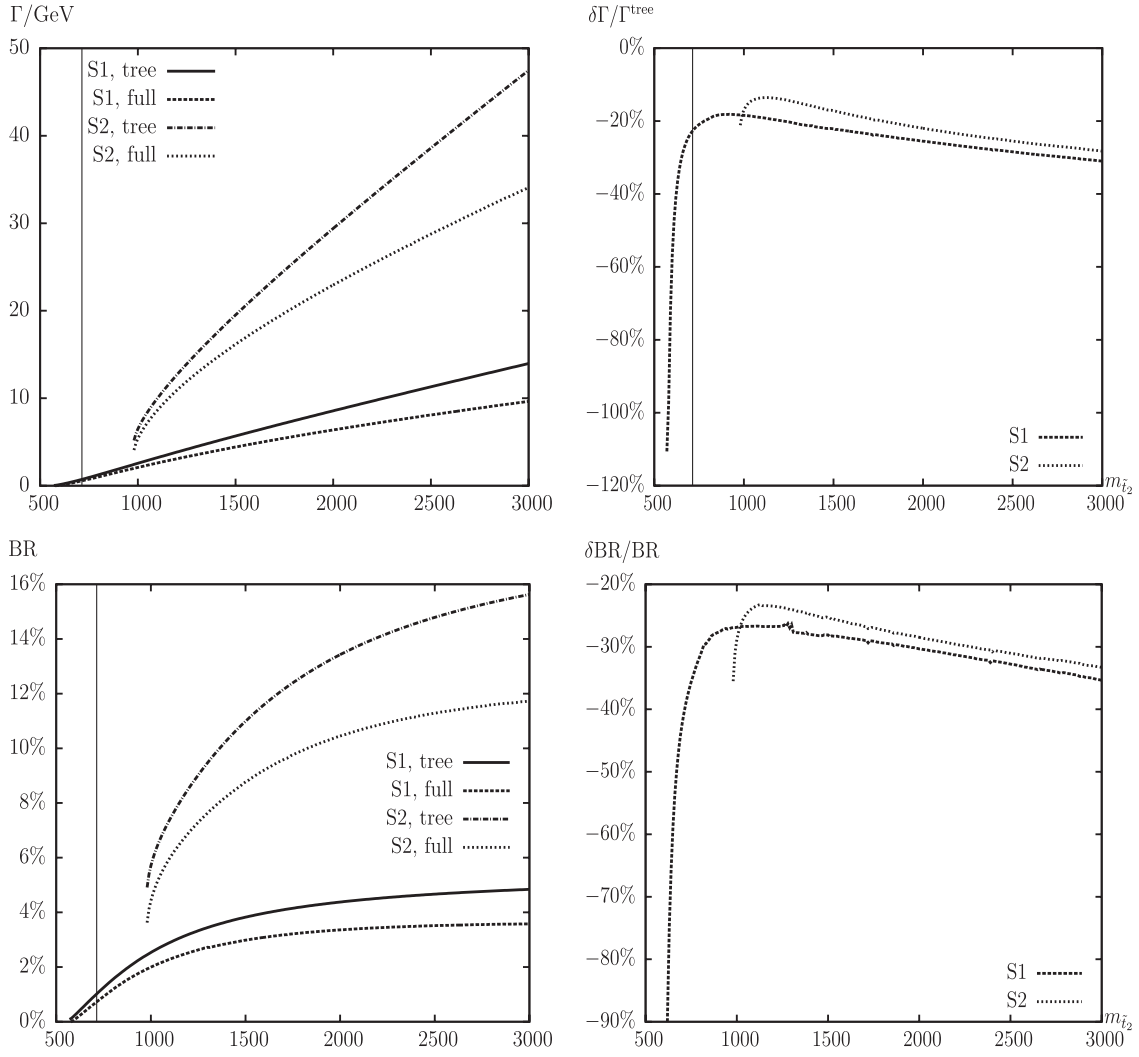


FIG. 18. $\Gamma(\tilde{t}_2 \rightarrow b\tilde{\chi}_2^+)$. Tree-level and full one-loop corrected partial decay widths are shown with the parameters chosen according to S1 and S2 (see Table I), with $m_{\tilde{t}_2}$ varied. The upper left plot shows the partial decay width; the upper right plot shows the corresponding relative size of the corrections. The lower left plot shows the BR; the lower right plot shows the relative correction of the BR. The vertical lines indicate where $m_{\tilde{t}_2} + m_{\tilde{t}_1} = 1000$ GeV, i.e. the maximum reach of the ILC(1000).

$$\Gamma^{\text{tree}}(\tilde{t}_2 \rightarrow \tilde{b}_i W^+) = \frac{|C(\tilde{t}_2, \tilde{b}_i, W^+)|^2 \lambda^{3/2}(m_{\tilde{t}_2}^2, m_{\tilde{b}_i}^2, M_W^2)}{16\pi M_W^2 m_{\tilde{t}_2}^3} \quad (i = 1, 2), \quad (201)$$

where $\lambda(x, y, z) = (x - y - z)^2 - 4yz$ and the couplings $C(a, b, c)$ can be found in the FEYNARTS model files [75]. $C(a, b, c)_{L,R}$ denote the part of the coupling that is proportional to $(\mathbb{1} \mp \gamma_5)/2$.

IV. NUMERICAL ANALYSIS

In this section we present a numerical analysis of all 15 decay channels. In the various figures below we show the partial decay widths and their relative correction at the tree-level (“tree”) and at the one-loop level (“full”),

$$\Gamma^{\text{tree}} \equiv \Gamma^{\text{tree}}(\tilde{t}_2 \rightarrow xy), \quad (202)$$

$$\Gamma^{\text{full}} \equiv \Gamma^{\text{full}}(\tilde{t}_2 \rightarrow xy), \quad (203)$$

$$\delta\Gamma/\Gamma^{\text{tree}} \equiv \frac{\Gamma^{\text{full}} - \Gamma^{\text{tree}}}{\Gamma^{\text{tree}}}, \quad (204)$$

where xy denotes the specific final state. The total decay width is defined as the sum of all 15 partial decay widths,

$$\Gamma_{\text{tot}}^{\text{tree}} \equiv \sum_{xy} \Gamma^{\text{tree}}(\tilde{t}_2 \rightarrow xy), \quad \Gamma_{\text{tot}}^{\text{full}} \equiv \sum_{xy} \Gamma^{\text{full}}(\tilde{t}_2 \rightarrow xy),$$

$$\delta\Gamma_{\text{tot}}/\Gamma_{\text{tot}}^{\text{tree}} \equiv \frac{\Gamma_{\text{tot}}^{\text{full}} - \Gamma_{\text{tot}}^{\text{tree}}}{\Gamma_{\text{tot}}^{\text{tree}}}. \quad (205)$$

We also show the absolute and relative changes of the branching ratios,

$$\text{BR}^{\text{tree}} \equiv \frac{\Gamma^{\text{tree}}(\tilde{t}_2 \rightarrow xy)}{\Gamma_{\text{tot}}^{\text{tree}}}, \quad (206)$$

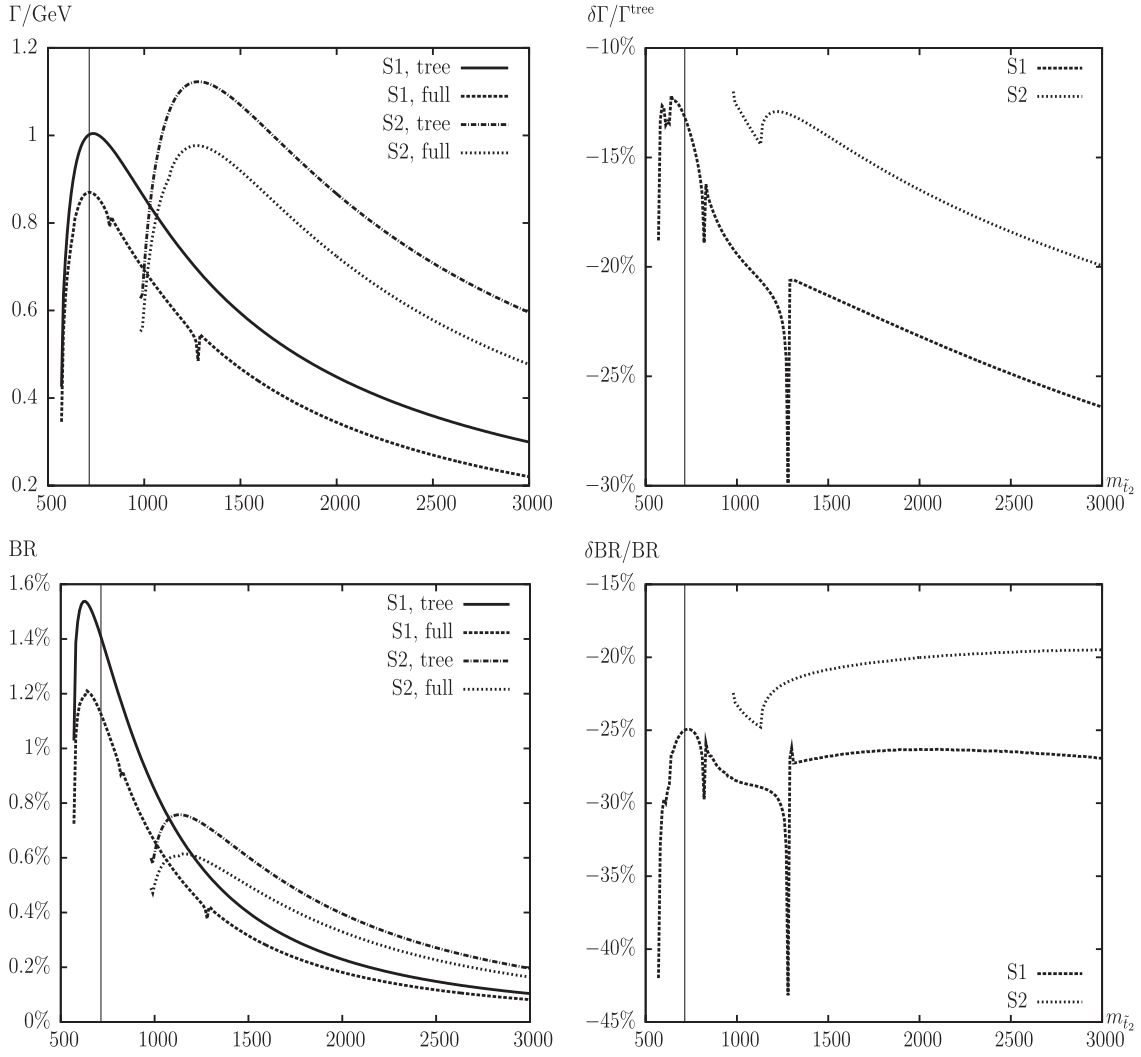


FIG. 19. $\Gamma(\tilde{t}_2 \rightarrow \tilde{b}_1 H^+)$. Tree-level and full one-loop corrected partial decay widths are shown with the parameters chosen according to S1 and S2 (see Table I), with $m_{\tilde{t}_2}$ varied. The upper left plot shows the partial decay width; the upper right plot shows the corresponding relative size of the corrections. The lower left plot shows the BR; the lower right plot shows the relative correction of the BR. The vertical lines indicate where $m_{\tilde{t}_2} + m_{\tilde{t}_1} = 1000$ GeV, i.e. the maximum reach of the ILC(1000).

$$\text{BR}^{\text{full}} \equiv \frac{\Gamma^{\text{full}}(\tilde{t}_2 \rightarrow xy)}{\Gamma_{\text{tot}}^{\text{full}}}, \quad (207)$$

$$\delta\text{BR}/\text{BR} \equiv \frac{\text{BR}^{\text{full}} - \text{BR}^{\text{tree}}}{\text{BR}^{\text{full}}}. \quad (208)$$

The last quantity is crucial to analyze the impact of the one-loop corrections on the phenomenology at the LHC and the ILC.

A. Parameter settings

The renormalization scale μ_R has been set to the mass of the decaying particle, i.e. $\mu_R = m_{\tilde{t}_2}$. The SM parameters are chosen as follows, see also [44]²¹:

²¹Using the most up-to-date values from Ref. [76] would have a negligible impact on our numerical results.

- (i) Fermion masses (on-shell masses, if not indicated differently):

$$\begin{aligned} m_e &= 0.51099891 \text{ MeV}, & m_{\nu_e} &= 0 \text{ MeV}, \\ m_\mu &= 105.658367 \text{ MeV}, & m_{\nu_\mu} &= 0 \text{ MeV}, \\ m_\tau &= 1776.84 \text{ MeV}, & m_{\nu_\tau} &= 0 \text{ MeV}, \\ m_u &= 53.8 \text{ MeV}, & m_d &= 53.8 \text{ MeV}, \\ m_c &= 1.27 \text{ GeV}, & m_s &= 104 \text{ MeV}, \\ m_t &= 171.2 \text{ GeV}, & m_b(m_b) &= 4.2 \text{ GeV}. \end{aligned} \quad (209)$$

According to Ref. [44], m_s is an estimate of a so-called ‘‘current quark mass’’ in the $\overline{\text{MS}}$ scheme at the scale $\mu \approx 2$ GeV. m_c and m_b are the ‘‘running’’ masses in the $\overline{\text{MS}}$ scheme. The top quark mass as

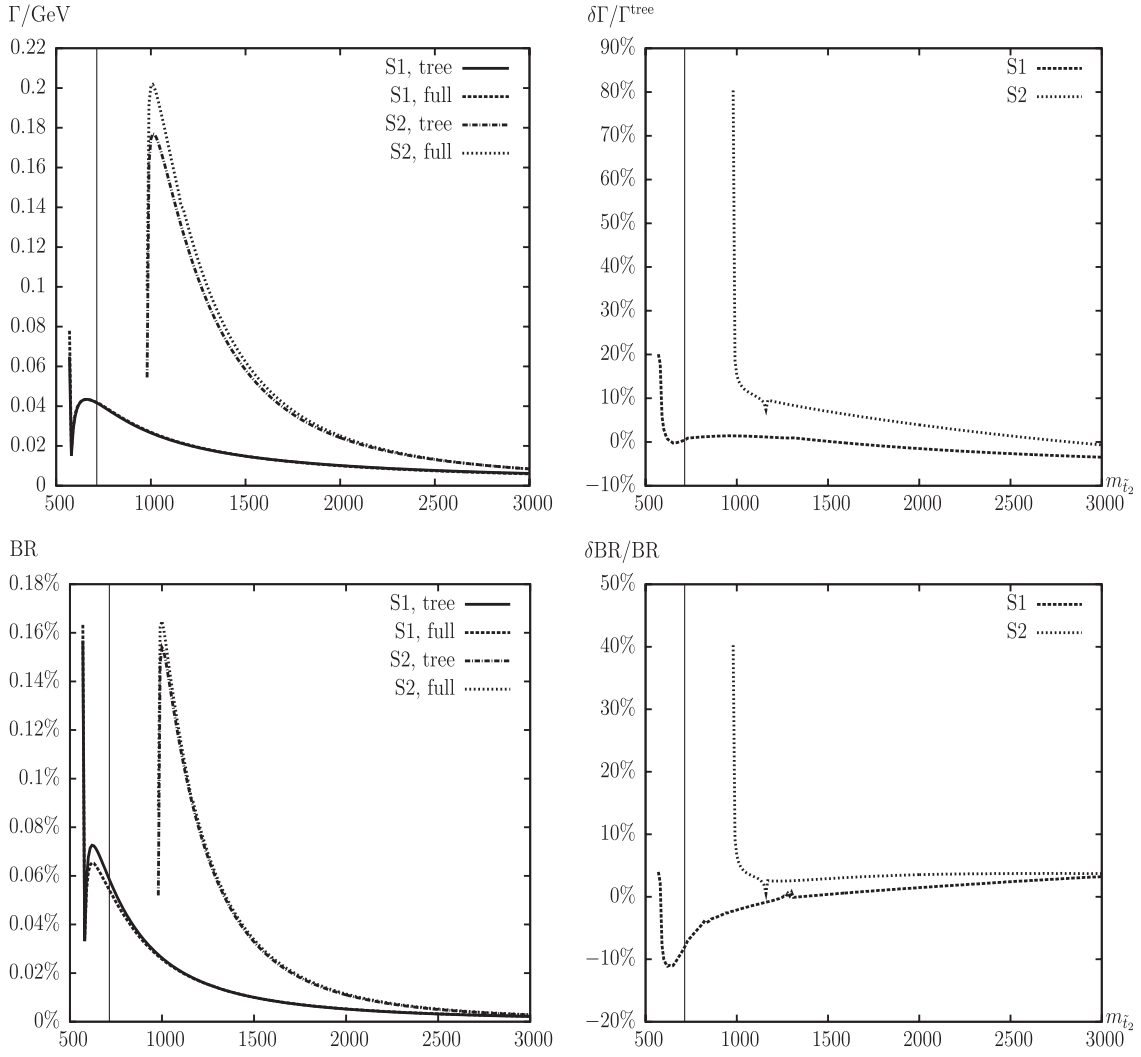


FIG. 20. $\Gamma(\tilde{t}_2 \rightarrow \tilde{b}_2 H^+)$. Tree-level and full one-loop corrected partial decay widths are shown with the parameters chosen according to S1 and S2 (see Table I), with $m_{\tilde{t}_2}$ varied. The upper left plot shows the partial decay width; the upper right plot shows the corresponding relative size of the corrections. The lower left plot shows the BR; the lower right plot shows the relative correction of the BR. The vertical lines indicate where $m_{\tilde{t}_2} + m_{\tilde{t}_1} = 1000$ GeV, i.e. the maximum reach of the ILC(1000).

well as the lepton masses are defined OS. m_u and m_d are effective parameters, calculated through the hadronic contributions to

$$\Delta\alpha_{\text{had}}^{(5)}(M_Z) = \frac{\alpha}{\pi} \sum_{f=u,c,d,s,b} Q_f^2 \left(\ln \frac{M_Z^2}{m_f^2} - \frac{5}{3} \right). \quad (210)$$

- (ii) The CKM matrix has been set to unity.
- (iii) Gauge boson masses:

$$M_Z = 91.1876 \text{ GeV}, \quad M_W = 80.398 \text{ GeV}. \quad (211)$$

- (iv) Coupling constants:

$$\alpha = \frac{e^2}{4\pi} = 1/137.0359895, \quad (212)$$

$$\alpha_s(M_Z) = 0.1176,$$

where the running and decoupling of α_s can be found in Sec. II A 3.

The Higgs sector quantities (masses, mixings, etc.) have been evaluated using FEYNHIGGS (version 2.6.5) [34–37].²²

We will show the results for some representative numerical examples. The parameters are chosen according to the two scenarios, S1 and S2, shown in Table I, but with one of the parameters varied. The scenarios are defined such that *all* decay modes are open simultaneously to permit an analysis of all channels, i.e. not picking specific parameters for each decay. We will start with a variation of $m_{\tilde{t}_2}$, and show later the results for varying φ_{A_i} . The scenarios are in agreement with

²²As default value within FEYNHIGGS, $\mu_R = m_t$ is used. Furthermore we have neglected the (in our case small) corrections of $\mathcal{O}(\alpha_b \alpha_s, \alpha_t \alpha_b, \alpha_b^2)$ (via a small modification in the code) and used the top pole mass for the evaluation of the MSSM Higgs boson sector quantities.

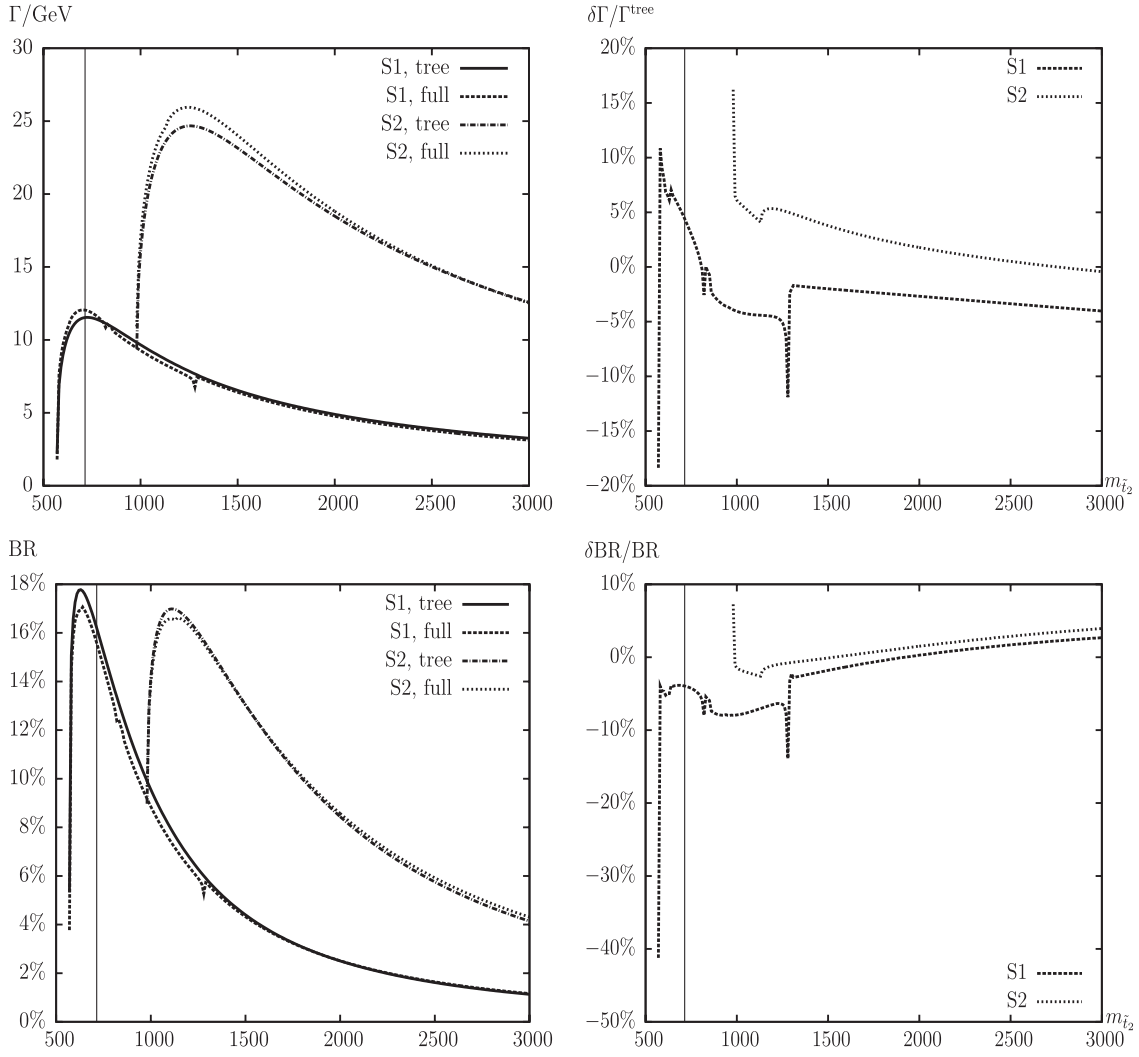


FIG. 21. $\Gamma(\tilde{t}_2 \rightarrow \tilde{b}_1 W^+)$. Tree-level and full one-loop corrected partial decay widths are shown with the parameters chosen according to S1 and S2 (see Table I), with $m_{\tilde{t}_2}$ varied. The upper left plot shows the partial decay width; the upper right plot shows the corresponding relative size of the corrections. The lower left plot shows the BR; the lower right plot shows the relative correction of the BR. The vertical lines indicate where $m_{\tilde{t}_2} + m_{\tilde{t}_1} = 1000$ GeV, i.e. the maximum reach of the ILC(1000).

the MSSM Higgs boson searches at LEP [78,79]. Too small values of the lightest Higgs boson mass would be reached for $\tan\beta \lesssim 9.4(4.6)$ within S1 (S2) as given in Table I.²³ In order to avoid completely unrealistic spectra, the following exclusion limits [44] hold in our two scenarios²⁴:

$$\begin{aligned}
 m_{\tilde{t}_1} &> 95 \text{ GeV}, & m_{\tilde{b}_1} &> 89 \text{ GeV}, & m_{\tilde{q}} &> 379 \text{ GeV}, \\
 m_{\tilde{e}_1} &> 73 \text{ GeV}, & m_{\tilde{\chi}_1^0} &> 46 \text{ GeV}, \\
 m_{\tilde{\chi}_1^\pm} &> 94 \text{ GeV}, & m_{\tilde{g}} &> 308 \text{ GeV}. & & (213)
 \end{aligned}$$

²³While in these scenarios we are not aiming to yield a light Higgs boson mass value around ~ 125 GeV, it should be noted that such a value is in principle in agreement with not too heavy scalar top quarks [80] that can be produced via $e^+e^- \rightarrow \tilde{t}_1^+ \tilde{t}_2^-$ at the ILC(1000).

²⁴The relatively light scalar quark masses and especially the light gluino mass are potentially in conflict with recent SUSY searches at the LHC [81] (although no fully model-independent results have been published). However, as stressed above, the parameters are chosen to be able to analyze as many decay modes as possible *simultaneously*. For a *realistic* collider analysis these bounds [81] will have to be taken into account.

A few examples of the scalar top and bottom quark masses in S1 and S2 are shown in Table II. The values of $m_{\tilde{t}_2}$ allow copious production of the heavier stop at the LHC. For other choices of the gluino mass, $m_{\tilde{g}} > m_{\tilde{t}_2}$, which would leave no visible effect for most of the decay modes of the \tilde{t}_2 , the heavier stop could also be produced in gluino decays at the LHC. Furthermore, in S1 (even for the nominal value of $m_{\tilde{t}_2}$ as given in Table I) the production of \tilde{t}_2 at the ILC(1000), i.e. with $\sqrt{s} = 1000$ GeV, via $e^+e^- \rightarrow \tilde{t}_1^+ \tilde{t}_2^-$ will be possible, with all the subsequent decay modes (1)–(7) being open. The clean environment

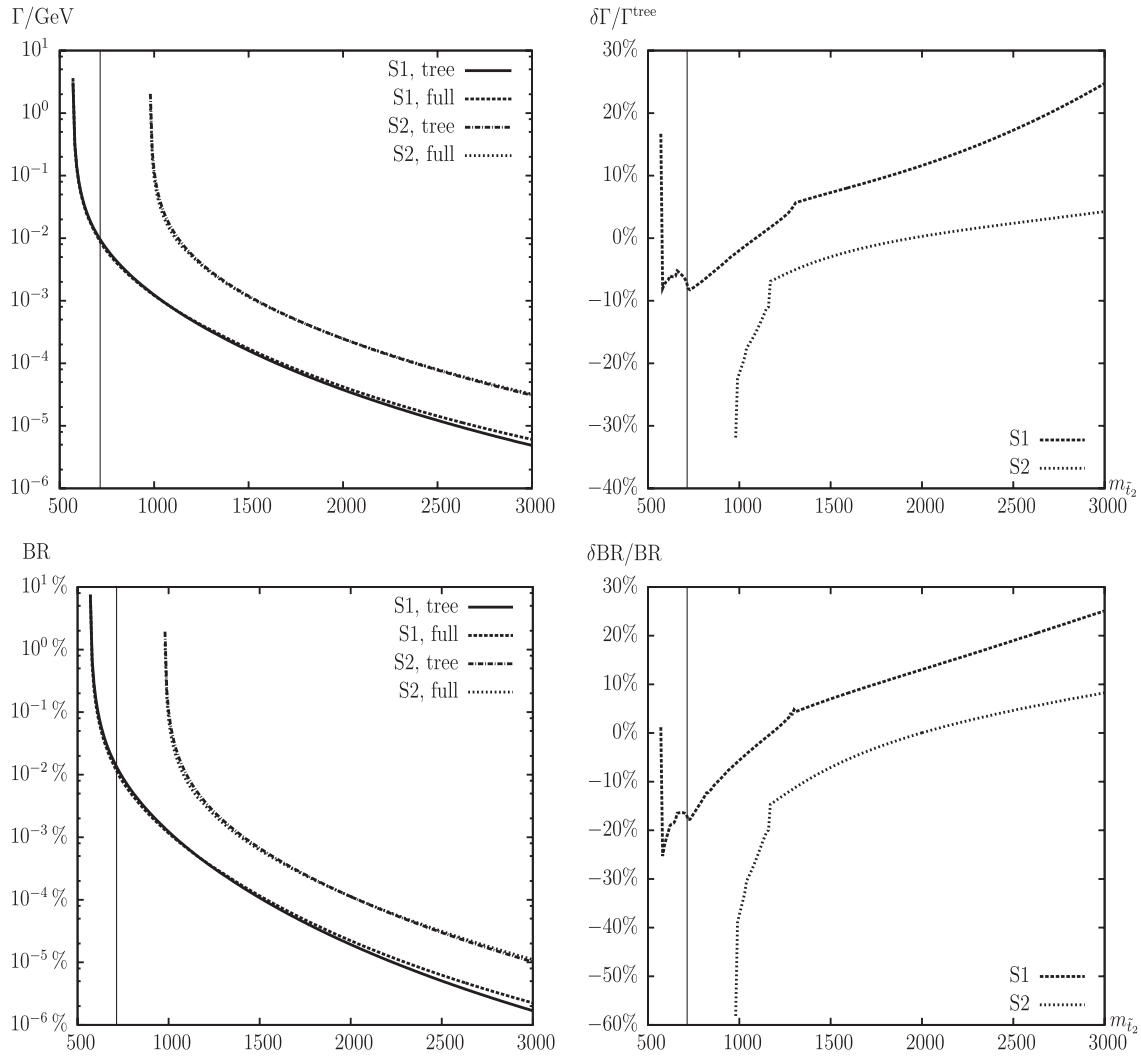


FIG. 22. $\Gamma(\tilde{t}_2 \rightarrow \tilde{b}_2 W^+)$. Tree-level and full one-loop corrected partial decay widths are shown with the parameters chosen according to S1 and S2 (see Table I), with $m_{\tilde{t}_2}$ varied. The upper left plot shows the partial decay width; the upper right plot shows the corresponding relative size of the corrections. The lower left plot shows the BR; the lower right plot shows the relative correction of the BR. The vertical lines indicate where $m_{\tilde{t}_2} + m_{\tilde{t}_1} = 1000$ GeV, i.e. the maximum reach of the ILC(1000).

of the ILC would permit a detailed study of the scalar top decays. For the lowest values shown in the plots below, $m_{\tilde{t}_2} \gtrsim 570$ GeV, we find (via a tree-level calculation) $\sigma(e^+e^- \rightarrow \tilde{t}_1^+ \tilde{t}_2) \approx 1.5$ fb, i.e. an integrated luminosity of ~ 1 ab^{-1} would yield about 1500 \tilde{t}_2 . This number drops to $\sim 280\tilde{t}_2$ for the masses shown in Table II. The ILC environment would result in an accuracy of the relative branching ratio [Eq. (208)] close to the statistical uncertainty: a BR of 30% could be determined to $\sim 5\%$ for the lowest $m_{\tilde{t}_2}$ values and to about 11% for the values given in Table II. Depending on the combination of allowed decay channels a determination of the branching ratios at the few percent level might be achievable in the high-luminosity running of the ILC(1000).

The numerical results we will show in the next subsections are of course dependent on choice of the SUSY

parameters. Nevertheless, they give an idea of the relevance of the full one-loop corrections. As an example, the largest decay width is $\Gamma(\tilde{t}_2 \rightarrow t\tilde{g})$, dominating the total decay width, Γ_{tot} , and thus the various branching ratios. For other choices of $m_{\tilde{g}}$ with $m_{\tilde{g}} > m_{\tilde{t}_2}$ the corrections to the decay widths would stay the same, but the branching ratios would look very different. Channels (and their respective one-loop corrections) that may look unobservable due to the smallness of their BR in the plots shown below, could become important if other channels are kinematically forbidden.

B. Full one-loop results for varying $m_{\tilde{t}_2}$

The results shown in this and the following subsections consist of tree, which denotes the tree-level value and of

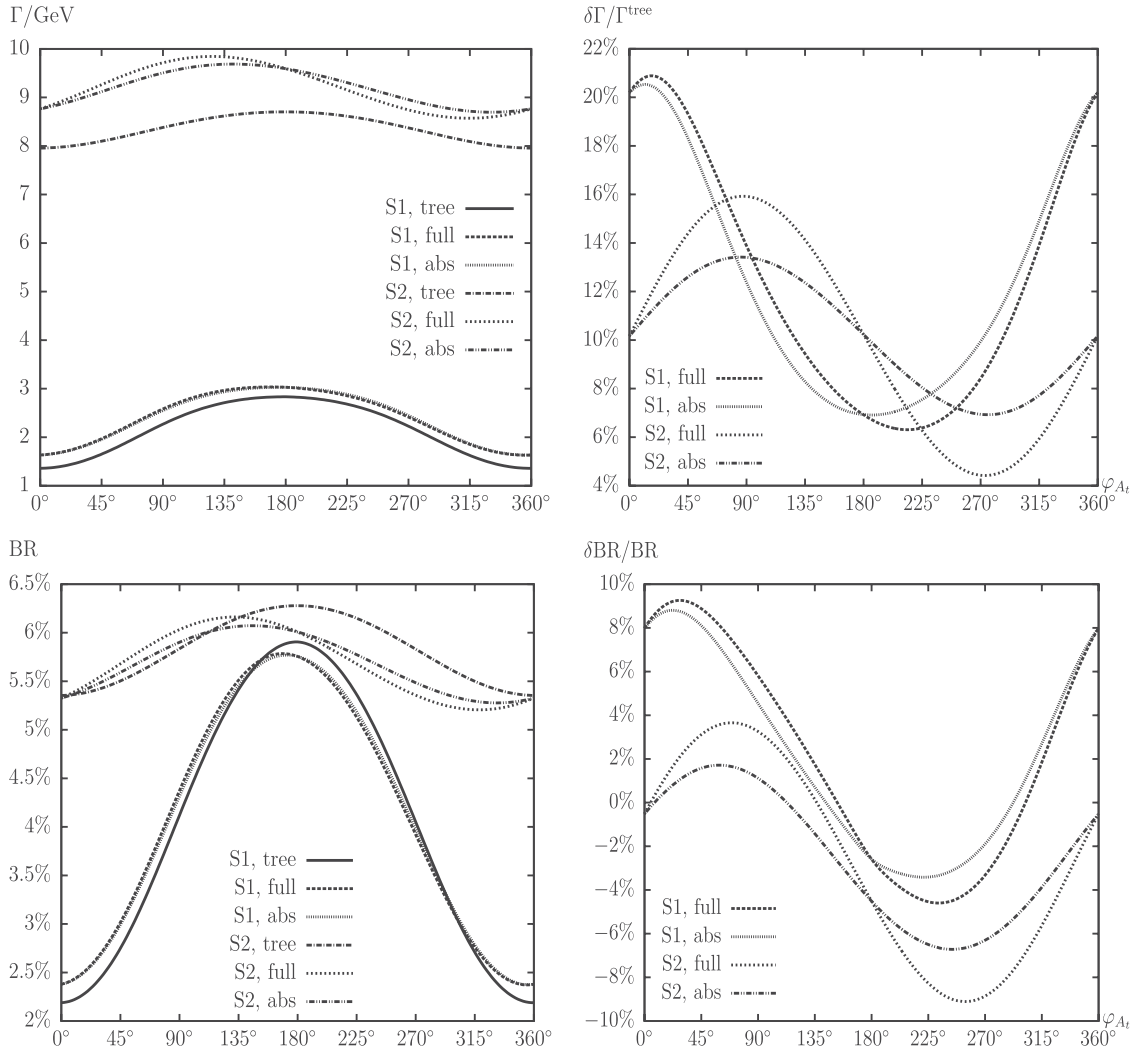


FIG. 23. $\Gamma(\tilde{t}_2 \rightarrow \tilde{t}_1 h_1)$. Tree-level (tree) and full one-loop (full) corrected partial decay widths are shown. Also shown are the full one-loop corrected partial decay widths including absorptive contributions (“abs”). The parameters are chosen according to S1 and S2 (see Table I), with φ_{A_t} varied. The upper left plot shows the partial decay width; the upper right plot shows the corresponding relative size of the corrections. The lower left plot shows the BR; the lower right plot shows the relative correction of the BR.

full, which is the partial decay width including *all* one-loop corrections as described in Sec. III. We start the numerical analysis with partial decay widths of \tilde{t}_2 evaluated as a function of $m_{\tilde{t}_2}$, starting at $m_{\tilde{t}_2} = 570$ GeV up to $m_{\tilde{t}_2} = 3$ TeV, which roughly coincides with the reach of the LHC for high-luminosity running. The upper panels contain the results for the absolute value of the various partial decay widths, $\Gamma(\tilde{t}_2 \rightarrow xy)$ (left) and the relative correction from the full one-loop contributions (right). The lower panels show the same results for $\text{BR}(\tilde{t}_2 \rightarrow xy)$.

Since in this section all parameters are chosen to be real, no contributions from absorptive parts of self-energy type corrections on external legs can contribute. This will be different in Sec. IV C.

In Figs. 8–10 we show the results for the process $\tilde{t}_2 \rightarrow \tilde{t}_1 h_n$ ($n = 1, 2, 3$) as a function of $m_{\tilde{t}_2}$. These are of particular interest for LHC analyses [8,9] (as emphasized

in the Introduction). The dips at $m_{\tilde{t}_2} \approx 819, 948, 971, 1264, 1303$ GeV (for all three figures) in the scenario S1 are effects due to the thresholds $m_t + m_{\tilde{\chi}_{1,2,3,4}^0} = m_{\tilde{t}_1}$ and $m_t + m_{\tilde{g}} = m_{\tilde{t}_1}$ (in this order) of the self-energies $\Sigma_{\tilde{t}_{1,2}}(m_{\tilde{t}_1}^2)$ in the renormalization constants $[\delta Z_{\tilde{t}}]_{11,21}$, δY_t , and $\delta m_{\tilde{t}_1}^2$. One can see that the size of the corrections of the partial decay widths is especially large very close to the production threshold²⁵ from which on the considered decay mode is kinematically possible. Away from this

²⁵It should be noted that a calculation very close to the production threshold requires the inclusion of additional (non-relativistic) contributions, which is beyond the scope of this paper. Consequently, very close to the production threshold our calculation (at the tree- or loop level) does not provide a very accurate description of the decay width.

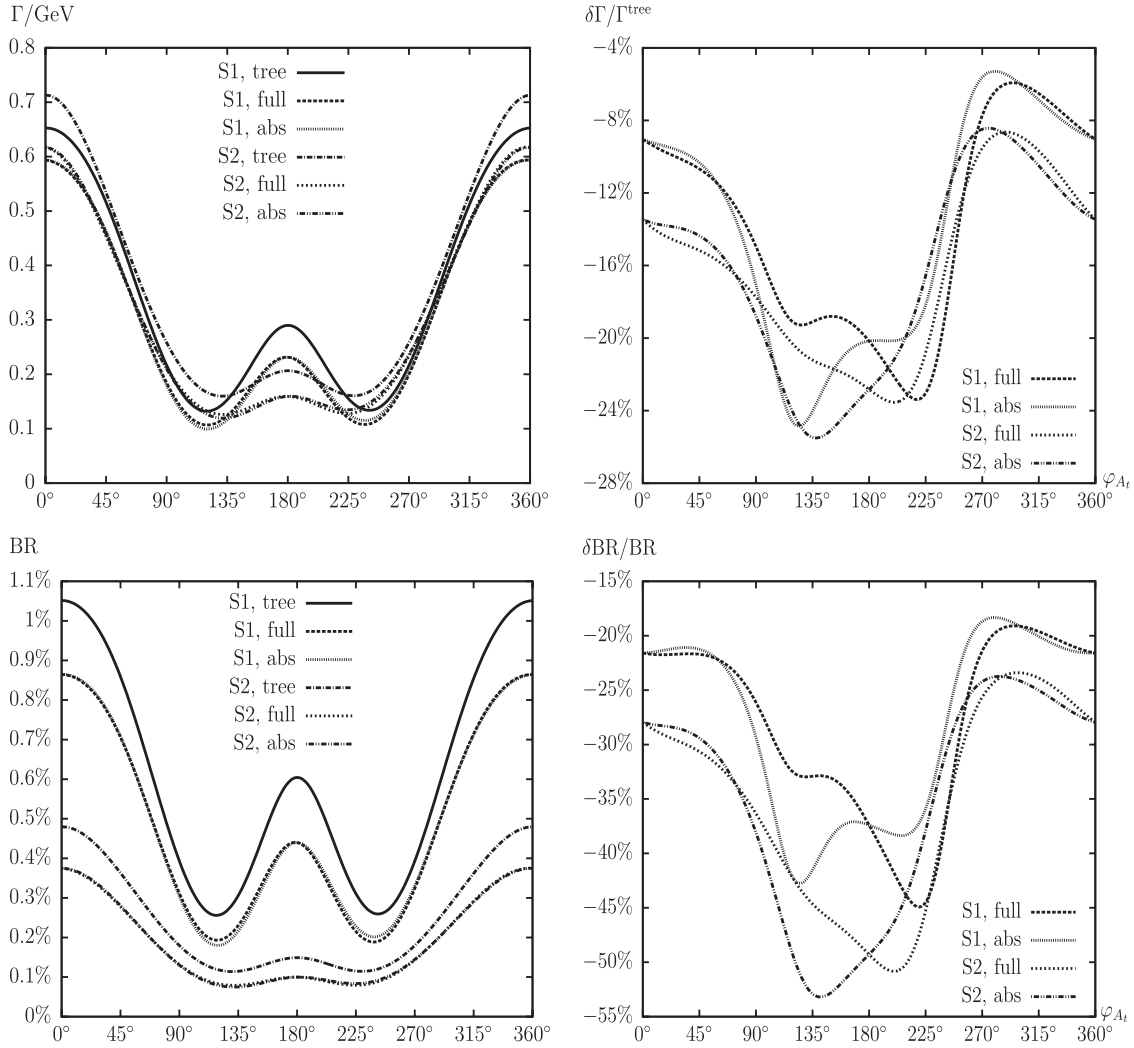


FIG. 24. $\Gamma(\tilde{t}_2 \rightarrow \tilde{t}_1 h_2)$. Tree-level (tree) and full one-loop (full) corrected partial decay widths are shown. Also shown are the full one-loop corrected partial decay widths including absorptive contributions (abs). The parameters are chosen according to S1 and S2 (see Table I), with φ_{A_t} varied. The upper left plot shows the partial decay width, the upper right plot the corresponding relative size of the corrections. The lower left plot shows the BR, the lower right plot the relative correction of the BR.

threshold relative corrections of $\sim +10\%$, -20% , -5% are found for h_1 , h_2 , h_3 , respectively. In (all) the plots the value of $m_{\tilde{t}_2}$ for which $m_{\tilde{t}_1} + m_{\tilde{t}_2} = 1000$ GeV is shown as a vertical line, i.e. the region where the heavier stop can be produced at the ILC(1000). In these regions the size of the corrections amounts up to $\sim +20\%$, -10% , $+10\%$ for the three neutral Higgs bosons. The BRs are at the few percent level for all three channels for the two numerical scenarios. The relative change in the BRs for the masses accessible at the ILC(1000) are about $+8\%$, -21% , -1% for h_1 , h_2 , h_3 , respectively. For larger masses, only accessible at the LHC, the one-loop corrections are around $+10\%$, -25% , and -5% . Depending on the MSSM parameters (and the channels kinematically allowed) the one-loop contributions presented here can be relevant for analyses at the ILC as well as at the LHC.

Next, in Fig. 11 we show results for the decay $\Gamma(\tilde{t}_2 \rightarrow \tilde{t}_1 Z)$. The dips due to the thresholds in $[\delta Z_{\tilde{t}}]_{11,21}$, δY_t , and $\delta m_{\tilde{t}_1}^2$ are the same as before. The relative corrections to the partial decay width in S1 range between $+8\%$ at low $m_{\tilde{t}_2}$, i.e. in the “ILC(1000) regime,” to -5% at large $m_{\tilde{t}_2}$, with the exception of the region close to thresholds. Within S2 the relative corrections stay below $\sim 5\%$. The $\text{BR}(\tilde{t}_2 \rightarrow \tilde{t}_1 Z)$ is larger than 15% for the smallest $m_{\tilde{t}_2}$ values in the two scenarios. This drops below 3% for $m_{\tilde{t}_2} \gtrsim 2.5$ TeV. The relative change for masses accessible at the ILC(1000) is found at the few percent level.

The results for the decay $\tilde{t}_2 \rightarrow t \tilde{g}$ are presented in Fig. 12. We see that for the relative corrections of the partial decay width up to 48% (22%) are reached for $m_{\tilde{t}_2} = 570(980)$ GeV in S1 (S2), i.e. at the smallest

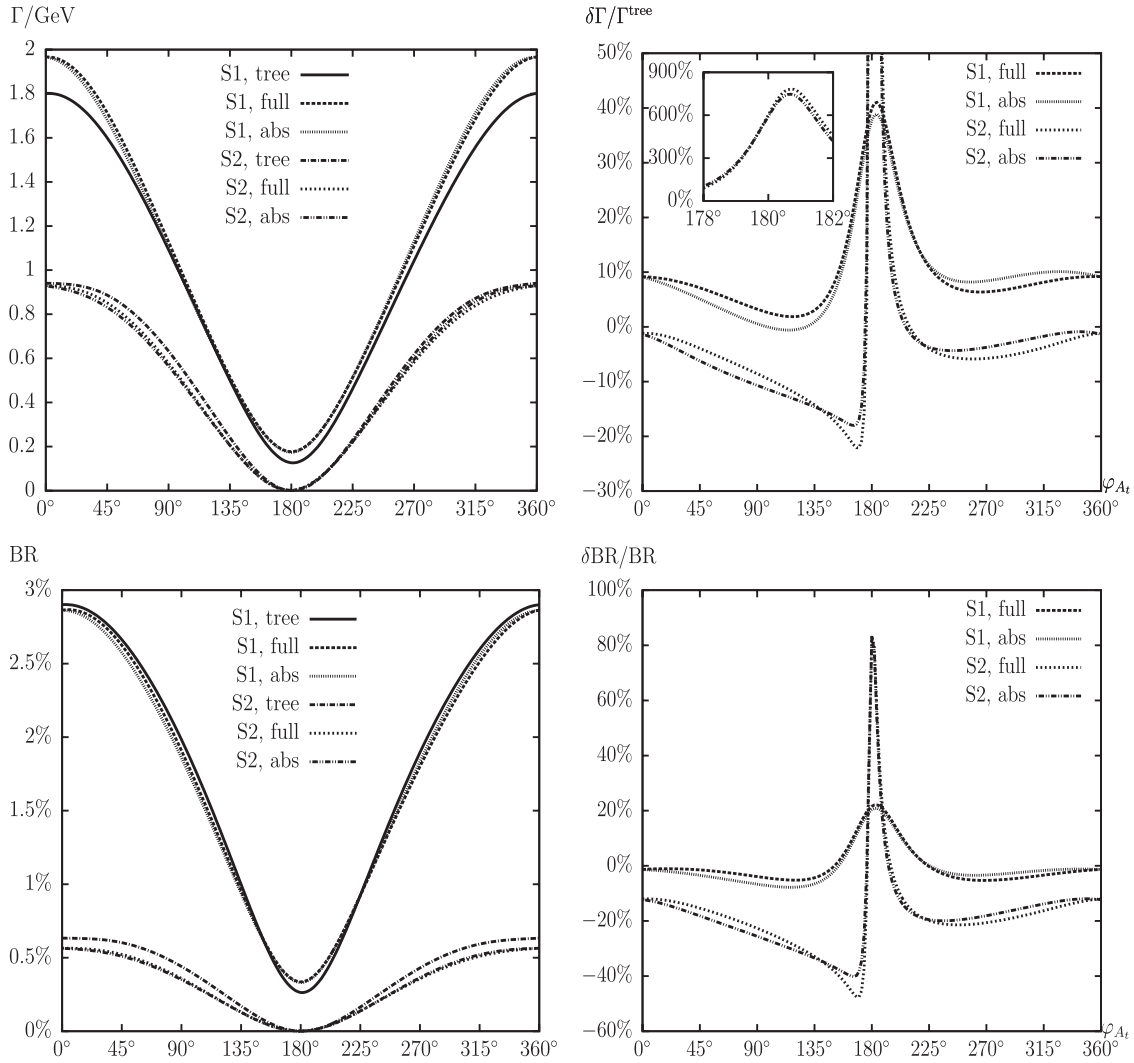


FIG. 25. $\Gamma(\tilde{\tau}_2 \rightarrow \tilde{\tau}_1 h_3)$. Tree-level (tree) and full one-loop (full) corrected partial decay widths are shown. Also shown are the full one-loop corrected partial decay widths including absorptive contributions (abs). The parameters are chosen according to S1 and S2 (see Table I), with φ_{A_t} varied. The upper left plot shows the partial decay width, the upper right plot the corresponding relative size of the corrections. The lower left plot shows the BR, the lower right plot the relative correction of the BR.

possible value and decrease for increasing $m_{\tilde{\tau}_2}$. It should be noted that in this case the hard and soft QCD radiation can be very large and the two compensate each other. The BR turns out to be very large and growing with $m_{\tilde{\tau}_2}$, where values larger than 50% are found. Within S1 the relative corrections can reach up to +20% in the production threshold region and are larger than +12% in the parameter space accessible at the ILC(1000). For large $m_{\tilde{\tau}_2}$ the corrections range between +11% and +15% in the two scenarios.

Now we turn to the decays $\tilde{\tau}_2 \rightarrow t\tilde{\chi}_k^0$ ($k = 1, 2, 3, 4$), with the results shown in Figs. 13–16. Since μ , M_1 , and M_2 are roughly of the same order, the four states are a mixture of gauginos and Higgsinos. Consequently, the partial decay widths are found to be roughly the same. The larger partial

decay widths for the decay modes $\tilde{\tau}_2 \rightarrow t\tilde{\chi}_k^0$ with $k = 1, 2$ ($k = 3, 4$) are found in S1 (S2) and are ~ 15 – 25 GeV. For S1 we find relative one-loop corrections ranging between 0% and $\sim -30\%$ for $\Gamma(\tilde{\tau}_2 \rightarrow t\tilde{\chi}_1^0)$ and $\Gamma(\tilde{\tau}_2 \rightarrow t\tilde{\chi}_2^0)$, where the smaller values are reached for small $m_{\tilde{\tau}_2}$. $\Gamma(\tilde{\tau}_2 \rightarrow t\tilde{\chi}_3^0)$ receives one-loop contributions between +8% and -16% , while for $\Gamma(\tilde{\tau}_2 \rightarrow t\tilde{\chi}_4^0)$ we find -18% to -35% with the exception of very small $m_{\tilde{\tau}_2}$, where the partial decay width itself is negligible. Within S2 the corrections stay at the few percent level for $\Gamma(\tilde{\tau}_2 \rightarrow t\tilde{\chi}_1^0)$, while for $\Gamma(\tilde{\tau}_2 \rightarrow t\tilde{\chi}_2^0)$, $\Gamma(\tilde{\tau}_2 \rightarrow t\tilde{\chi}_3^0)$, and $\Gamma(\tilde{\tau}_2 \rightarrow t\tilde{\chi}_4^0)$ they range between -10% and -30% . Following the size of the partial decay widths, also the branching ratios are roughly the same for the four decay modes. The relative changes in the BRs for $m_{\tilde{\tau}_2} + m_{\tilde{\tau}_1} \lesssim 1000$ GeV are $\sim -15\%$, -18% , -6% , and -30%

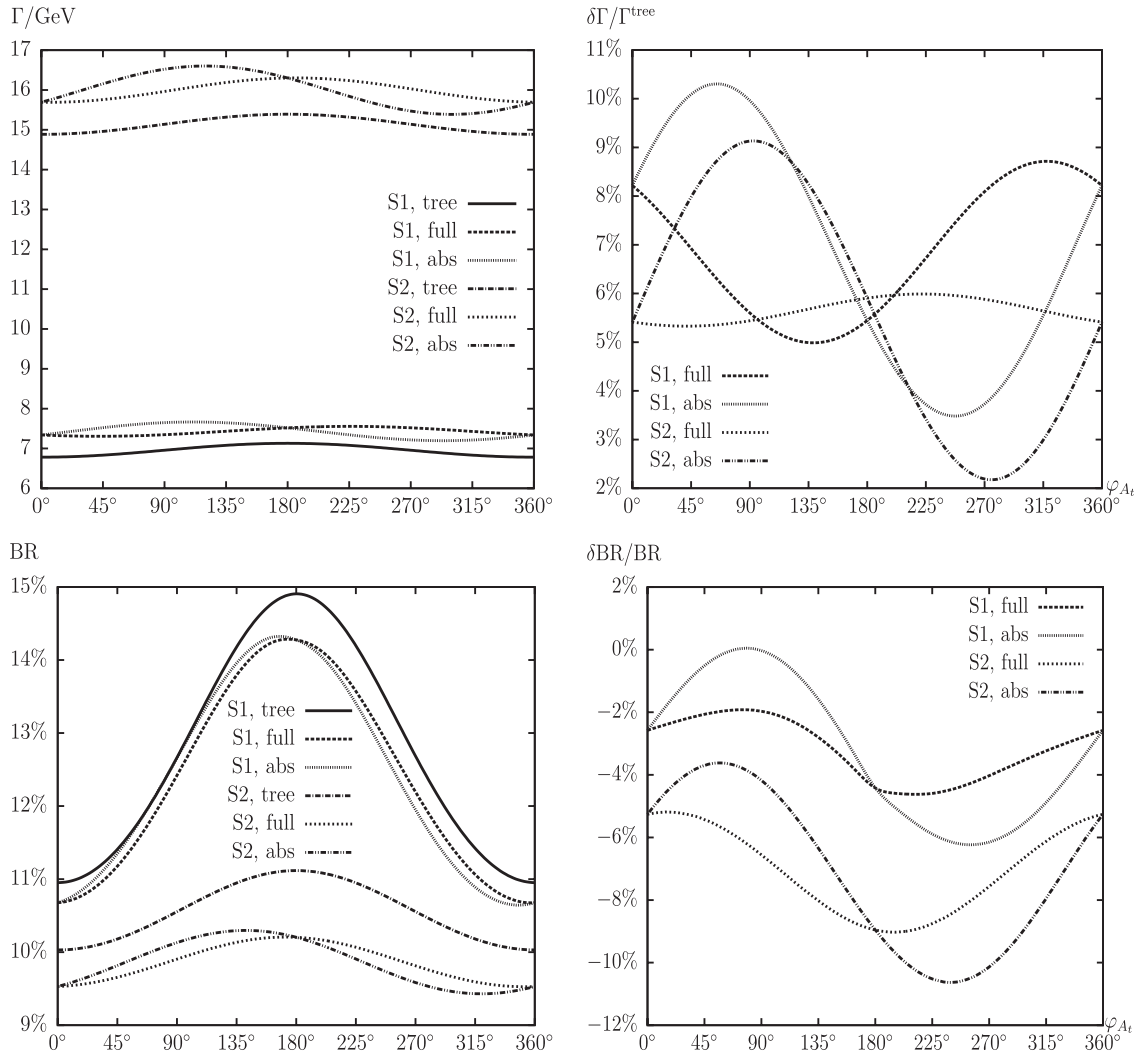


FIG. 26. $\Gamma(\tilde{t}_2 \rightarrow \tilde{t}_1 Z)$. Tree-level (tree) and full one-loop (full) corrected partial decay widths are shown. Also shown are the full one-loop corrected partial decay widths including absorptive contributions (abs). The parameters are chosen according to S1 and S2 (see Table I), with φ_{A_1} varied. The upper left plot shows the partial decay width, the upper right plot the corresponding relative size of the corrections. The lower left plot shows the BR, the lower right plot the relative correction of the BR.

for $k = 1, 2, 3, 4$, respectively. Especially, for this parameter range, for the decays to the two lighter neutralinos the branching ratios are $\sim 5\%$ and $\sim 10\%$, i.e. the one-loop corrections can be crucial to match the anticipated ILC precision.

Next in Figs. 17 and 18 we present the results for $\tilde{t}_2 \rightarrow b\tilde{\chi}_j^+$ ($j = 1, 2$). The size of the partial decay widths and branching ratios for $\tilde{t}_2 \rightarrow b\tilde{\chi}_1^+$ ($\tilde{t}_2 \rightarrow b\tilde{\chi}_2^+$) are roughly the same as for $\tilde{t}_2 \rightarrow t\tilde{\chi}_k^0$ with $k = 1, 2$ ($k = 3, 4$). For $\Gamma(\tilde{t}_2 \rightarrow b\tilde{\chi}_1^+)$ we find relative corrections starting at -5% at low $m_{\tilde{t}_2}$ in S1 down to $\sim -35\%$ at high $m_{\tilde{t}_2}$ in both scenarios. The partial decay width $\Gamma(\tilde{t}_2 \rightarrow b\tilde{\chi}_2^+)$ is very small in S1 for $m_{\tilde{t}_1} + m_{\tilde{t}_2} < 1000$ GeV. Because of this smallness, and additionally pronounced due to the vicinity of the production threshold, the relative size of the

corrections becomes huge and is not reliable anymore. For higher $m_{\tilde{t}_2}$ values we find relative corrections between -20% (-10%) to -30% in S1 (S2). A large branching ratio of $\sim 14\%$ in the ILC(1000) accessible regime is reached in S1 in the decay $\tilde{t}_2 \rightarrow b\tilde{\chi}_1^+$, where the one-loop corrections are $\sim -20\%$. Again the one-loop corrections can be crucial to match the ILC precision.

We now turn to the decay modes $\tilde{t}_2 \rightarrow \tilde{b}_i H^+$ ($i = 1, 2$). Results are shown in Figs. 19 and 20, (which have been used for the investigations in Ref. [38]). In Fig. 19 several peaks and dips can be observed. Within S1 the first (fourth) peak at $m_{\tilde{t}_2} \approx 571(638)$ GeV stems from the threshold $m_{\tilde{t}_1} + M_{H^\pm}(M_W) = m_{\tilde{b}_1}$ in the self-energies $\Sigma_{\tilde{b}_{1,2}}(m_{\tilde{b}_1}^2)$ entering the renormalization constants $[\delta Z_{\tilde{b}}]_{1,2}$. The second dip at $m_{\tilde{t}_2} \approx 596$ GeV comes from the threshold

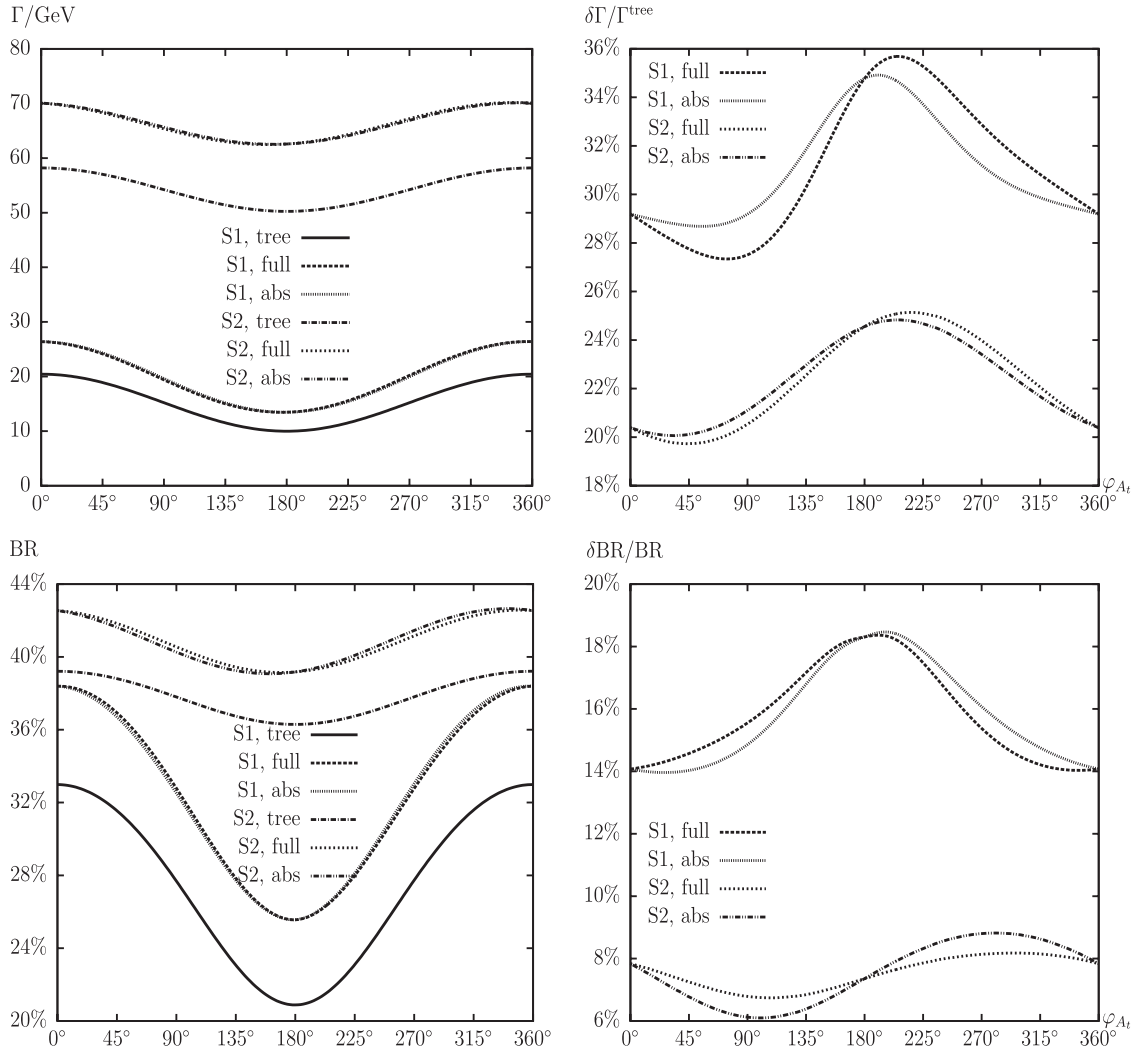


FIG. 27. $\Gamma(\tilde{t}_2 \rightarrow t\tilde{g})$. Tree-level (tree) and full one-loop (full) corrected partial decay widths are shown. Also shown are the full one-loop corrected partial decay widths including absorptive contributions (abs). The parameters are chosen according to S1 and S2 (see Table I), with φ_{A_t} varied. The upper left plot shows the partial decay width, the upper right plot the corresponding relative size of the corrections. The lower left plot shows the BR, the lower right plot the relative correction of the BR.

$m_{\tilde{g}} + m_b = m_{\tilde{b}_1}$. The third and the fifth dip come from the same threshold²⁶ $m_t + m_{\tilde{\chi}_1^\pm} = m_{\tilde{b}_1}$ at $m_{\tilde{t}_2} \approx 601, 823$ GeV, respectively.²⁷ The sixth dip at $m_{\tilde{t}_2} \approx 1282$ GeV comes from the threshold $m_t + m_{\tilde{\chi}_2^\pm} = m_{\tilde{b}_1}$. Within S2 the peak/dip at $m_{\tilde{t}_2} \approx 1130$ GeV is the threshold $m_{\tilde{t}_1} + M_W = m_{\tilde{b}_1}$. The other peaks/dips do not appear as the values for the stop masses are different. Also in Fig. 20 some peaks/dips appear. Within S1 the first peak/dip is visible at $m_{\tilde{t}_2} \approx 571$ GeV, due to the threshold $m_{\tilde{t}_1} + M_{H^\pm} = m_{\tilde{b}_1}$ (in the self-energy $\Sigma_{\tilde{b}_{21}}(m_{\tilde{b}_1}^2)$ entering the renormalization constant $[\delta\mathbf{Z}_{\tilde{b}_{21}}]_{21}$). Within S2 the “apparently single” dip is

²⁶It should be remembered that $m_{\tilde{b}_1}$ changes its value when the value of $m_{\tilde{t}_2}$ is changed.

²⁷For these two different input parameters ($m_{\tilde{t}_2} \approx 601, 823$ GeV) we get coincidentally $m_{\tilde{b}_1} \approx 349.14$ GeV.

in reality two dips at $m_{\tilde{t}_2} \approx 1163(1164)$ GeV coming from the thresholds $m_{\tilde{b}_1} + m_A(m_H) = m_{\tilde{b}_2}$ (it should be noted that the internal Higgs boson masses are tree-level masses).

The absolute value of the partial decay widths is relatively small, staying below $\sim 1.2(0.2)$ GeV for $\Gamma(\tilde{t}_2 \rightarrow \tilde{b}_1 H^+)$ [$\Gamma(\tilde{t}_2 \rightarrow \tilde{b}_2 H^+)$]. The relative size of the one-loop corrections to $\Gamma(\tilde{t}_2 \rightarrow \tilde{b}_1 H^+)$ ranges between $\sim -12\%$ and -27% (-20%) in S1 (S2). For $\Gamma(\tilde{t}_2 \rightarrow \tilde{b}_2 H^+)$ very large corrections are found for the smallest $m_{\tilde{t}_2}$ values, dropping to values close to zero for larger masses. Because of the small partial decay widths, also the branching ratios are at or below the 1% level. Only if other channels were kinematically suppressed, these decays could play a relevant role, and the one-loop effects could be expected at the level of one-loop contributions to the partial decay widths itself.

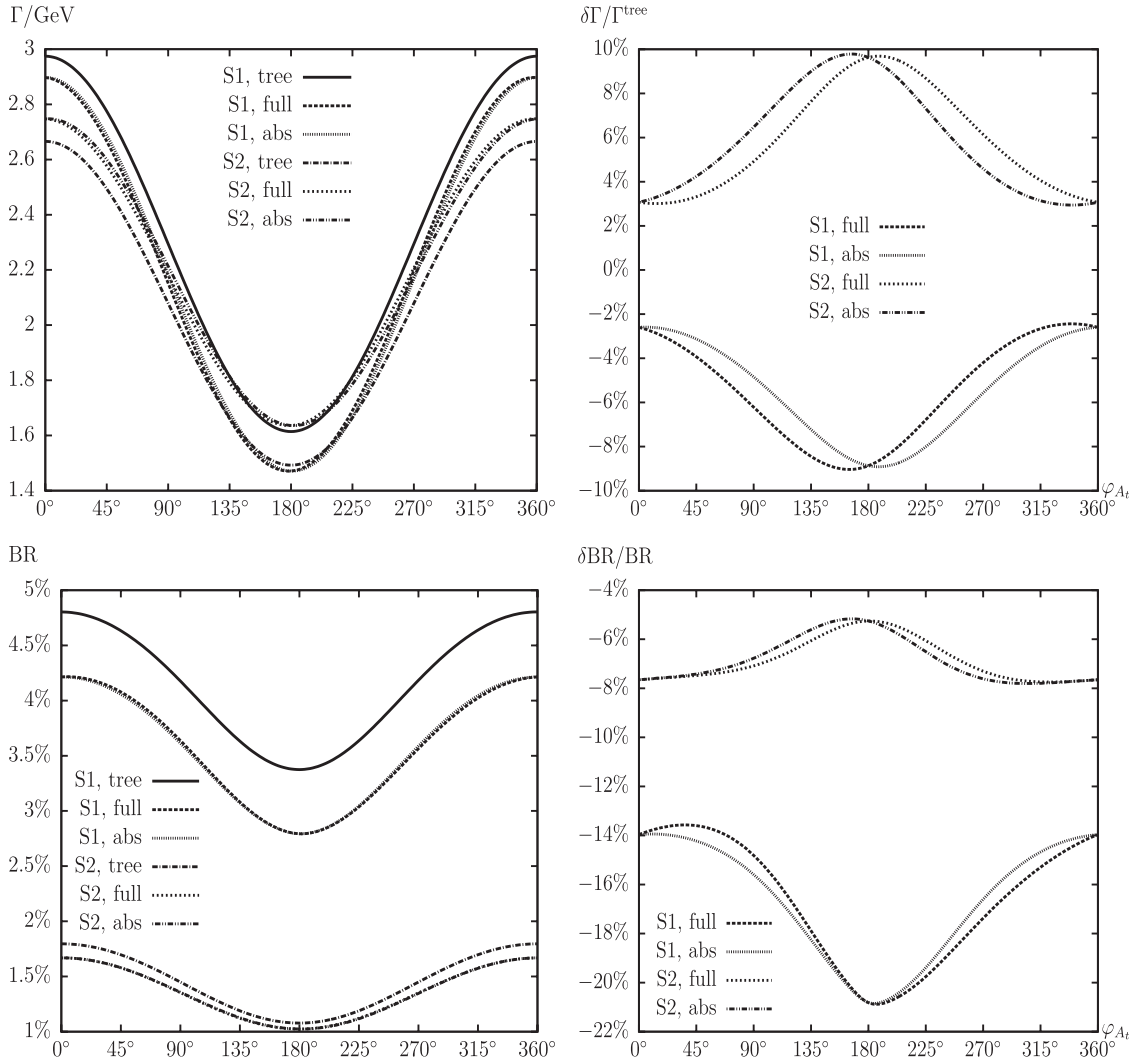


FIG. 28. $\Gamma(\tilde{t}_2 \rightarrow t\tilde{\chi}_1^0)$. Tree-level (tree) and full one-loop (full) corrected partial decay widths are shown. Also shown are the full one-loop corrected partial decay widths including absorptive contributions (abs). The parameters are chosen according to S1 and S2 (see Table I), with φ_{A_t} varied. The upper left plot shows the partial decay width, the upper right plot the corresponding relative size of the corrections. The lower left plot shows the BR, the lower right plot the relative correction of the BR.

Results for the other decay modes involving scalar top and bottom quarks, $\tilde{t}_2 \rightarrow \tilde{b}_i W^+$ ($i = 1, 2$), are shown in Figs. 21 and 22. Also these decay modes have been analyzed in detail in Ref. [38]. The peaks/dips are the same ones as for the decays $\tilde{t}_2 \rightarrow \tilde{b}_i H^+$. On top of that due to different renormalization constants entering the calculation one observes the following: within S1 peaks appear at $m_{\tilde{t}_2} \approx 618(656, 657)$ GeV due to $m_{\tilde{b}_1} + M_Z(m_{A_t}, m_H) = m_{\tilde{b}_2}$, and at $m_{\tilde{t}_2} \approx 721$ GeV due to $m_t + m_{\tilde{\chi}_2^\pm} = m_{\tilde{t}_2}$. The “knee” at $m_{\tilde{t}_2} \approx 1303$ GeV results from $m_t + m_{\tilde{g}} = m_{\tilde{t}_1}$ in $\Sigma_{\tilde{t}_2}(m_{\tilde{t}_1}^2)$ entering the renormalization constant δY_t . Within S2 one hardly visible dip can be found at $m_{\tilde{t}_2} \approx 1039$ GeV from $m_{\tilde{b}_1} + M_Z = m_{\tilde{b}_2}$. The knee at $m_{\tilde{t}_2} \approx 1163(1164)$ GeV is the same one as in Fig. 20. The absolute size of

$\Gamma(\tilde{t}_2 \rightarrow \tilde{b}_1 W^+)$ is found to be between ~ 5 GeV and ~ 25 GeV, depending on $m_{\tilde{t}_2}$ and the scenario. $\Gamma(\tilde{t}_2 \rightarrow \tilde{b}_2 W^+)$, on the other hand, is found to be tiny for nearly all $m_{\tilde{t}_2}$ values. However, the smallness of $\Gamma(\tilde{t}_2 \rightarrow \tilde{b}_2 W^+)$ is a purely coincidental effect. A slightly smaller $m_{\tilde{b}_2}$ would yield a width of $\mathcal{O}(0.1)$ GeV. The relative corrections to $\Gamma(\tilde{t}_2 \rightarrow \tilde{b}_1 W^+)$ range between $+10\%$ ($+15\%$) and -5% (0%) for S1 (S2). For $\Gamma(\tilde{t}_2 \rightarrow \tilde{b}_2 W^+)$ we find corrections of $\sim -10\%$ (-30%) to $+18\%$ ($+3\%$) in S1 (S2), where it has to be kept in mind that the partial decay width itself is tiny in our scenarios S1 and S2. The branching ratio for $\tilde{t}_2 \rightarrow \tilde{b}_1 W^+$ can reach up to $\sim 18\%$ in the parameter range with $m_{\tilde{t}_2} + m_{\tilde{t}_1} \lesssim 1000$ GeV. Here the relative one-loop effect on the BR is $\sim -5\%$ and could be important to reach the ILC precision.

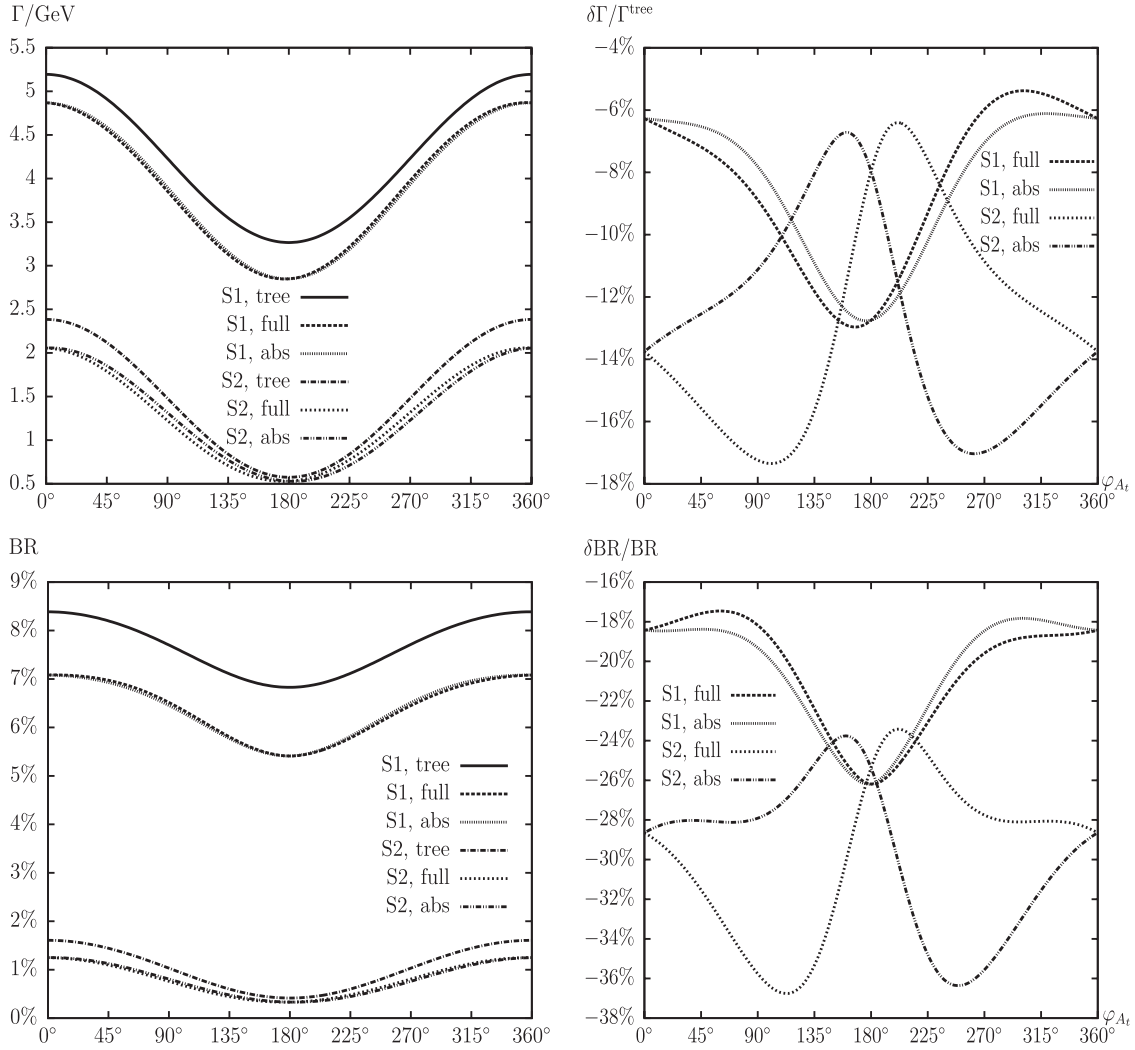


FIG. 29. $\Gamma(\tilde{t}_2 \rightarrow t\tilde{\chi}_2^0)$. Tree-level (tree) and full one-loop (full) corrected partial decay widths are shown. Also shown are the full one-loop corrected partial decay widths including absorptive contributions (abs). The parameters are chosen according to S1 and S2 (see Table I), with φ_{A_t} varied. The upper left plot shows the partial decay width, the upper right plot the corresponding relative size of the corrections. The lower left plot shows the BR, the lower right plot the relative correction of the BR.

C. Full one-loop results for varying φ_{A_t}

In this subsection we analyze the various partial decay widths²⁸ and branching ratios as a function of φ_{A_t} . The other parameters are chosen according to Table I. Thus, within S1 we have $m_{\tilde{t}_1} + m_{\tilde{t}_2} = 910$ GeV, i.e. the production channel $e^+e^- \rightarrow \tilde{t}_1^\dagger\tilde{t}_2$ is open at the ILC(1000). Consequently, the accuracy of the prediction of the various partial decay widths and branching ratios should be at the same level (or better) as the anticipated ILC precision. It should be noted that the tree-level prediction depends on φ_{A_t} via the stop mixing matrix.

²⁸Again we note, that we do not investigate the decays of \tilde{t}_2^\dagger here, which would correspond to an analysis of \mathcal{CP} asymmetries, which is beyond the scope of this paper.

When performing an analysis involving complex parameters it should be noted that the results for physical observables are affected only by certain combinations of the complex phases of the parameters μ , the trilinear couplings A_t, A_b, \dots , and the gaugino mass parameters M_1, M_2, M_3 [53,82]. It is possible, for instance, to rotate the phase φ_{M_2} away. Experimental constraints on the (combinations of) complex phases arise, in particular, from their contributions to electric dipole moments of the electron and the neutron (see Refs. [83,84] and references therein), of the deuteron [85] and of heavy quarks [86]. While SM contributions enter only at the three-loop level, due to its complex phases the MSSM can contribute already at one-loop order. Large phases in the first two generations of sfermions can only be accommodated if these generations are assumed to be very heavy [87] or

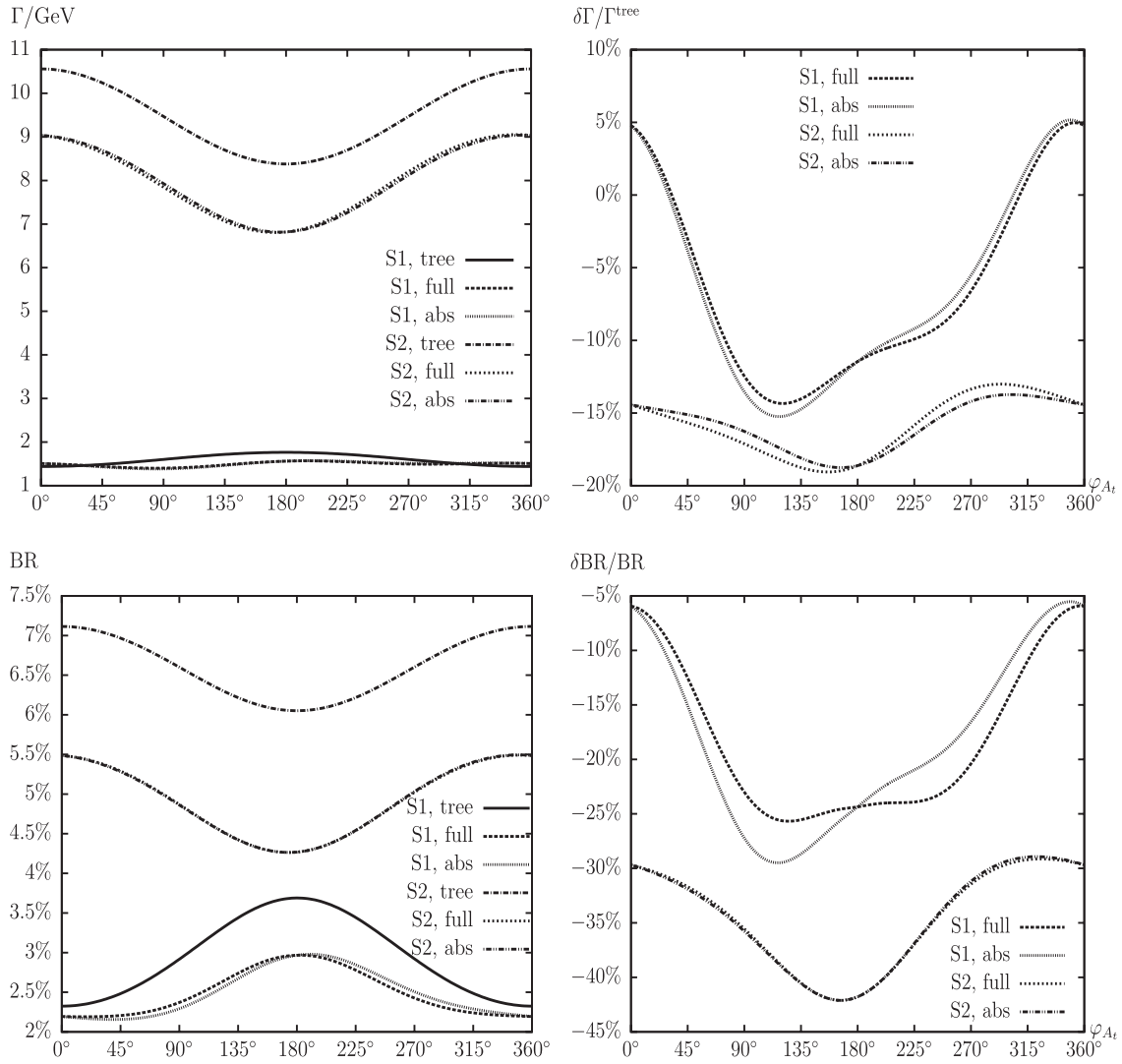


FIG. 30. $\Gamma(\tilde{t}_2 \rightarrow t\tilde{\chi}_3^0)$. Tree-level (tree) and full one-loop (full) corrected partial decay widths are shown. Also shown are the full one-loop corrected partial decay widths including absorptive contributions (abs). The parameters are chosen according to S1 and S2 (see Table I), with φ_{A_t} varied. The upper left plot shows the partial decay width, the upper right plot the corresponding relative size of the corrections. The lower left plot shows the BR, the lower right plot the relative correction of the BR.

large cancellations occur [88]; see, however, the discussion in Ref. [89]. A recent review can be found in Ref. [90]. Accordingly (using the convention that $\varphi_{M_2} = 0$, as done in this paper), in particular, the phase φ_μ is tightly constrained [91], while the bounds on the phases of the third generation trilinear couplings are much weaker. The phases of μ , A_t , and A_b enter only in the combinations ($\varphi_{A_{t,b}} + \varphi_\mu$) (or in different combinations together with phases of M_1 or M_3). Setting $\varphi_\mu = 0$ (see above) as well as $\varphi_{M_1} = \varphi_{\tilde{g}} = 0$ (we do not consider these phases in this paper) leaves us with φ_{A_t} and φ_{A_b} as the only complex valued parameters. The dependence on φ_{A_b} on the partial decay widths involving scalar bottom quarks has been analyzed in detail in Ref. [38]. Consequently, we focus on a complex A_t and keep A_b real.

Since now a complex A_t can appear in the couplings, contributions from absorptive parts of self-energy type corrections on external legs can arise, and their impact will be discussed.²⁹ The corresponding formulas for an inclusion of these absorptive contributions via finite wave function correction factors can be found in the Appendix.

As before we start with the decays to Higgs bosons, $\tilde{t}_2 \rightarrow \tilde{t}_1 h_n$ ($n = 1, 2, 3$) shown in Figs. 23–25. The arrangement of the panels is the same as in the previous subsection. In Fig. 23, where the partial decay width $\Gamma(\tilde{t}_2 \rightarrow \tilde{t}_1 h_1)$ is given as a function of φ_{A_t} , one can see that the size of the corrections to the partial decay width vary substantially

²⁹In a slight abuse of the language “full” still refers to corrections without absorptive contributions.

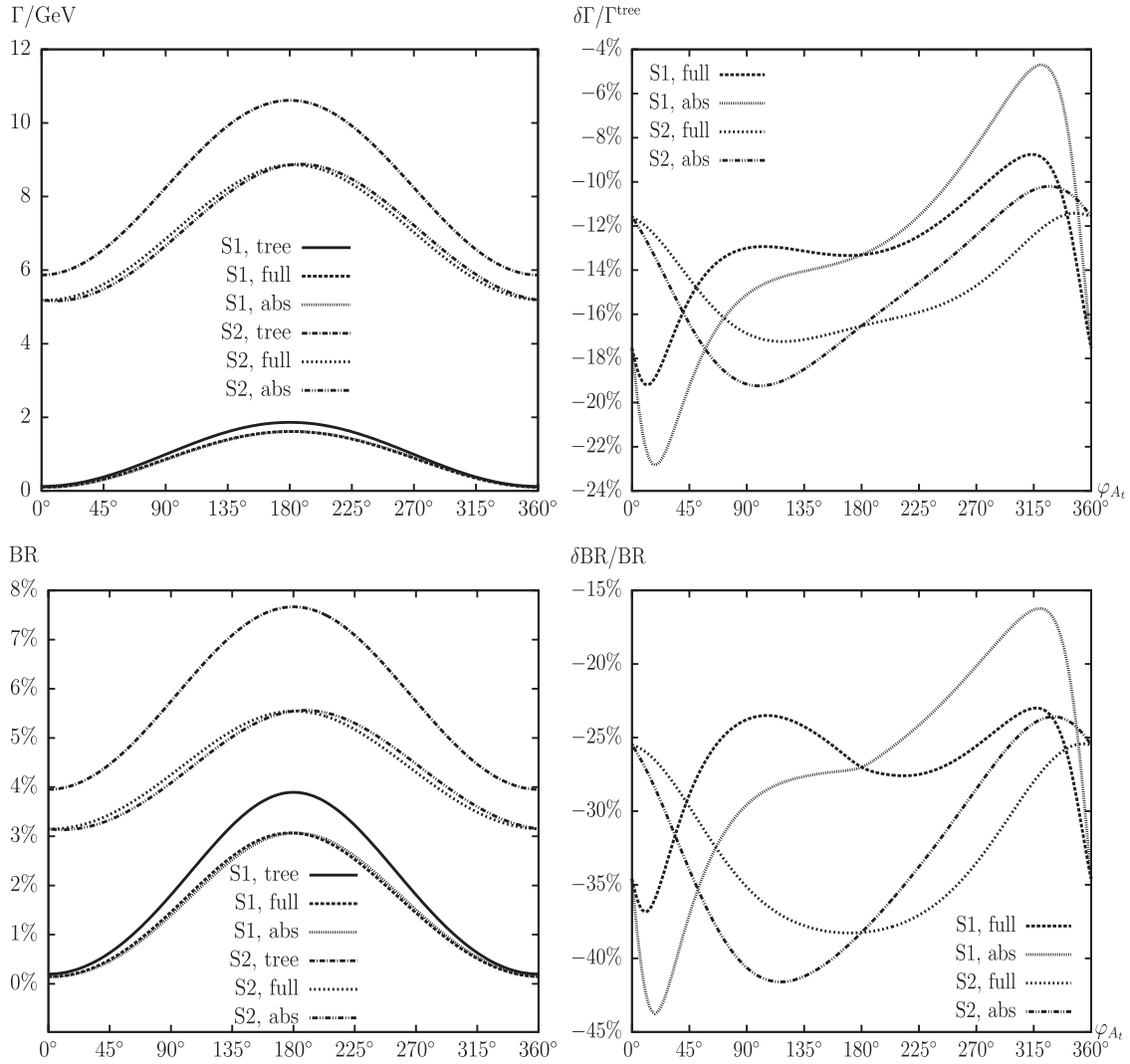


FIG. 31. $\Gamma(\tilde{t}_2 \rightarrow t \tilde{\chi}_4^0)$. Tree-level (tree) and full one-loop (full) corrected partial decay widths are shown. Also shown are the full one-loop corrected partial decay widths including absorptive contributions (abs). The parameters are chosen according to S1 and S2 (see Table I), with φ_{A_t} varied. The upper left plot shows the partial decay width, the upper right plot the corresponding relative size of the corrections. The lower left plot shows the BR, the lower right plot the relative correction of the BR.

with φ_{A_t} . The one-loop effects range from +21 (+16)% to +6 (+4)% in S1 (S2). The effect of the absorptive parts of self-energy type corrections on external legs (called “absorptive contributions” from now on) are at the few percent level. For $\varphi_{A_t} = 0, \pi, 2\pi$ these effects vanish (by construction).

It should be kept in mind that the parameters are chosen such that $e^+e^- \rightarrow \tilde{t}_1^+ \tilde{t}_2$ is kinematically possible at the ILC (1000) in S1, where the knowledge of such a large variation can be very important. Also for $\tilde{t}_2 \rightarrow \tilde{t}_1 h_2$, shown in Fig. 24, the variation with φ_{A_t} is very large, ranging from -6% to -24%, again with a non-negligible shift from the absorptive contributions. The wiggles in the size of the relative corrections to the partial decay width is a result of small numerical variations and not visible in the upper left

panel showing the full decay width. These variations are enhanced due to the smallness of the tree-level partial width; see Eq. (204). The results for $\tilde{t}_2 \rightarrow \tilde{t}_1 h_3$ can be found in Fig. 25. Also here the size of the corrections shows a large variation with φ_{A_t} , again with non-negligible absorptive contributions. Within S2 for real and negative A_t the partial width becomes extremely small at tree level, leading to (formally) very large relative one-loop corrections. The one-loop effects on the branching ratios also vary strongly with φ_{A_t} , following the same pattern as the partial decay widths. Effects up to $\pm 8\%$ are reached for $\text{BR}(\tilde{t}_2 \rightarrow \tilde{t}_1 h_1)$, while the other two decay modes reach large corrections only where the BRs are relatively small, $\lesssim 1\%$. The one-loop corrections to $\Gamma(\tilde{t}_2 \rightarrow \tilde{t}_1 h_1)$, however, can easily exceed the ILC precision.

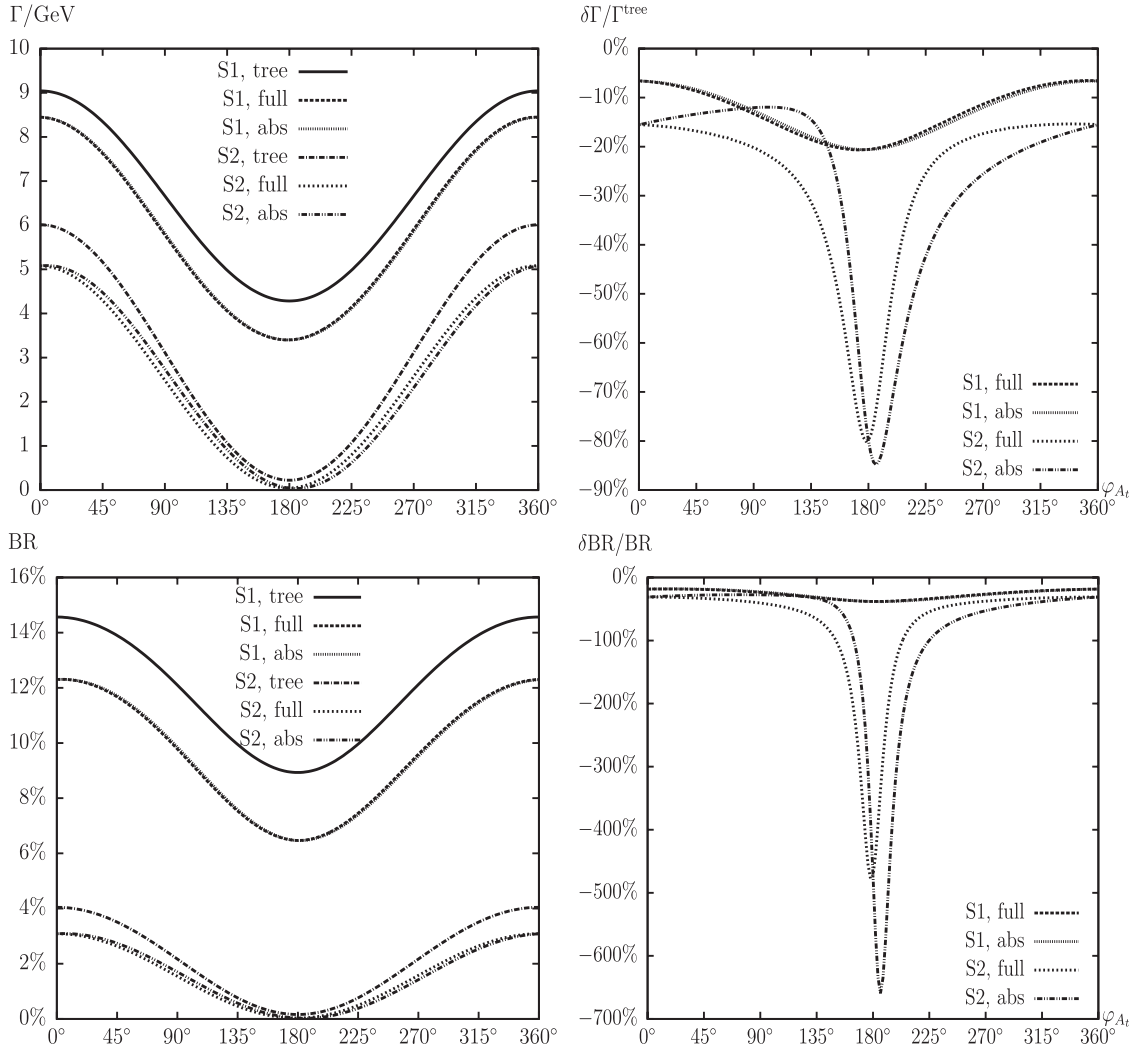


FIG. 32. $\Gamma(\tilde{t}_2 \rightarrow b \tilde{\chi}_1^+)$. Tree-level (tree) and full one-loop (full) corrected partial decay widths are shown. Also shown are the full one-loop corrected partial decay widths including absorptive contributions (abs). The parameters are chosen according to S1 and S2 (see Table I), with φ_{A_t} varied. The upper left plot shows the partial decay width, the upper right plot the corresponding relative size of the corrections. The lower left plot shows the BR, the lower right plot the relative correction of the BR.

In Fig. 26 we present the phase dependence for the decay mode $\tilde{t}_2 \rightarrow \tilde{t}_1 Z$. While in S1 the effect of the one-loop corrections to $\Gamma(\tilde{t}_2 \rightarrow \tilde{t}_1 Z)$ varies from $\sim +8\%$ to $\sim +5\%$, within S2 only a very small variation can be observed. These numbers change if the absorptive contributions are taken into account. In both scenarios substantially larger variations are found. Within S1 (S2) the branching ratio varies with φ_{A_t} between $\sim 11\%$ and $\sim 15\%$ (9.5% and 11%). Again the variation of the relative correction of the BR increases visibly via the inclusion of the absorptive contributions. The relative corrections reach -4% (-9%) and are relevant to match the ILC precision in S1.

Next we show the results for $\tilde{t}_2 \rightarrow t \tilde{g}$ in Fig. 27. In both numerical scenarios we find a substantial variation of the one-loop effects with φ_{A_t} . The effects range from $+28\%$

($+20\%$) to $+36\%$ ($+24\%$) in S1 (S2), where the effect of the absorptive contributions remains relatively small. The branching ratio varies strongly with φ_{A_t} in S1, ranging from $\sim 38\%$ to $\sim 25\%$, while in S2 it is larger and varies less, being around $\sim 41\%$. The one-loop corrections in S1 vary between $+14\%$ and $+18\%$ and are important for physics at the LHC and the ILC. Within S2 they are found to be $\sim 8\%$.

In Figs. 28–31 we present the variation of $\Gamma(\tilde{t}_2 \rightarrow t \tilde{\chi}_k^0)$ ($k = 1, 2, 3, 4$) as a function of φ_{A_t} . As for the variation with $m_{\tilde{t}_2}$ also here for $k = 1, 2$ ($k = 3, 4$) larger values of the partial decay width are found in S1 (S2) with a similar size as before. The one-loop effects on $\Gamma(\tilde{t}_2 \rightarrow t \tilde{\chi}_1^0)$ for $\varphi_{A_t} = 0$ are relatively small, at the $+3\%$ (-3%) level in S1 (S2). The variation of φ_{A_t} , however, now yields

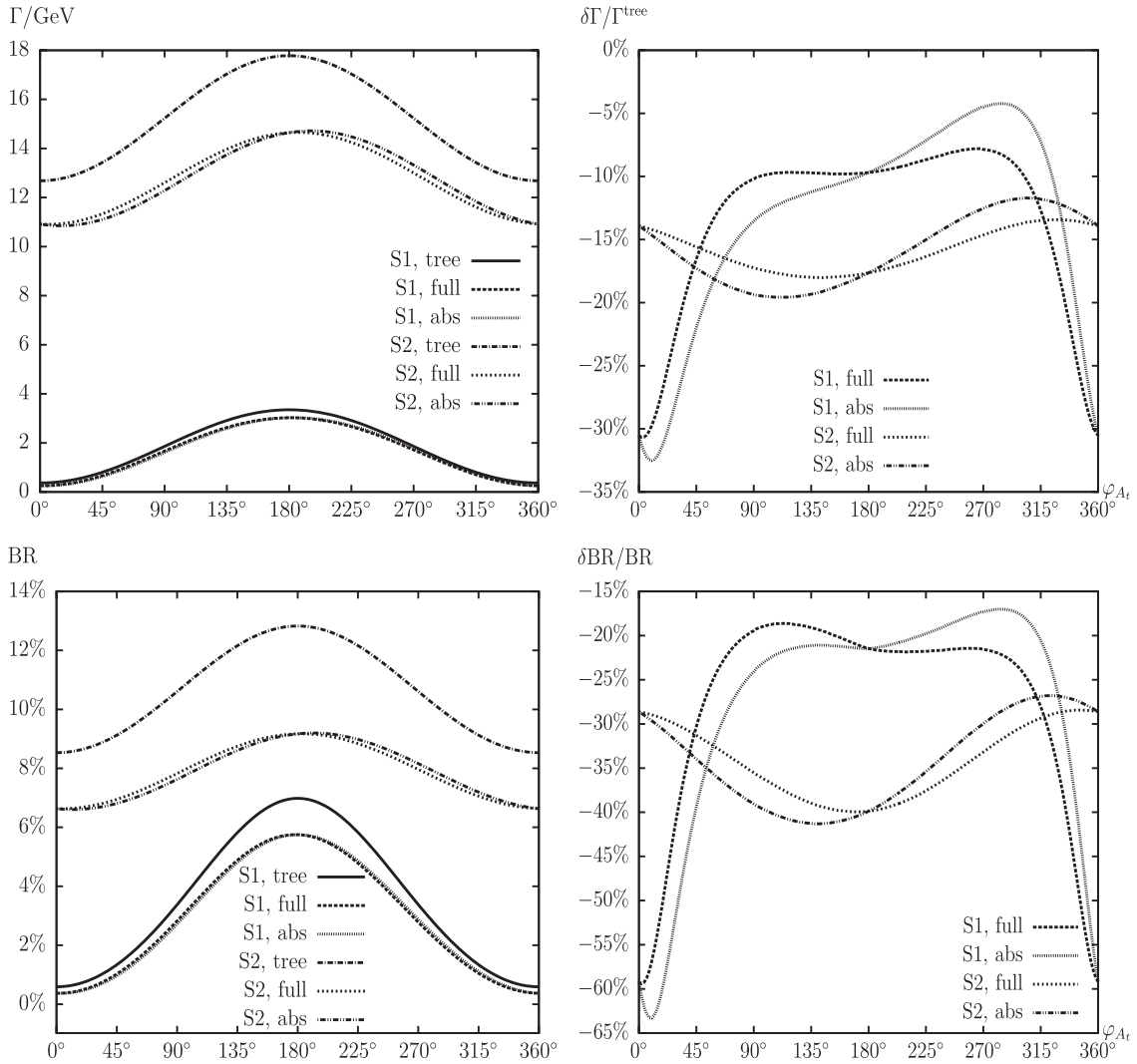


FIG. 33. $\Gamma(\tilde{t}_2 \rightarrow b\tilde{\chi}_2^+)$. Tree-level (tree) and full one-loop (full) corrected partial decay widths are shown. Also shown are the full one-loop corrected partial decay widths including absorptive contributions (abs). The parameters are chosen according to S1 and S2 (see Table I), with φ_{A_t} varied. The upper left plot shows the partial decay width, the upper right plot the corresponding relative size of the corrections. The lower left plot shows the BR, the lower right plot the relative correction of the BR.

one-loop corrections up to $\sim +10\%$ (-10%) in the two scenarios, with a small shift induced by the absorptive contributions. $\Gamma(\tilde{t}_2 \rightarrow t\tilde{\chi}_2^0)$ also exhibits a strong variation with φ_{A_t} , ranging from -12% (-18%) to -6% in S1 (S2). The absorptive contributions in this case can change the result strongly, leading especially in S2 to a substantially different shape. For $\Gamma(\tilde{t}_2 \rightarrow t\tilde{\chi}_3^0)$ the variation in S2 is small. Within S1, however, the effects for $\varphi_{A_t} = 0$ are at the $\sim +5\%$ level, while they reach nearly -15% for intermediate φ_{A_t} . The absorptive contributions are small. The last partial decay width of the four decay modes, $\Gamma(\tilde{t}_2 \rightarrow t\tilde{\chi}_4^0)$, shows a large variation at the one-loop level of nearly -20% in S1, where, however, the partial width itself is very small. For $\varphi_{A_t} \approx \pi$ a width of ~ 2 GeV is reached with a variation at the -10% level. Within S2

$\Gamma(\tilde{t}_2 \rightarrow t\tilde{\chi}_4^0)$ varies around ~ 7 GeV with a one-loop variation between -12% and -17% . The absorptive contributions lead to a result smaller by a few percent. Within S1, i.e. with the ILC(1000) accessible parameter space, the one-loop corrections reach -20% and more for $\text{BR}(\tilde{t}_2 \rightarrow t\tilde{\chi}_k^0)$, $k = 1, 2$, which can exceed the anticipated ILC precision. In general a strong variation of the one-loop effects with φ_{A_t} on the branching ratios is found, where very large corrections are found in S2 for $k = 3, 4$, where the one-loop contributions can change the BRs by up to -40% .

The results for $\Gamma(\tilde{t}_2 \rightarrow b\tilde{\chi}_j^+)$ ($j = 1, 2$) are shown in Figs. 32 and 33. For $\Gamma(\tilde{t}_2 \rightarrow b\tilde{\chi}_1^+)$ the decay width changes substantially with φ_{A_t} . The relative corrections are mostly between -5% and -20% , except in S2 for $\varphi_{A_t} \sim \pi$, where

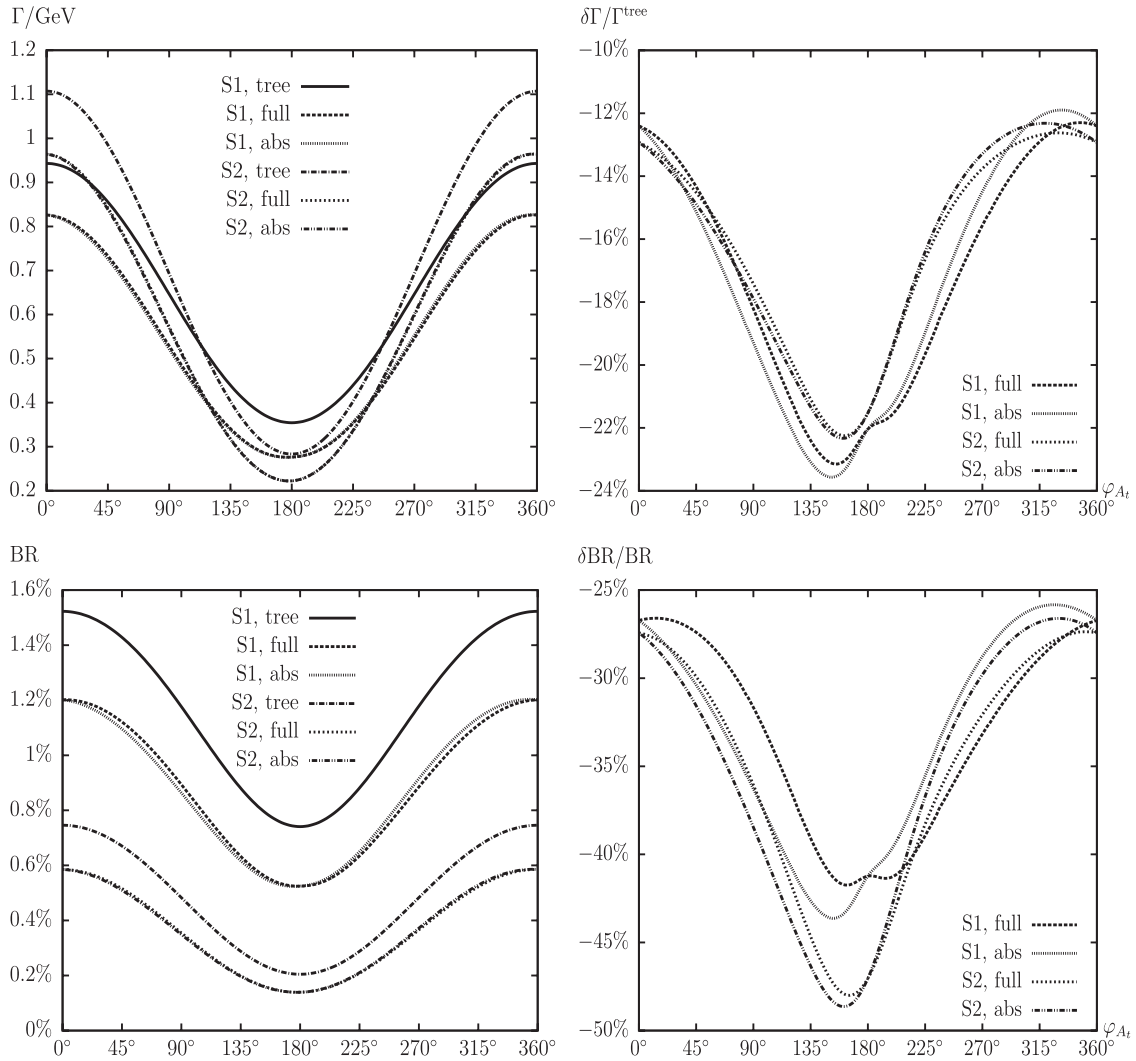


FIG. 34. $\Gamma(\tilde{t}_2 \rightarrow \tilde{b}_1 H^+)$. Tree-level (tree) and full one-loop (full) corrected partial decay widths are shown. Also shown are the full one-loop corrected partial decay widths including absorptive contributions (abs). The parameters are chosen according to S1 and S2 (see Table I), with φ_{A_i} varied. The upper left plot shows the partial decay width, the upper right plot the corresponding relative size of the corrections. The lower left plot shows the BR, the lower right plot the relative correction of the BR.

$\Gamma(\tilde{t}_2 \rightarrow b \tilde{\chi}_1^+)$ becomes very small. The absorptive contributions lead to a visible shift in the relative one-loop corrections in S2, where the largest effects are found again where $\Gamma(\tilde{t}_2 \rightarrow b \tilde{\chi}_1^+)$ is small. For $\Gamma(\tilde{t}_2 \rightarrow b \tilde{\chi}_2^+)$ we find a similar size of the corrections. Larger relative corrections of up to -32% are reached only in S1 where the decay width itself becomes very small. Within S1 the larger branching ratio values of 7% – 12% are found for $\tilde{t}_2 \rightarrow b \tilde{\chi}_1^+$. Here the relative corrections are between -18% and -30% , with some variation induced by the absorptive contributions, which can be relevant for the LHC and the ILC. For $\tilde{t}_2 \rightarrow b \tilde{\chi}_2^+$ the larger BR is found in S2, where values around 8% are found. The one-loop effects nearly reach -40% , which can be relevant for the LHC. Finally it should be noted that the apparently very large corrections on $\text{BR}(\tilde{t}_2 \rightarrow b \tilde{\chi}_1^+)$ in S2 (see the lower right plot in Fig. 32)

do not correspond to a negative BR. At $\varphi_{A_i} \sim \pi$ the loop corrections are negative and comparably to the (very small) tree-level width, leading to $\text{BR}^{\text{full}} \ll \text{BR}^{\text{tree}}$ in Eq. (208). The effect of these relatively large loop corrections around $\varphi_{A_i} \sim \pi$ can be sizably lowered by including higher-order corrections as, e.g., $|\mathcal{M}_{\text{loop}}|^2$.

Now we turn to the decay modes involving scalar bottom quarks, which have also been analyzed in Ref. [38]. In Figs. 34 and 35 the results for $\Gamma(\tilde{t}_2 \rightarrow \tilde{b}_i H^+)$ ($i = 1, 2$) are presented. While we find $\Gamma(\tilde{t}_2 \rightarrow \tilde{b}_1 H^+)$ at the ~ 1 GeV level, $\Gamma(\tilde{t}_2 \rightarrow \tilde{b}_2 H^+)$ is only around the 0.1 GeV level. The relative variation of $\Gamma(\tilde{t}_2 \rightarrow \tilde{b}_1 H^+)$ ranges from $\sim -13\%$ for large values of the width to $\sim -23\%$ for small values, with some variations induced by the absorptive contributions. For $\Gamma(\tilde{t}_2 \rightarrow \tilde{b}_2 H^+)$ in S1 the relative variation can

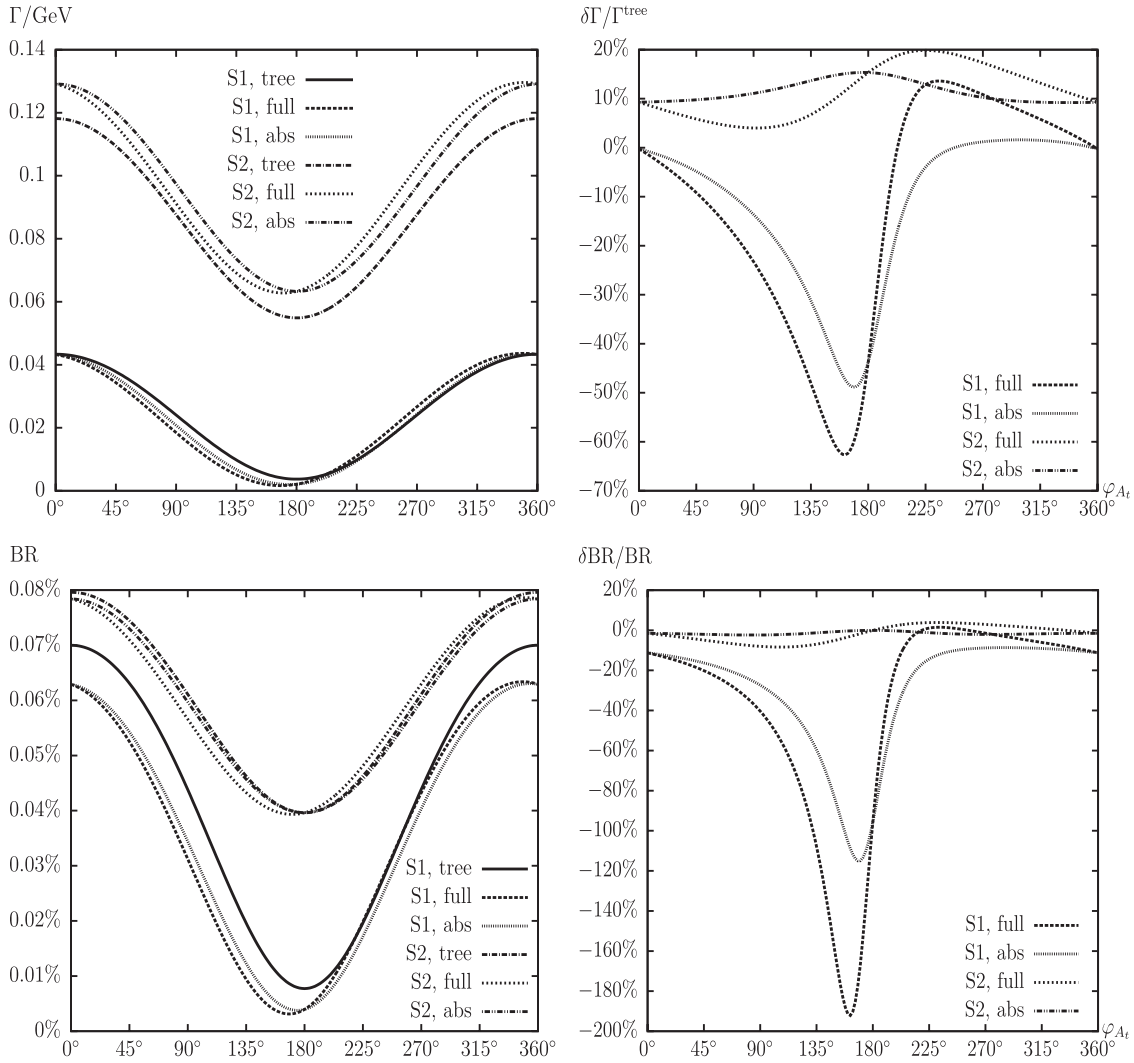


FIG. 35. $\Gamma(\tilde{t}_2 \rightarrow \tilde{b}_2 H^+)$. Tree-level (tree) and full one-loop (full) corrected partial decay widths are shown. Also shown are the full one-loop corrected partial decay widths including absorptive contributions (abs). The parameters are chosen according to S1 and S2 (see Table I), with φ_{A_t} varied. The upper left plot shows the partial decay width, the upper right plot the corresponding relative size of the corrections. The lower left plot shows the BR, the lower right plot the relative correction of the BR.

become very large, -60% (with a clearly visible shift from the absorptive contributions) but the partial decay width is negligibly small. Within S2, where $\Gamma(\tilde{t}_2 \rightarrow \tilde{b}_2 H^+) \sim 0.1$ GeV is realized the relative variation is at the 10% level. As for the variation with $m_{\tilde{t}_2}$ we find only small values for the branching ratios at the 1% (0.1%) level for the decay to the lighter (heavier) sbottom. The one-loop effects on the BRs are only important if other channels are kinematically suppressed. In this case the effects can be of the same order as for the partial decay widths itself. Again, the apparent very large effect on $\text{BR}(\tilde{t}_2 \rightarrow \tilde{b}_2 H^+)$ in S1 still corresponds to a positive BR; see Eq. (208).

The other decay modes involving scalar bottom quarks, $\tilde{t}_2 \rightarrow \tilde{b}_i W^+$ ($i = 1, 2$) are analyzed in Figs. 36 and 37. As in the analysis with $m_{\tilde{t}_2}$ varied, we find $\Gamma(\tilde{t}_2 \rightarrow \tilde{b}_1 W^+)$ at

the 11 (25) GeV level in S1 (S2). The relative correction without absorptive contributions changes sizably in S1, ranging between 0% and +12%. Taking into account the absorptive contributions this strongly reduces to 5% and 7%. Within S2 the corrections without absorptive contributions are around +5% for all φ_{A_t} , but the absorptive contributions have the opposite effect of strongly enhancing the variation. $\Gamma(\tilde{t}_2 \rightarrow \tilde{b}_2 W^+)$, again as in Sec. IV B, is very small and stays below ~ 0.03 GeV. The variation of this negligibly small partial decay width is found to be between -6% and $+6\%$; the shift from the absorptive contributions remains relatively small. Consequently, a relevant branching ratio is found only for $\tilde{t}_2 \rightarrow \tilde{b}_1 W^+$, where values around $\sim 20\%$ ($\sim 16\%$) are found in S1 (S2). The relative effects of the one-loop corrections can

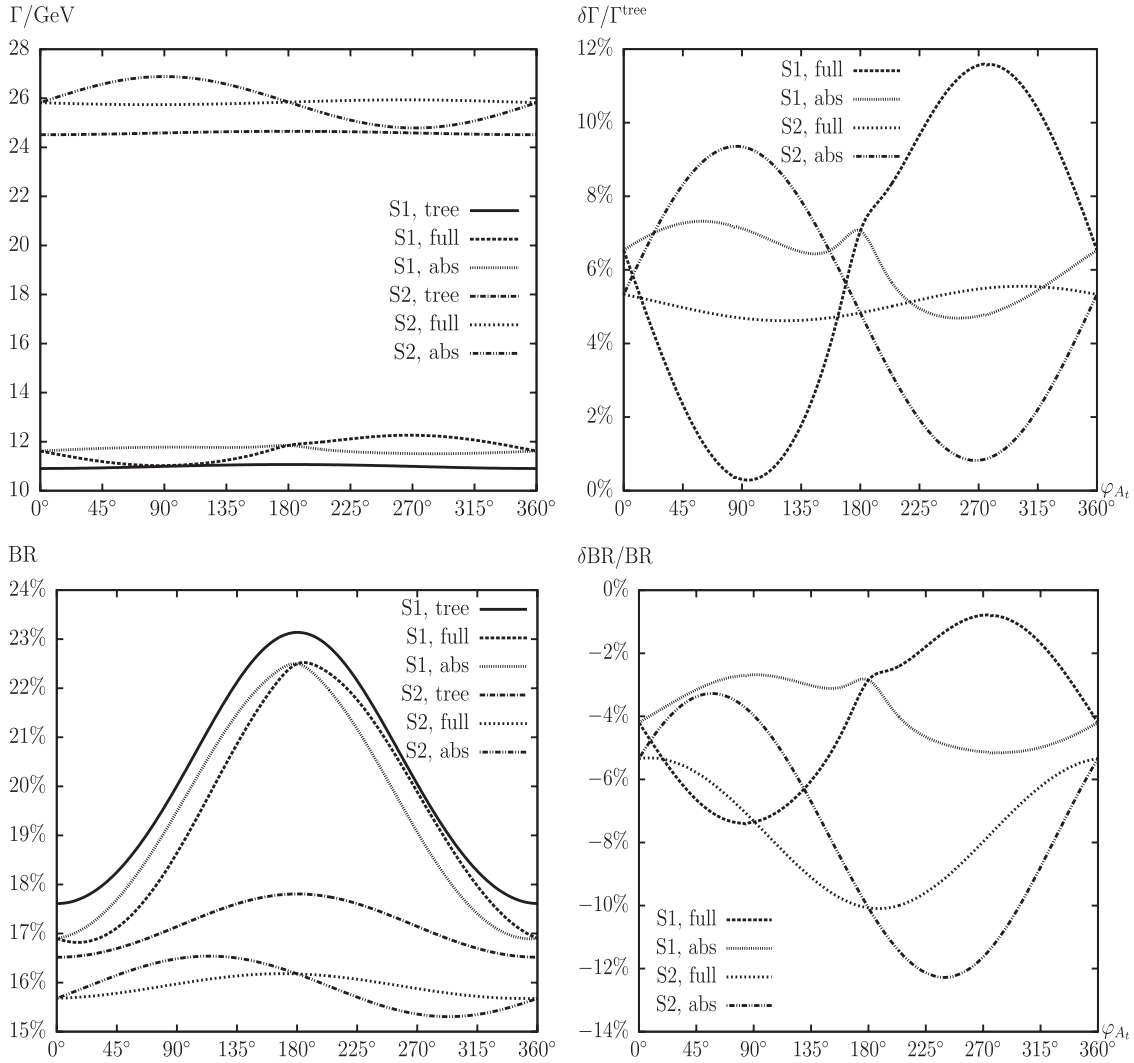


FIG. 36. $\Gamma(\tilde{t}_2 \rightarrow \tilde{b}_1 W^+)$. Tree-level (tree) and full one-loop (full) corrected partial decay widths are shown. Also shown are the full one-loop corrected partial decay widths including absorptive contributions (abs). The parameters are chosen according to S1 and S2 (see Table I), with φ_{A_i} varied. The upper left plot shows the partial decay width, the upper right plot the corresponding relative size of the corrections. The lower left plot shows the BR, the lower right plot the relative correction of the BR.

reach -7% (-10%), which is potentially important for physics at the ILC and the LHC.

D. The total decay width

Finally we show the results for the total decay width of \tilde{t}_2 . In Fig. 38 the upper panels show the absolute and relative variation with $m_{\tilde{t}_2}$. The lower panels depict the result for varying φ_{A_i} . In S1 for small $m_{\tilde{t}_2}$, $m_{\tilde{t}_1} + m_{\tilde{t}_2} \leq 1000$ GeV the size of the relative corrections of Γ_{tot} ranges between $+15\%$ and $+8\%$. For larger $m_{\tilde{t}_2}$ in the two numerical scenarios the variation ranges between $\sim +7\%$ down to $\sim -5\%$ for $m_{\tilde{t}_2} = 3$ TeV. The variation with φ_{A_i} is found to be large in both numerical scenarios. Within S1 we find values of the relative correction between $+13\%$ and $+7\%$, decreasing to a range of $+9.5\%$ and $+11\%$ once

the absorptive contributions are taken into account. For S2 the absolute values as well as the relative correction of Γ_{tot} , are larger than in S1. The size of the relative corrections ranges between $+11\%$ and $+15.5\%$, where the absorptive contributions do not change the overall size of the effects but only affect the dependence on φ_{A_i} .

V. CONCLUSIONS

We evaluate all partial decay widths corresponding to a two-body decay of the heavy scalar top quark in the minimal supersymmetric standard model with complex parameters. The decay modes are given in Eqs. (1)–(7). The evaluation is based on a full one-loop calculation of all decay channels, also including hard QED and QCD radiation. Such a calculation is necessary to derive a reliable

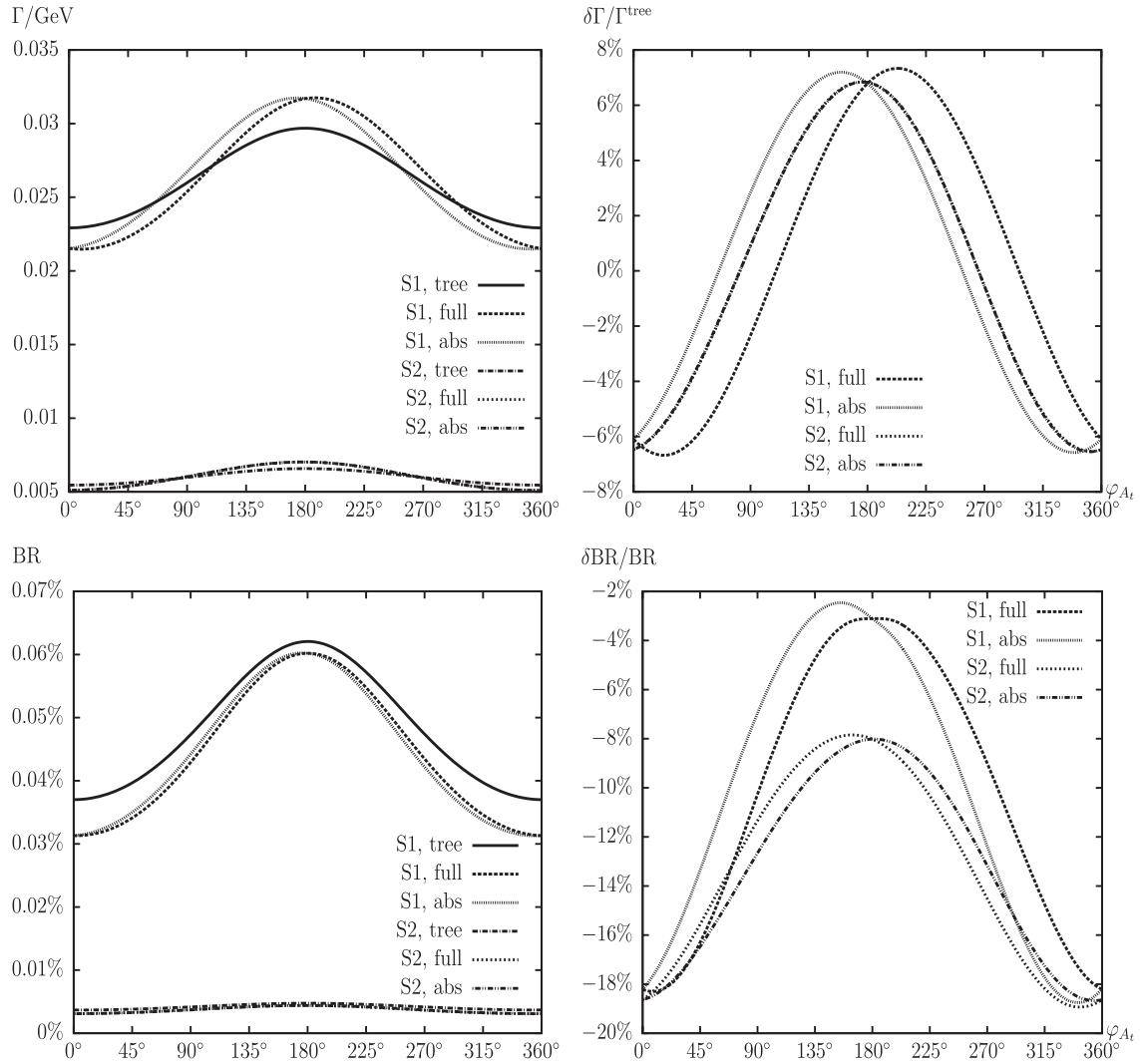


FIG. 37. $\Gamma(\tilde{t}_2 \rightarrow \tilde{b}_2 W^+)$. Tree-level (tree) and full one-loop (full) corrected partial decay widths are shown. Also shown are the full one-loop corrected partial decay widths including absorptive contributions (abs). The parameters are chosen according to S1 and S2 (see Table I), with φ_{A_t} varied. The upper left plot shows the partial decay width, the upper right plot the corresponding relative size of the corrections. The lower left plot shows the BR, the lower right plot the relative correction of the BR.

prediction of any two-body decay branching ratio. Three-body decay modes can become sizable only if all the two-body decay channels are kinematically (nearly) closed and have thus been neglected throughout the paper.

We first reviewed the one-loop renormalization procedure of the cMSSM, which is relevant for our calculation. This includes the t/\tilde{t} and b/\tilde{b} sector (which has been chosen according to the analysis in Refs. [38]), the gluino sector, and the strong coupling constant. We furthermore reviewed the required renormalization of the Higgs and SM gauge boson sector as well as the chargino and neutralino sector in the cMSSM.

We have discussed the calculation of the one-loop diagrams, the treatment of UV- and IR divergences that are canceled by the inclusion of (hard and soft) QCD and QED radiation. Our calculation setup can easily be extended to

other two-body decay modes in the cMSSM. In fact in order to test our method we checked the finiteness of various other partial decay widths (considering neutralino, chargino, and Higgs boson decays).

For the numerical analysis we have chosen two parameter sets that allow simultaneously *all* two-body decay modes (but could potentially be in conflict with the most recent SUSY search results from the LHC). The masses of the scalar top quarks in these scenarios are 260 and 650 GeV, and 720 and 1200 GeV for the lighter and the heavier stop, respectively. Consequently, both scenarios result in copious scalar top quark production at the LHC. A decay of the heavy stop to a lighter stop (or sbottom) and a neutral (or charged) Higgs boson can serve as a source of Higgs bosons at the LHC, thus a precise knowledge of stop branching ratios is required. The first scenario also allows

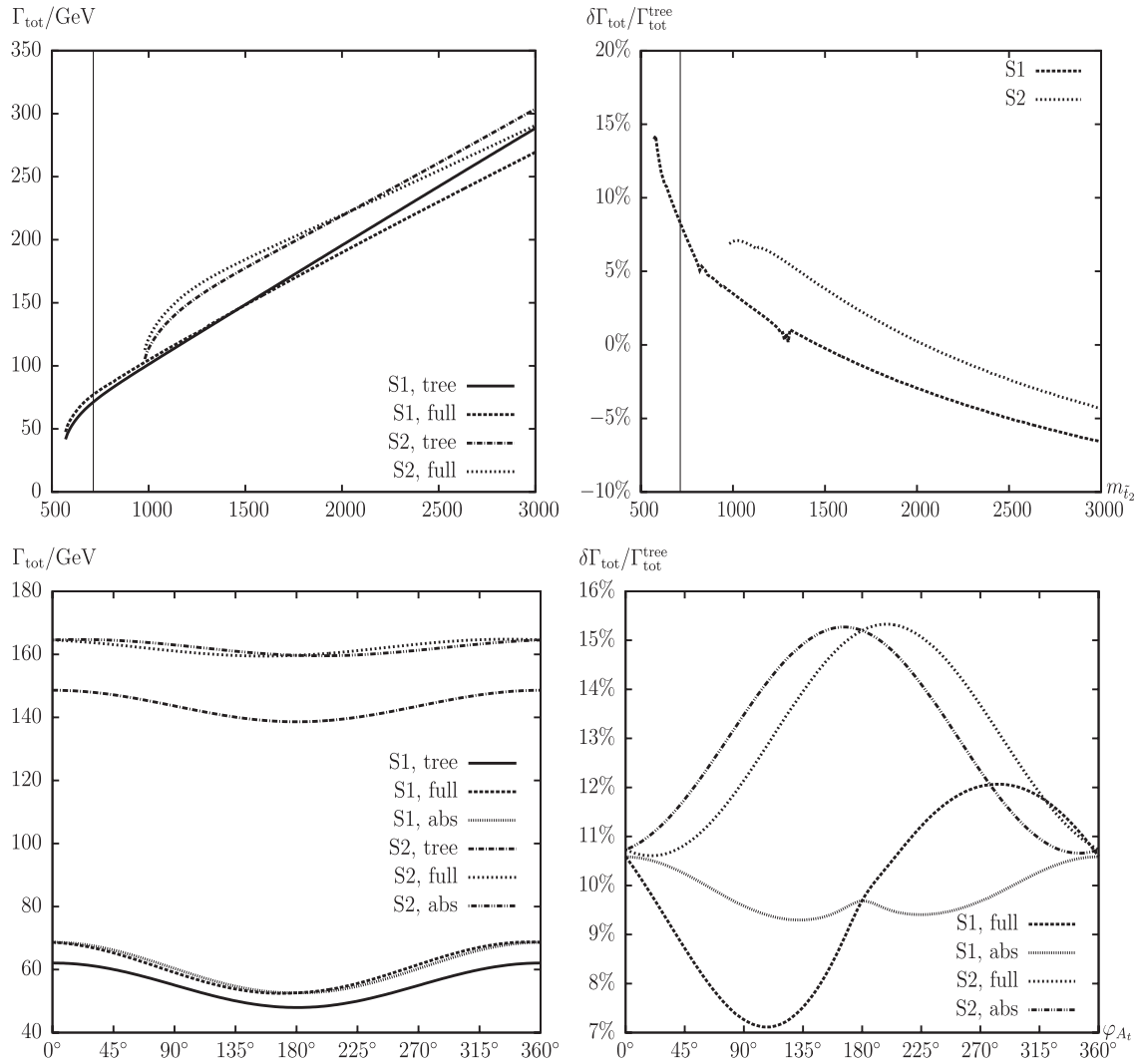


FIG. 38. Γ_{tot} . The tree-level (tree) and full one-loop (full) corrected total decay widths shown with the parameters chosen according to S1 and S2 (see Table I). The upper left plot shows the total decay width, the upper right plot the corresponding relative size of the total corrections, with $m_{\tilde{t}_2}$ varied. The lower plots show the same but with φ_{A_i} varied. Also shown is the full one-loop corrected total decay width including absorptive contributions (abs).

$\tilde{t}_1^\dagger \tilde{t}_2$ production at the ILC(1000), where statistically dominated experimental measurements of the heavy stop branching ratios will be possible. Depending on the integrated luminosity a precision at the few percent level seems to be achievable.

In our numerical analysis we have shown results for varying $m_{\tilde{t}_2}$ and φ_{A_i} , the phase of the trilinear coupling A_t . In the results with varied $m_{\tilde{t}_2}$ only the lighter values allow $\tilde{t}_1^\dagger \tilde{t}_2$ production at the ILC(1000), whereas the results with varied φ_{A_i} have sufficiently light scalar top quarks to permit $e^+ e^- \rightarrow \tilde{t}_1^\dagger \tilde{t}_2$. In the two numerical scenarios we compared the tree-level partial widths with the one-loop corrected partial decay widths. In the analysis with φ_{A_i} varied we showed explicitly the effect of the absorptive parts of self-energy type corrections on external legs. We

also analyzed the relative change of the partial decay widths to demonstrate the size of the loop corrections on each individual channel. In order to see the effect on the experimentally accessible quantities we also show the various branching ratios at tree level (all channels are evaluated at tree level) and at the one-loop level (with all channels evaluated including the full one-loop contributions). Furthermore we presented the relative change of the BRs that can directly be compared with the anticipated experimental accuracy.

We found sizable, roughly $\mathcal{O}(10\%)$, corrections in all the channels. For some parts of the parameter space (not only close to thresholds) also larger corrections up to 30% or 40% have been observed. This applies especially to the BR($\tilde{t}_2 \rightarrow \tilde{t}_1 h_n$) with $n = 1, 2, 3$. The size of the full one-loop corrections to the partial decay widths and the

branching ratios also depends strongly on φ_{A_i} . The one-loop contributions, again being roughly of $\mathcal{O}(10\%)$, often vary by a factor of 2–3 as a function of φ_{A_i} . In some cases the absorptive contributions can change the result visibly. All results are given in detail in Secs. [IV B](#) and [IV C](#).

The numerical results we have shown are, of course, dependent on the choice of the SUSY parameters. Nevertheless, they give an idea of the relevance of the full one-loop corrections. The largest partial decay width, if kinematically allowed, is $\Gamma(\tilde{t}_2 \rightarrow t\tilde{g})$ in our scenarios, dominating the total decay width, Γ_{tot} , and thus the various branching ratios. For other choices of $m_{\tilde{g}}$ with $m_{\tilde{g}} > m_{\tilde{t}_2}$ the corrections to the partial decay widths would stay the same, but the branching ratios would look very different. Decay channels (and their respective one-loop corrections) that may look unobservable due to the smallness of their BR in our numerical examples could become important if other channels are kinematically forbidden.

Following our analysis it is evident that the full one-loop corrections are mandatory for a precise prediction of the various branching ratios. The results for the scalar top quark decays will be implemented into the Fortran code FEYNHIGGS.

ACKNOWLEDGMENTS

We thank P. Bechtle, K. Desch, S. Dittmaier, A. Fowler, J. Guasch, H. Haber, T. Hahn, W. Hollik, L. Mihaila, E. Mirabella, F. von der Pahlen, T. Plehn, D. Stöckinger, and G. Weiglein for helpful discussions. The work of S. H. was supported in part by CICYT (Grant No. FPA 2007-66387), in part by CICYT (Grant No. FPA 2010-22163-C02-01), and by the Spanish MICINN's Consolider-Ingenio 2010 Program under Grant MultiDark No. CSD2009-00064. This work was supported in part by the European Community's Marie-Curie Research Training Network under Contract No. MRTN-CT-2006-035505 "Tools and Precision Calculations for Physics Discoveries at Colliders." Part of the work was performed while H. R. was at Albert-Ludwigs-Universität Freiburg, Freiburg, Germany.

APPENDIX A: ABSORPTIVE PARTS FROM SELF-ENERGY TYPE CONTRIBUTIONS

As indicated in the main text, contributions to the partial decay widths can arise from the product of the imaginary parts of the loop functions (absorptive parts) of the self-energy type contributions in the external legs and the imaginary parts of complex couplings entering the decay vertex or the self-energies. In our calculation these corrections are taken into account via wave function correction factors $\delta\hat{Z}$ (which should not be confused with the field renormalization constants δZ , which have been introduced via the multiplicative renormalization procedure). For the off-diagonal wave function correction factors, this

procedure has been checked against explicitly including the (renormalized) self-energy type corrections of the external legs, and full agreement has been found. The corrections from the absorptive parts can be sizable.

It is possible to combine the wave function correction factors with the field renormalization constants in a single Z factor, \hat{Z} , see e.g. Ref. [\[92\]](#) and references therein.

However, if the external particles were stable the wave function corrections would be fully taken into account via the field renormalization constants. The Z factors listed in Sec. [II](#) also ensure that the external (stable) particle does not mix with other fields, which is one of the on-shell properties. In our scenarios, this is true e.g. the lightest neutralino.

In the case of quasistable particles,³⁰ additional contributions to the mixing can occur so that the field renormalization constants only partly ensure no mixing (for a more detailed explanation, see the subsection scalar quarks below). Extra diagonal contributions can also be taken into account via \hat{Z} factors.³¹ Here we briefly list all the resulting constants.

1. Scalar quarks

- (i) For an on-shell particle state, no mixing with another state should occur, corresponding to

$$\begin{aligned}\hat{\Sigma}_{\tilde{q}_{12}}(m_{\tilde{q}_1}^2) &= 0, & \hat{\Sigma}_{\tilde{q}_{12}}(m_{\tilde{q}_2}^2) &= 0, \\ \hat{\Sigma}_{\tilde{q}_{21}}(m_{\tilde{q}_1}^2) &= 0, & \hat{\Sigma}_{\tilde{q}_{21}}(m_{\tilde{q}_2}^2) &= 0,\end{aligned}\quad (\text{A1})$$

in the case of squarks. Partly, this is already fulfilled due to our renormalization conditions Eq. [\(59\)](#) in Sec. [II A 1](#). As the considered external particles are quasistable, in spite of the renormalization conditions above, there remains a contribution of the imaginary parts of the loop functions. This contribution is taken into account via wave function correction factors $\delta\hat{Z}$, which are different for incoming squarks/outgoing antisquarks (unbarred) and outgoing squarks/incoming antisquarks (barred),

$$\begin{aligned}[\delta\hat{Z}_{\tilde{q}}]_{12} &= +2i \frac{\widetilde{\text{Im}}\Sigma_{\tilde{q}_{12}}(m_{\tilde{q}_2}^2)}{(m_{\tilde{q}_1}^2 - m_{\tilde{q}_2}^2)}, \\ [\delta\hat{Z}_{\tilde{q}}]_{21} &= -2i \frac{\widetilde{\text{Im}}\Sigma_{\tilde{q}_{21}}(m_{\tilde{q}_1}^2)}{(m_{\tilde{q}_1}^2 - m_{\tilde{q}_2}^2)},\end{aligned}\quad (\text{A2})$$

³⁰Which means that considering them as external particles is an approximation, which is justified because in our decays the contributions from the (additional) diagonal $\delta\hat{Z}$ are numerically rather negligible.

³¹There is still an ongoing discussion whether the diagonal field renormalization constants take into account all the contributions needed to ensure the on-shell properties of the external particles or whether an extra wave function correction factor $\delta\hat{Z}$ is needed.

$$\begin{aligned}
[\delta \tilde{\mathbf{Z}}_{\bar{q}}]_{12} &= +2i \frac{\widetilde{\text{Im}} \Sigma_{\bar{q}21}(m_{\bar{q}_2}^2)}{(m_{\bar{q}_1}^2 - m_{\bar{q}_2}^2)}, \\
[\delta \tilde{\mathbf{Z}}_{\bar{q}}]_{21} &= -2i \frac{\widetilde{\text{Im}} \Sigma_{\bar{q}12}(m_{\bar{q}_1}^2)}{(m_{\bar{q}_1}^2 - m_{\bar{q}_2}^2)},
\end{aligned} \tag{A3}$$

where $\widetilde{\text{Im}}$ takes only the imaginary part of the loop functions. Compact expressions for practical numerical calculations are obtained via the combined Z factors δZ ,

$$[\delta Z_{\bar{q}}]_{12} = [\delta \mathbf{Z}_{\bar{q}} + \delta \hat{\mathbf{Z}}_{\bar{q}}]_{12} = +2 \frac{\Sigma_{\bar{q}12}(m_{\bar{q}_2}^2) - \delta Y_q}{(m_{\bar{q}_1}^2 - m_{\bar{q}_2}^2)}, \tag{A4}$$

$$[\delta Z_{\bar{q}}]_{21} = [\delta \mathbf{Z}_{\bar{q}} + \delta \hat{\mathbf{Z}}_{\bar{q}}]_{21} = -2 \frac{\Sigma_{\bar{q}21}(m_{\bar{q}_1}^2) - \delta Y_q^*}{(m_{\bar{q}_1}^2 - m_{\bar{q}_2}^2)}, \tag{A5}$$

$$[\delta \bar{Z}_{\bar{q}}]_{12} = [\delta \mathbf{Z}_{\bar{q}}^* + \delta \hat{\mathbf{Z}}_{\bar{q}}]_{12} = +2 \frac{\Sigma_{\bar{q}21}(m_{\bar{q}_2}^2) - \delta Y_q^*}{(m_{\bar{q}_1}^2 - m_{\bar{q}_2}^2)}, \tag{A6}$$

$$[\delta \bar{Z}_{\bar{q}}]_{21} = [\delta \mathbf{Z}_{\bar{q}}^* + \delta \hat{\mathbf{Z}}_{\bar{q}}]_{21} = -2 \frac{\Sigma_{\bar{q}12}(m_{\bar{q}_1}^2) - \delta Y_q}{(m_{\bar{q}_1}^2 - m_{\bar{q}_2}^2)}. \tag{A7}$$

- (ii) The diagonal contributions result in the following combined Z factors:

$$\begin{aligned}
[\delta Z_{\bar{q}}]_{ii} &= [\delta \mathbf{Z}_{\bar{q}} + \delta \hat{\mathbf{Z}}_{\bar{q}}]_{ii} \\
&= -[\widetilde{\text{Re}} \Sigma'_{\bar{q}ii}(m_{\bar{q}_i}^2) + i \widetilde{\text{Im}} \Sigma'_{\bar{q}ii}(m_{\bar{q}_i}^2)] \\
&= -\Sigma'_{\bar{q}ii}(m_{\bar{q}_i}^2),
\end{aligned} \tag{A8}$$

$$\begin{aligned}
[\delta \bar{Z}_{\bar{q}}]_{ii} &= [\delta \mathbf{Z}_{\bar{q}}^* + \delta \hat{\mathbf{Z}}_{\bar{q}}]_{ii} \\
&= -[\widetilde{\text{Re}} \Sigma'_{\bar{q}ii}(m_{\bar{q}_i}^2) + i \widetilde{\text{Im}} \Sigma'_{\bar{q}ii}(m_{\bar{q}_i}^2)] \\
&= [\delta Z_{\bar{q}}]_{ii}.
\end{aligned} \tag{A9}$$

It should be noted that $\widetilde{\text{Re}} \Sigma_{ij}(p^2) = (\widetilde{\text{Re}} \Sigma_{ji}(p^2))^*$ holds due to $\mathcal{CP}\mathcal{T}$ invariance and the squark field renormalization constants obey $[\widetilde{\text{Re}} \delta \bar{Z}_{\bar{q}}]_{ij} = [\widetilde{\text{Re}} \delta Z_{\bar{q}}]_{ij}^* = [\delta Z_{\bar{q}}]_{ij}^*$, which is exactly the case without absorptive contributions as described in Sec. II A 1.

In the following we will only give the Z factors that combine the renormalization factors and the additional wave function correction factors. The derivation is analogous to the one performed in the squark sector.

2. Quarks

The new (diagonal) combined factors Z_q , taking into account the absorptive part of the self-energy type contribution on an external quark leg are different for incoming quarks/outgoing antiquarks (unbarred) and outgoing quarks/incoming antiquarks (barred),

$$\begin{aligned}
\delta Z_q^{L/R} &= -[\Sigma_q^{L/R}(m_q^2) + m_q^2(\Sigma_q^{L'}(m_q^2) + \Sigma_q^{R'}(m_q^2)) \\
&\quad + m_q(\Sigma_q^{SL'}(m_q^2) + \Sigma_q^{SR'}(m_q^2))] \\
&\quad \pm \frac{1}{2m_q}[\Sigma_q^{SL}(m_q^2) - \Sigma_q^{SR}(m_q^2)],
\end{aligned} \tag{A10}$$

$$\begin{aligned}
\delta \bar{Z}_q^{L/R} &= -[\Sigma_q^{L/R}(m_q^2) + m_q^2(\Sigma_q^{L'}(m_q^2) + \Sigma_q^{R'}(m_q^2)) \\
&\quad + m_q(\Sigma_q^{SL'}(m_q^2) + \Sigma_q^{SR'}(m_q^2))] \\
&\quad \mp \frac{1}{2m_q}[\Sigma_q^{SL}(m_q^2) - \Sigma_q^{SR}(m_q^2)].
\end{aligned} \tag{A11}$$

The diagonal quark field renormalization constants obey $\widetilde{\text{Re}} \delta \bar{Z}_q^{L/R} = [\delta Z_q^{L/R}]^*$, which is exactly the case without absorptive contributions as described in Sec. II A 1.

There are no additional off-diagonal terms to the absorptive contributions because the CKM matrix has been set to unity.

3. Gluinos

The new combined factors $Z_{\tilde{g}}$, taking into account the absorptive part of the self-energy type contribution on the external gluino leg are unbarred (barred) for an incoming (outgoing) gluino,

$$\begin{aligned}
\delta Z_{\tilde{g}}^{L/R} &= -[\Sigma_{\tilde{g}}^{L/R}(m_{\tilde{g}}^2) + m_{\tilde{g}}^2(\Sigma_{\tilde{g}}^{L'}(m_{\tilde{g}}^2) + \Sigma_{\tilde{g}}^{R'}(m_{\tilde{g}}^2)) \\
&\quad + m_{\tilde{g}}(\Sigma_{\tilde{g}}^{SL'}(m_{\tilde{g}}^2) + \Sigma_{\tilde{g}}^{SR'}(m_{\tilde{g}}^2))] \\
&\quad \pm \frac{1}{2m_{\tilde{g}}}[\Sigma_{\tilde{g}}^{SL}(m_{\tilde{g}}^2) - \Sigma_{\tilde{g}}^{SR}(m_{\tilde{g}}^2)],
\end{aligned} \tag{A12}$$

$$\delta \bar{Z}_{\tilde{g}}^{L/R} = \delta Z_{\tilde{g}}^{R/L}. \tag{A13}$$

The last formula holds due to the Majorana character of the gluino and the $Z_{\tilde{g}}$ factors obey $\widetilde{\text{Re}} \delta \bar{Z}_{\tilde{g}}^{L/R} = \widetilde{\text{Re}} \delta Z_{\tilde{g}}^{R/L} = \delta Z_{\tilde{g}}^*/\delta Z_{\tilde{g}}$, which is exactly the case without absorptive contributions as described in Sec. II A 2.

4. Higgs bosons

Finite contributions from the neutral Higgs wave function correction factors are taken into account via the \mathbf{Z} matrix, see Eq. (132), which is a complex quantity. The application of the \mathbf{Z} matrix at the amplitude level automatically takes any absorptive contribution into account.

For the charged Higgs bosons, the new combined factors Z_{H^\pm} [unbarred (barred) for an incoming (outgoing) Higgs] read

$$\delta Z_{H^-H^+} = -\Sigma'_{H^-H^+}(M_{H^\pm}^2), \quad (\text{A14})$$

$$\delta \bar{Z}_{H^-H^+} = \delta Z_{H^-H^+} \quad (\text{A15})$$

instead of Eq. (99g) in addition with Eq. (134).

5. Vector bosons

For the vector bosons, the new combined factors $Z_{\{WW,ZZ\}}$ are

$$\delta Z_{ZZ} = -\Sigma_{ZZ}^{T/}(M_Z^2), \quad \delta Z_{WW} = -\Sigma_{WW}^{T/}(M_W^2), \quad (\text{A16})$$

$$\delta \bar{Z}_{ZZ} = \delta Z_{ZZ}, \quad \delta \bar{Z}_{WW} = \delta Z_{WW}. \quad (\text{A17})$$

However, we found that the additional corrections from vector boson self-energies due to the imaginary parts do not give a contribution (because in this paper all SUSY masses are larger than M_Z), and hence no change in the Z factors is required.

6. Charginos and neutralinos

More details to the new combined factors $Z_{\tilde{\chi}^-}$ and $Z_{\tilde{\chi}^0}$ (taking into account the absorptive part of the self-energy type contributions on the external legs) can be found in Ref. [93]. In our notation they read (unbarred for an incoming neutralino or a negative chargino, barred for an outgoing neutralino or negative chargino)

$$\begin{aligned} [\delta Z_{\tilde{\chi}^\pm}^{L/R}]_{ii} &= -[\Sigma_{\tilde{\chi}^\pm}^{L/R}(m_{\tilde{\chi}_i^\pm}^2) + m_{\tilde{\chi}_i^\pm}^2(\Sigma_{\tilde{\chi}^\pm}^{L'}(m_{\tilde{\chi}_i^\pm}^2) \\ &+ \Sigma_{\tilde{\chi}^\pm}^{R'}(m_{\tilde{\chi}_i^\pm}^2)) + m_{\tilde{\chi}_i^\pm}(\Sigma_{\tilde{\chi}^\pm}^{SL'}(m_{\tilde{\chi}_i^\pm}^2) \\ &+ \Sigma_{\tilde{\chi}^\pm}^{SR'}(m_{\tilde{\chi}_i^\pm}^2))]_{ii} \pm \frac{1}{2m_{\tilde{\chi}_i^\pm}}[\Sigma_{\tilde{\chi}^\pm}^{SL}(m_{\tilde{\chi}_i^\pm}^2) \\ &- \Sigma_{\tilde{\chi}^\pm}^{SR}(m_{\tilde{\chi}_i^\pm}^2) - \delta \mathbf{M}_{\tilde{\chi}^\pm} + \delta \mathbf{M}_{\tilde{\chi}^\pm}^*]_{ii}, \quad (\text{A18}) \end{aligned}$$

$$\begin{aligned} [\delta Z_{\tilde{\chi}^\pm}^{L/R}]_{ij} &= \frac{2}{m_{\tilde{\chi}_i^\pm}^2 - m_{\tilde{\chi}_j^\pm}^2} [m_{\tilde{\chi}_j^\pm}^2 \Sigma_{\tilde{\chi}^\pm}^{L/R}(m_{\tilde{\chi}_j^\pm}^2) \\ &+ m_{\tilde{\chi}_i^\pm} m_{\tilde{\chi}_j^\pm} \Sigma_{\tilde{\chi}^\pm}^{R/L}(m_{\tilde{\chi}_j^\pm}^2) + m_{\tilde{\chi}_i^\pm} \Sigma_{\tilde{\chi}^\pm}^{SL/SR}(m_{\tilde{\chi}_j^\pm}^2) \\ &+ m_{\tilde{\chi}_j^\pm} \Sigma_{\tilde{\chi}^\pm}^{SR/SL}(m_{\tilde{\chi}_j^\pm}^2) - m_{\tilde{\chi}_{ij}^\pm} \delta \mathbf{M}_{\tilde{\chi}^\pm} \\ &- m_{\tilde{\chi}_{ji}^\pm} \delta \mathbf{M}_{\tilde{\chi}^\pm}^\dagger]_{ij}, \quad (\text{A19}) \end{aligned}$$

$$\begin{aligned} [\delta Z_{\tilde{\chi}^0}^{L/R}]_{kk} &= -[\Sigma_{\tilde{\chi}^0}^{L/R}(m_{\tilde{\chi}_k^0}^2) + m_{\tilde{\chi}_k^0}^2(\Sigma_{\tilde{\chi}^0}^{L'}(m_{\tilde{\chi}_k^0}^2) + \Sigma_{\tilde{\chi}^0}^{R'}(m_{\tilde{\chi}_k^0}^2)) \\ &+ m_{\tilde{\chi}_k^0}(\Sigma_{\tilde{\chi}^0}^{SL'}(m_{\tilde{\chi}_k^0}^2) + \Sigma_{\tilde{\chi}^0}^{SR'}(m_{\tilde{\chi}_k^0}^2))]_{kk} \\ &\pm \frac{1}{2m_{\tilde{\chi}_k^0}}[\Sigma_{\tilde{\chi}^0}^{SL}(m_{\tilde{\chi}_k^0}^2) - \Sigma_{\tilde{\chi}^0}^{SR}(m_{\tilde{\chi}_k^0}^2) \\ &- \delta \mathbf{M}_{\tilde{\chi}^0} + \delta \mathbf{M}_{\tilde{\chi}^0}^*]_{kk}, \quad (\text{A20}) \end{aligned}$$

$$\begin{aligned} [\delta Z_{\tilde{\chi}^0}^{L/R}]_{kl} &= \frac{2}{m_{\tilde{\chi}_k^0}^2 - m_{\tilde{\chi}_l^0}^2} [m_{\tilde{\chi}_l^0}^2 \Sigma_{\tilde{\chi}^0}^{L/R}(m_{\tilde{\chi}_l^0}^2) \\ &+ m_{\tilde{\chi}_k^0} m_{\tilde{\chi}_l^0} \Sigma_{\tilde{\chi}^0}^{R/L}(m_{\tilde{\chi}_l^0}^2) + m_{\tilde{\chi}_k^0} \Sigma_{\tilde{\chi}^0}^{SL/SR}(m_{\tilde{\chi}_l^0}^2) \\ &+ m_{\tilde{\chi}_l^0} \Sigma_{\tilde{\chi}^0}^{SR/SL}(m_{\tilde{\chi}_l^0}^2) - m_{\tilde{\chi}_{k/l}^0} \delta \mathbf{M}_{\tilde{\chi}^0} \\ &- m_{\tilde{\chi}_{l/k}^0} \delta \mathbf{M}_{\tilde{\chi}^0}^\dagger]_{kl}, \quad (\text{A21}) \end{aligned}$$

$$\begin{aligned} [\delta \bar{Z}_{\tilde{\chi}^\pm}^{L/R}]_{ii} &= -[\Sigma_{\tilde{\chi}^\pm}^{L/R}(m_{\tilde{\chi}_i^\pm}^2) + m_{\tilde{\chi}_i^\pm}^2(\Sigma_{\tilde{\chi}^\pm}^{L'}(m_{\tilde{\chi}_i^\pm}^2) \\ &+ \Sigma_{\tilde{\chi}^\pm}^{R'}(m_{\tilde{\chi}_i^\pm}^2)) + m_{\tilde{\chi}_i^\pm}(\Sigma_{\tilde{\chi}^\pm}^{SL'}(m_{\tilde{\chi}_i^\pm}^2) \\ &+ \Sigma_{\tilde{\chi}^\pm}^{SR'}(m_{\tilde{\chi}_i^\pm}^2))]_{ii} \mp \frac{1}{2m_{\tilde{\chi}_i^\pm}}[\Sigma_{\tilde{\chi}^\pm}^{SL}(m_{\tilde{\chi}_i^\pm}^2) \\ &- \Sigma_{\tilde{\chi}^\pm}^{SR}(m_{\tilde{\chi}_i^\pm}^2) - \delta \mathbf{M}_{\tilde{\chi}^\pm} + \delta \mathbf{M}_{\tilde{\chi}^\pm}^*]_{ii}, \quad (\text{A22}) \end{aligned}$$

$$\begin{aligned} [\delta \bar{Z}_{\tilde{\chi}^\pm}^{L/R}]_{ij} &= \frac{2}{m_{\tilde{\chi}_j^\pm}^2 - m_{\tilde{\chi}_i^\pm}^2} [m_{\tilde{\chi}_i^\pm}^2 \Sigma_{\tilde{\chi}^\pm}^{L/R}(m_{\tilde{\chi}_i^\pm}^2) \\ &+ m_{\tilde{\chi}_i^\pm} m_{\tilde{\chi}_j^\pm} \Sigma_{\tilde{\chi}^\pm}^{R/L}(m_{\tilde{\chi}_i^\pm}^2) \\ &+ m_{\tilde{\chi}_i^\pm} \Sigma_{\tilde{\chi}^\pm}^{SL/SR}(m_{\tilde{\chi}_i^\pm}^2) + m_{\tilde{\chi}_j^\pm} \Sigma_{\tilde{\chi}^\pm}^{SR/SL}(m_{\tilde{\chi}_i^\pm}^2) \\ &- m_{\tilde{\chi}_{ij}^\pm} \delta \mathbf{M}_{\tilde{\chi}^\pm} - m_{\tilde{\chi}_{ji}^\pm} \delta \mathbf{M}_{\tilde{\chi}^\pm}^\dagger]_{ij}, \quad (\text{A23}) \end{aligned}$$

$$[\delta \bar{Z}_{\tilde{\chi}^0}^{L/R}]_{kk} = [\delta Z_{\tilde{\chi}^0}^{R/L}]_{kk}, \quad (\text{A24})$$

$$[\delta \bar{Z}_{\tilde{\chi}^0}^{L/R}]_{kl} = [\delta Z_{\tilde{\chi}^0}^{R/L}]_{lk}. \quad (\text{A25})$$

The chargino/neutralino Z factors obey $\widetilde{\text{Re}} \delta \bar{Z}_{\tilde{\chi}^\pm}^{L/R} = [\widetilde{\text{Re}} \delta Z_{\tilde{\chi}^\pm}^{L/R}]^\dagger = [\delta \mathbf{Z}_{\tilde{\chi}^\pm}^{L/R}]^\dagger$, which is exactly the case without absorptive contributions as described in Sec. II C, or in other words $\delta \bar{Z}_{\tilde{\chi}^\pm}^{L/R} = [\delta \mathbf{Z}_{\tilde{\chi}^\pm}^{L/R}]^\dagger + [\delta \bar{\mathbf{Z}}_{\tilde{\chi}^\pm}^{L/R}]$. The Eqs. (A24) and (A25) hold due to the Majorana character of the neutralinos.

- [1] H. P. Nilles, *Phys. Rep.* **110**, 1 (1984); H. E. Haber and G. L. Kane, *Phys. Rep.* **117**, 75 (1985); R. Barbieri, *Riv. Nuovo Cimento* **11N4**, 1 (1988).
- [2] G. Aad *et al.* (ATLAS Collaboration), [arXiv:0901.0512](https://arxiv.org/abs/0901.0512).
- [3] G. Bayatian *et al.* (CMS Collaboration), *J. Phys. G* **34**, 995 (2007).
- [4] TESLA Collaboration, [arXiv:hep-ph/0106315](https://arxiv.org/abs/hep-ph/0106315); see tesla-desy.de/new_pages/TDR_CD/start.html; K. Ackermann *et al.*, Report No. DESY-PROC-2004-01.
- [5] J. Brau *et al.* (ILC Collaboration), [arXiv:0712.1950](https://arxiv.org/abs/0712.1950); G. Aarons *et al.* (ILC Collaboration), [arXiv:0709.1893](https://arxiv.org/abs/0709.1893).
- [6] G. Weiglein *et al.* (LHC/ILC Study Group), *Phys. Rep.* **426**, 47 (2006); A. De Roeck *et al.*, *Eur. Phys. J. C* **66**, 525 (2010); A. De Roeck, J. Ellis, and S. Heinemeyer, CERN Cour. **49N10**, 27 (2009).
- [7] K. Hikasa and M. Kobayashi, *Phys. Rev. D* **36**, 724 (1987); M. Mühlleitner and E. Popenza, *J. High Energy Phys.* **04**, (2011) 095.
- [8] H. Heath, C. Lynch, S. Moretti, and C. Shepherd-Themistocleous, [arXiv:0901.1676](https://arxiv.org/abs/0901.1676).
- [9] A. Datta, A. Djouadi, M. Guchait, and F. Moortgat, *Nucl. Phys.* **B681**, 31 (2004).
- [10] S. Kraml, H. Eberl, A. Bartl, W. Majerotto, and W. Porod, *Phys. Lett. B* **386**, 175 (1996); A. Djouadi, W. Hollik, and C. Jünger, *Phys. Rev. D* **55**, 6975 (1997).
- [11] W. Beenakker, R. Höpker, and P. Zerwas, *Phys. Lett. B* **378**, 159 (1996).
- [12] W. Beenakker, R. Höpker, T. Plehn, and P. Zerwas, *Z. Phys. C* **75**, 349 (1997).
- [13] A. Bartl, H. Eberl, K. Hidaka, S. Kraml, W. Majerotto, W. Porod, and Y. Yamada, *Phys. Lett. B* **419**, 243 (1998).
- [14] A. Bartl, H. Eberl, K. Hidaka, S. Kraml, W. Majerotto, W. Porod, and Y. Yamada, *Phys. Rev. D* **59**, 115007 (1999).
- [15] M. Mühlleitner, A. Djouadi, and Y. Mambrini, *Comput. Phys. Commun.* **168**, 46 (2005).
- [16] A. Bartl *et al.*, *Phys. Lett. B* **435**, 118 (1998).
- [17] J. Guasch, J. Sola, and W. Hollik, *Phys. Lett. B* **437**, 88 (1998).
- [18] L. Jin and C. Li, *Phys. Rev. D* **65**, 035007 (2002).
- [19] J. Guasch, W. Hollik, and J. Sola, *Phys. Lett. B* **510**, 211 (2001); *J. High Energy Phys.* **10** (2002) 040.
- [20] A. Arhrib and R. Benbrik, *Phys. Rev. D* **71**, 095001 (2005).
- [21] H. Hlucha, H. Eberl, and W. Frisch, [arXiv:1104.2151](https://arxiv.org/abs/1104.2151).
- [22] C. Weber, K. Kovarik, H. Eberl, and W. Majerotto, *Nucl. Phys.* **B776**, 138 (2007).
- [23] C. Weber, H. Eberl, and W. Majerotto, *Phys. Lett. B* **572**, 56 (2003).
- [24] E. Accomando, G. Chachamis, F. Fugel, M. Spira, and M. Walser, *Phys. Rev. D* **85**, 015004 (2012).
- [25] A. Bartl, S. Hesselbach, K. Hidaka, T. Kernreiter, and W. Porod, *Phys. Lett. B* **573**, 153 (2003).
- [26] A. Bartl, S. Hesselbach, K. Hidaka, T. Kernreiter, and W. Porod, *Phys. Rev. D* **70**, 035003 (2004).
- [27] H. Eberl, S. Frank, and W. Majerotto, *Eur. Phys. J. C* **70**, 1017 (2010).
- [28] O. Kittel and A. Pilaftsis, *Nucl. Phys.* **B856**, 682 (2012).
- [29] T. Ibrahim and P. Nath, *Phys. Rev. D* **71**, 055007 (2005).
- [30] A. Bartl, E. Christova, K. Hohenwarter-Sodek, and T. Kernreiter, *Phys. Rev. D* **70**, 095007 (2004).
- [31] J. Ellis, F. Moortgat, G. Moortgat-Pick, J. Smillie, and J. Tattersall, *Eur. Phys. J. C* **60**, 633 (2009).
- [32] F. Deppisch and O. Kittel, *J. High Energy Phys.* **09** (2009) 110; **03** (2010) 091(E).
- [33] F. Deppisch and O. Kittel, *J. High Energy Phys.* **06** (2010) 067.
- [34] S. Heinemeyer, W. Hollik, and G. Weiglein, *Comput. Phys. Commun.* **124**, 76 (2000); see www.feynhiggs.de.
- [35] S. Heinemeyer, W. Hollik, and G. Weiglein, *Eur. Phys. J. C* **9**, 343 (1999).
- [36] G. Degrassi, S. Heinemeyer, W. Hollik, P. Slavich, and G. Weiglein, *Eur. Phys. J. C* **28**, 133 (2003).
- [37] M. Frank, T. Hahn, S. Heinemeyer, W. Hollik, R. Rzehak, and G. Weiglein, *J. High Energy Phys.* **02** (2007) 047.
- [38] S. Heinemeyer, H. Rzehak, and C. Schappacher, *Phys. Rev. D* **82**, 075010 (2010); Proc. Sci., CHARGED2010 (2010) 039.
- [39] S. Heinemeyer, W. Hollik, H. Rzehak, and G. Weiglein, *Phys. Lett. B* **652**, 300 (2007).
- [40] H. Rzehak, Ph.D. thesis, Technische Universität München, 2005; see: nbn-resolving.de/ with urn: nbn:de:bvb:91-diss20050923-0853568146.
- [41] A. Djouadi, P. Gambino, S. Heinemeyer, W. Hollik, C. Jünger, and G. Weiglein, *Phys. Rev. Lett.* **78**, 3626 (1997); *Phys. Rev. D* **57**, 4179 (1998).
- [42] W. Hollik and H. Rzehak, *Eur. Phys. J. C* **32**, 127 (2003).
- [43] S. Heinemeyer, W. Hollik, H. Rzehak, and G. Weiglein, *Eur. Phys. J. C* **39**, 465 (2005).
- [44] C. AMSLER *et al.* (Particle Data Group), *Phys. Lett. B* **667**, 1 (2008).
- [45] K. Chetyrkin, J. Kühn, and M. Steinhauser, *Comput. Phys. Commun.* **133**, 43 (2000).
- [46] M. Carena, D. Garcia, U. Nierste, and C. Wagner, *Nucl. Phys.* **B577**, 88 (2000).
- [47] R. Hempfling, *Phys. Rev. D* **49**, 6168 (1994); L. Hall, R. Rattazzi, and U. Sarid, *Phys. Rev. D* **50**, 7048 (1994); M. Carena, M. Olechowski, S. Pokorski, and C. Wagner, *Nucl. Phys.* **B426**, 269 (1994).
- [48] M. S. Carena, J. R. Ellis, A. Pilaftsis, and C. E. M. Wagner, *Nucl. Phys.* **B586**, 92 (2000).
- [49] D. Noth and M. Spira, *Phys. Rev. Lett.* **101**, 181801 (2008); *J. High Energy Phys.* **06** (2011) 084.
- [50] T. Fritzsche, Ph. D. thesis, Cuvillier Verlag, Göttingen 2005.
- [51] R. Harlander, L. Mihaila, and M. Steinhauser, *Phys. Rev. D* **72**, 095009 (2005); *Phys. Rev. D* **76**, 055002 (2007).
- [52] R. Peccei and H. Quinn, *Phys. Rev. Lett.* **38**, 1440 (1977); *Phys. Rev. D* **16**, 1791 (1977).
- [53] S. Dimopoulos and S. Thomas, *Nucl. Phys.* **B465**, 23 (1996).
- [54] S. Heinemeyer, *Eur. Phys. J. C* **22**, 521 (2001).
- [55] M. Frank, S. Heinemeyer, W. Hollik, and G. Weiglein, [arXiv:hep-ph/0202166](https://arxiv.org/abs/hep-ph/0202166).
- [56] A. Freitas and D. Stöckinger, *Phys. Rev. D* **66**, 095014 (2002).
- [57] A. Brignole, *Phys. Lett. B* **281**, 284 (1992).
- [58] K. Williams, Ph.D. thesis, Durham University, 2008; available at www.ippp.dur.ac.uk/Research/theses.html.
- [59] N. Baro, F. Boudjema, and A. Semenov, *Phys. Rev. D* **78**, 115003 (2008).
- [60] K. Williams, H. Rzehak, and G. Weiglein, *Eur. Phys. J. C* **71**, 1669 (2011).
- [61] A. Denner, *Fortschr. Phys.* **41**, 307 (1993).

- [62] T. Takagi, *Japanese J. Math.* **1**, 83 (1927); J. H. Wilkinson and C. Reinsch, *Handbook for Automatic Computation* (Springer, New York, 1971); R. A. Horn and C. A. Johnson, *Matrix Analysis* (Cambridge University Press, Cambridge, England, 1990); T. Hahn, [arXiv:physics/0607103](https://arxiv.org/abs/physics/0607103).
- [63] A. Chatterjee, M. Drees, S. Kulkarni, and Q. Xu, *Phys. Rev. D* **85**, 075013 (2012).
- [64] N. Baro and F. Boudjema, *Phys. Rev. D* **80**, 076010 (2009).
- [65] T. Fritzsche and W. Hollik, *Eur. Phys. J. C* **24**, 619 (2002); T. Fritzsche, Diploma thesis, Institut für Theoretische Physik, Universität Karlsruhe, Germany, 2000; see www-ftp.particle.uni-karlsruhe.de/diplomatheses.de.shtml.
- [66] A. Denner, S. Dittmaier, M. Roth, and D. Wackerth, *Nucl. Phys.* **B560**, 33 (1999).
- [67] J. Küblbeck, M. Böhm, and A. Denner, *Comput. Phys. Commun.* **60**, 165 (1990); T. Hahn, *Comput. Phys. Commun.* **140**, 418 (2001); T. Hahn and C. Schappacher, *Comput. Phys. Commun.* **143**, 54 (2002). The program, the user's guide, and the MSSM model files are available via www.feynarts.de.
- [68] T. Hahn and M. Pérez-Victoria, *Comput. Phys. Commun.* **118**, 153 (1999).
- [69] F. del Aguila, A. Culatti, R. Muñoz Tapia, and M. Pérez-Victoria, *Nucl. Phys.* **B537**, 561 (1999).
- [70] W. Siegel, *Phys. Lett.* **84B**, 193 (1979); D. Capper, D. Jones, and P. van Nieuwenhuizen, *Nucl. Phys.* **B167**, 479 (1980).
- [71] D. Stöckinger, *J. High Energy Phys.* 03 (2005) 076.
- [72] W. Hollik and D. Stöckinger, *Phys. Lett. B* **634**, 63 (2006).
- [73] S. Dittmaier, *Nucl. Phys.* **B675**, 447 (2003).
- [74] W. Beenakker and A. Denner, *Nucl. Phys.* **B338**, 349 (1990).
- [75] The couplings can be found in the files MSSM.PS.GZ, MSSMQCD.PS.GZ, and HMIX.PS.GZ as part of the package [67].
- [76] K. Nakamura *et al.* (Particle Data Group Collaboration), *J. Phys. G* **37**, 075021 (2010).
- [77] J. Frere, D. Jones, and S. Raby, *Nucl. Phys.* **B222**, 11 (1983); M. Claudson, L. Hall, and I. Hinchliffe, *Nucl. Phys.* **B228**, 501 (1983); C. Kounnas, A. Lahanas, D. Nanopoulos, and M. Quiros, *Nucl. Phys.* **B236**, 438 (1984); J. Gunion, H. Haber, and M. Sher, *Nucl. Phys.* **B306**, 1 (1988); J. Casas, A. Lleyda, and C. Muñoz, *Nucl. Phys.* **B471**, 3 (1996); P. Langacker and N. Polonsky, *Phys. Rev. D* **50**, 2199 (1994); A. Strumia, *Nucl. Phys.* **B482**, 24 (1996).
- [78] LEP Higgs Working Group, *Phys. Lett. B* **565**, 61 (2003).
- [79] LEP Higgs Working Group, *Eur. Phys. J. C* **47**, 547 (2006).
- [80] S. Heinemeyer, O. Stål, and G. Weiglein, *Phys. Lett. B* **710**, 201 (2012); A. Arbey, M. Battaglia, A. Djouadi, F. Mahmoudi, and J. Quevillon, *Phys. Lett. B* **708**, 162 (2012).
- [81] W. Ehrenfeld, *SUSY11, Fermilab, 2011*, <https://indico.fnal.gov/contributionDisplay.py?sessionId=10&contribId=257&confId=3563>; I. Melzer-Pellmann, *SUSY11, Fermilab, 2011*, <https://indico.fnal.gov/contributionDisplay.py?sessionId=10&contribId=258&confId=3563>.
- [82] M. Dugan, B. Grinstein, and L. Hall, *Nucl. Phys.* **B255**, 413 (1985).
- [83] D. Demir, O. Lebedev, K. Olive, M. Pospelov, and A. Ritz, *Nucl. Phys.* **B680**, 339 (2004).
- [84] D. Chang, W. Keung, and A. Pilaftsis, *Phys. Rev. Lett.* **82**, 900 (1999); **83**, 3972(E)(1999). A. Pilaftsis, *Phys. Lett. B* **471**, 174 (1999).
- [85] O. Lebedev, K. Olive, M. Pospelov, and A. Ritz, *Phys. Rev. D* **70**, 016003 (2004).
- [86] W. Hollik, J. Illana, S. Rigolin, and D. Stöckinger, *Phys. Lett. B* **416**, 345 (1998); *Phys. Lett. B* **425**, 322 (1998).
- [87] P. Nath, *Phys. Rev. Lett.* **66**, 2565 (1991); Y. Kizukuri and N. Oshimo, *Phys. Rev. D* **46**, 3025 (1992).
- [88] T. Ibrahim and P. Nath, *Phys. Lett. B* **418**, 98 (1998); *Phys. Rev. D* **57**, 478 (1998); **58**, 019901(E) (1998); **60**, 079903(E) (1999); **60**, 119901(E) (1999); M. Brhlik, G. Good, and G. Kane, *Phys. Rev. D* **59**, 115004 (1999).
- [89] S. Abel, S. Khalil, and O. Lebedev, *Nucl. Phys.* **B606**, 151 (2001).
- [90] Y. Li, S. Profumo, and M. Ramsey-Musolf, *J. High Energy Phys.* 08 (2010) 062.
- [91] V. Barger, T. Falk, T. Han, J. Jiang, T. Li, and T. Plehn, *Phys. Rev. D* **64**, 056007 (2001).
- [92] A. Fowler and G. Weiglein, *J. High Energy Phys.* 01 (2010) 108.
- [93] A. Fowler, Ph. D. thesis, Durham University, United Kingdom, 2010.